Heat, Moisture, and Momentum Budgets of a Midlatitude Squall Line with a Trailing Stratiform Region

William A. Gallus

Colorado State University

DEPARTMENT OF ATMOSPHERIC SCIENCE

PAPER NO.
455

THE HEAT, MOISTURE, AND MOMENTUM BUDGETS OF A MIDLATITUDE SQUALL LINE WITH A TRAILING STRATIFORM REGION

by

William A. Gallus

Department of Atmospheric Science
Colorado State University
Fort Collins, CO 80523

This research was supported by the National Science Foundation
under Grant No. ATM–8711649, and a National Science Foundation Graduate Fellowship

Atmospheric Science Paper No. 455

October 1989

Abstract

Rawinsonde data from the 1985 O-K PRE-STORM project are used to calculate the heat, moisture and momentum budgets during the late mature through decaying stages of a large squall line system that occurred on 10-11 June. Rawinsondes are composited to decrease station spacing and allow better resolution of mesoscale features within the system. Low-level radar data and surface accumulated rainfall reports are used to partition the convective system into convective line and stratiform regions, and to check the accuracy of the heat and moisture budgets. Despite the compositing approach, the spacing of the sounding data is inadequate to fully resolve motions in the convective line. The resolution is marginally adequate, however, for motions in the stratiform region.

This squall line had a pronounced rear-inflow jet that advanced toward the front of the system with time, and strong front-to-rear flow at higher levels. Convergence was strong in mid-levels within the stratiform region where the opposing jets met. Divergence at the top of the system weakened markedly as the system decayed. Upward vertical motion also weakened, and the vertical axes of strongest convective line ascent and descent within the stratiform region became increasingly sloped over time.

Heating rates within the overall convective system peaked around 400 mb near the convective line region, and decreased in intensity from over $13^{o}C\ h^{-1}$ to less than $5^{o}C\ h^{-1}$ between 0300 and 0730 UTC. Cooling occurred in the stratiform region and was most intense just behind the back edge of the radar echo around 550 mb, just above the melting level. Peak cooling rates increased from over $3^{o}C\ h^{-1}$ to $6^{o}C\ h^{-1}$ between 0300 and 0600 UTC, and then decreased to $4^{o}C\ h^{-1}$ at 0730 UTC. Drying rates peaked also in the convective line region, but at lower levels than the heating rates. Moistening due to evaporation was typically strongest around 700 mb in

the stratiform region. Vertical integrations of both budgets produced rainfall rates generally close to the observed ones for averages over the entire system. However, precipitation in the leading convective line was underestimated by 40%, due in large part to inadequate sounding data resolution. In the stratiform region the diagnosed precipitation rates underestimated the observed by as much as 2 or 3 $mm\ h^{-1}$ as the system decayed. Radar reflectivity data showed that the rearward transport of hydrometeors could add as much as 2 - 4 $mm\ h^{-1}$ to the diagnosed stratiform rates. The transport, in addition to liquid water storage, could account for the underestimations in the diagnosed rates. The fact that the underestimate in the stratiform region did not occur at 0300 UTC suggests that vertical motion in the convective line was aliased into the stratiform region significantly at this earlier time. Less aliasing may have occurred later as the leading line weakened and the separation between it and the stratiform region increased. In general, the location of predicted rainfall and the temporal trend of the heating and moistening rates matched observations well, establishing the credibility of the budget studies.

A strong mesolow existed at mid-levels within the stratiform region of the system, and the momentum budget showed pressure gradient accelerations were generally front-to-rear. Coriolis accelerations and internal turbulent stresses generally opposed the pressure gradient, and the resulting observed accelerations became weak, with increasing rear-to-front acceleration at high levels as the system weakened. The pressure gradient increased the vertical shear of the component of the wind normal to the line, but as the system decayed, the turbulent stresses began to oppose the increase in shear.

ACKNOWLEDGEMENTS

I wish to extend my sincere gratitude to Dr. Richard H. Johnson, my advisor, who seemed to always be available for guidance, encouragement, and thoughtful criticism of this research. Additional thanks goes to my other committee members, Dr. Steven Rutledge and Dr. Reza Zoughi.

Special appreciation is given to two colleagues, Gregory Stumpf and James Bresch, who spent countless hours teaching me the details of the computer systems in use within the Atmospheric Science Department. They had an impressive task ahead of them, and accomplished it with much patience.

I would also like to thank others who assisted me at different points during the past two years, including Dr. James Toth, Sue Chen, Mike Vescio, and Rolf Hertenstein.

The final manuscript was prepared by Gail Cordova, and some of the figures were drafted by Judy Sorbie. This research was supported by the National Science Foundation Grant No. ATM-8711649, and a National Science Foundation Graduate Fellowship.

TABLE OF CONTENTS

LIST OF FIGURES

LIST OF TABLES

Chapter 1

INTRODUCTION

The accurate parameterization of the effects of organized mesoscale convective systems (MCSs), such as midlatitude and tropical squall lines, on the large-scale fields of heat, moisture and momentum for large-scale models is an ongoing problem in numerical weather prediction. Tropical convection and its impact on synoptic scales has been studied often (e.g., Houze and Betts, 1981), with less attention given to midlatitude systems. Among the first to show the essential role that deep cumulus clouds played in the atmospheric heat balance were Riehl and Malkus (1958). They argued that nearly all of the upward heat transfer in the equatorial regions took place within tall cumulonimbus clouds where released latent heat of condensation was transported to high levels of the troposphere. Since that time, numerous field projects have been conducted allowing more intensive study of convection, both in the tropics and middle latitudes. These studies have shown that convection is frequently organized on the mesoscale.

Organized convection can cover broad areas in the form of non-squall cloud clusters (e.g., Esbensen *et al.*, 1988), or exist more in the form of a band, or squall line. Fujita (1955) stated that a squall line starts from a point and expands its area of influence as it organizes into a mesoscale system. A squall line typically consists of a narrow band of intense convection found along its leading edge, with a broad region of lighter, widespread stratiform precipitation trailing it (Houze and Hobbs, 1982). The system often grows to over 400 km in horizontal extent and resembles the cloud clusters found in the tropics. Because these squall line systems contain both convective regions and stratiform regions, with very different dynamic and microphysical processes operating within them, the influence of MCSs on the tropospheric heat balance may be more complex than first theorized.

One valuable dataset that allowed intensive research into the effects of tropical squall lines on the large-scale environment came from the GARP Atlantic Tropical Experiment (GATE) of 1974. Many GATE studies showed that a mesoscale precipitating stratiform cloud, referred to as a mesoscale anvil (after Brown, 1979), was common within tropical cloud clusters and squall lines (Houze, 1977; Zipser, 1977; Leary and Houze, 1980; Johnson, 1980; Gamache and Houze, 1982, and others). These mesoscale anvils were found to contain updrafts on the order of 10 $cm\ s^{-1}$ with evaporatively-driven mesoscale downdrafts below cloud base (Zipser, 1977; Gamache and Houze, 1982; Johnson, 1982). Figure 1.1 is a conceptual model of a typical convective system, in this case, for a midlatitude system, with mesoscale motion in the stratiform region (from Houze *et al.*, 1989). Because of the large areas covered by the anvils, 40% or more of the precipitation produced by squall systems can be from the stratiform component (Cheng and Houze, 1979). Therefore, a significant amount of the heat and moisture transport in mesoscale convective systems (MCSs) occurs in the precipitating stratiform cloud associated with the systems (Gamache and Houze, 1982).

The GATE experiment resulted in the first attempts to explore the differences in the heat and moisture budgets between the intense convective line portion of squall lines and the larger stratiform regions with them. The first budget studies of tropical cloud clusters (Yanai *et al.*, 1973) showed warming throughout the troposphere for the convective systems, viewing them as a single entity. Because early budgets were done on large spatial and temporal scales, the small-scale processes within the cumulonimbus clouds were not resolvable, and processes operating outside the intense convection were blended into the budget results for the convective systems. Although the convective elements of the squall line are not accurately resolved by mesoscale budgets, the budgets of the convective line region do show heating and drying throughout the troposphere, with smaller magnitudes than those that would be found if data were available on these small scales. The stratiform region, however, operates more on the mesoscale, and budget results closer to actual values can be obtained. The stratiform region is characterized by two differing mesoscale vertical motions which produce budget results distinctly different from those in the convective

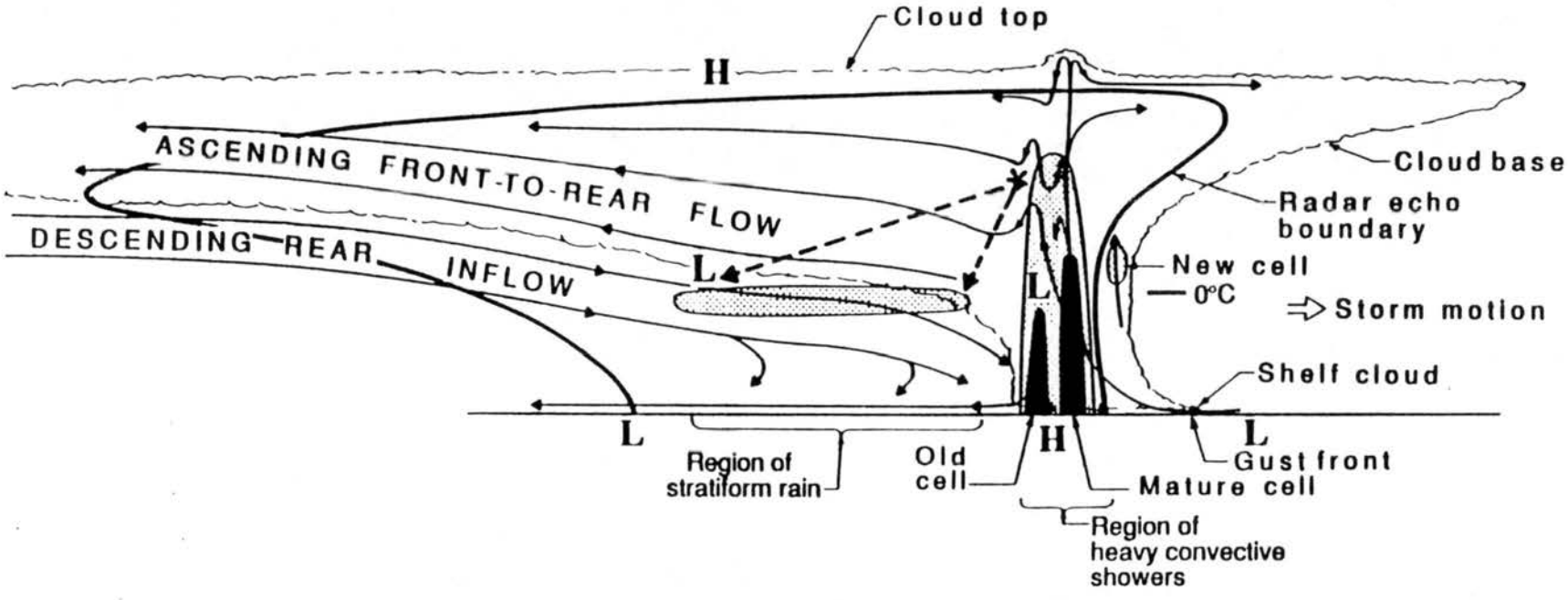

Figure 1.1: Schematic diagram of a typical squall line system having a trailing stratiform region. (From Houze, *et al.* 1989).

region. Gamache and Houze (1982) used sounding winds to compute vertical velocities in the different regions which were partitioned using radar data. They showed a mesoscale downdraft beneath the anvil having maximum intensity at 850 mb, a mesoscale updraft strongest at 300 mb, and a convective line updraft peaking at 650 mb. When the data were combined for the entire system, the resulting vertical profile resembled those of the earlier tropical studies (e.g., Yanai *et al.*, 1973). They did not calculate heat and moisture budget terms for that case, but estimates of the apparent heat source term for stratiform regions have been made. Johnson and Young (1983) used Winter MONEX rawinsonde data, and Houze (1982) used cloud structure and precipitation observations to determine the heating term. Figure 1.2 (from Johnson and Young, 1983) shows that both methods indicated cooling at low levels with warming aloft. These profiles differ from those of the earlier studies that looked at tropical convection as a whole.

Although the GATE dataset allowed intensive study of the budgets of tropical convective systems, similar studies on midlatitude convection have not been as common. Midlatitude budgets usually are done over regions of severe storms, on smaller spatial and temporal scales than tropical studies. One of the first attempts to use a more dense rawinsonde network to study the internal structure of a midlatitude squall line in great detail was by Ogura and Liou (1980). By compositing sounding data, they were able to resolve smaller-scaled features not seen before in midlatitude systems. They found strong mid-level convergence to the rear of the leading line of intense convection, with strong ascent at high levels, and descent at low levels roughly 100 km behind the leading convection. Some of these features were typical of tropical squall lines. They did not perform heat or moisture budget analyses with the data.

This study will use a similarly dense rawinsonde network to compare the features of another squall line with Ogura and Liou's (1980) results, and study in greater detail the time evolution of the system as it decayed. In addition, sounding moisture and energy data will be used to compute heat and moisture budgets at three different times as the system weakened. Other moisture and/or heat budgets have been done on midlatitude convection by Lewis (1975), Sanders and Paine (1975), Fritsch *et al.* (1976), McNab and

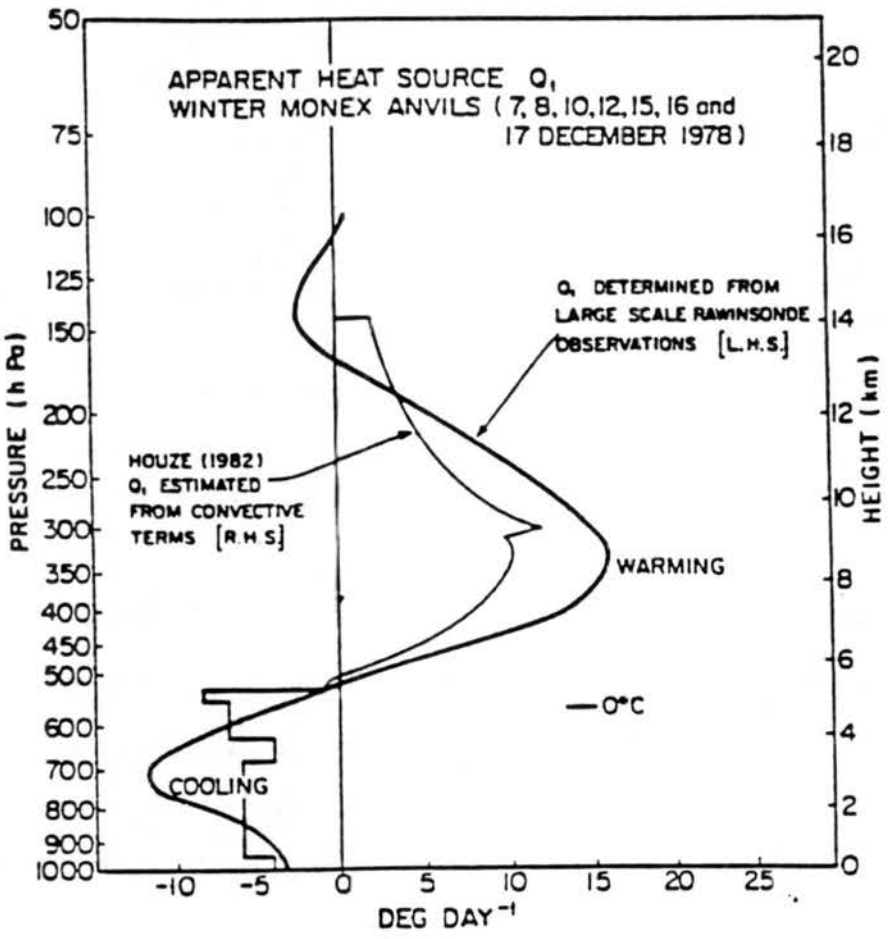

Figure 1.2: Comparison of heat source terms for the stratiform regions of convective systems. (From Johnson and Young, 1983). Heavy curve is inferred from Winter MONEX rawinsonde data by Johnson and Young (1983), and lighter curve is estimated by Houze (1982) from cloud and precipitation observations.

Betts (1978), Ogura and Chen (1977), and Kuo and Anthes (1984) among others. Because these studies are generally done over relatively short temporal scales, the errors in data and limitations of analysis complicate attempts to achieve a high degree of accuracy. On these shorter scales, storage terms in the budget equations can be significant compared to the normally dominant vertical advection term and the source term (Ogura and Chen, 1977; Lewis, 1975; Sanders and Paine, 1975; McNab and Betts, 1978). In this paper, careful consideration will be given to these storage effects.

Momentum budgets have also been done on tropical and midlatitude convection, but these studies are far fewer than heat or moisture budgets. Generally, the component of the wind in the direction of squall line motion is examined. Sanders and Emanuel (1977) studied a midlatitude squall line to compare force balances between the pressure-gradient force, Coriolis force, turbulent stresses and the acceleration. They observed that the mesoscale circulation within the system underwent a noticeable time evolution that may be characteristic of squall lines, and also found that turbulent stresses from the cumulus-scale eddies were as large as the horizontal pressure-gradient force. LeMone (1983) performed a momentum budget analysis of a GATE squall line and also found turbulent forces to be substantial. In that case, the vertical transport of horizontal momentum was found to be against the vertical momentum gradient. Doppler radar data were used by Smull and Houze (1987) to look at some features of the momentum budget of an Oklahoma squall line. They found similar results to LeMone with the vertical transport of momentum increasing the shear of the wind component normal to the line. Rear-to-front flow was accelerated at lower levels while front-to-rear flow was increased at higher levels.

During May and June of 1985, the OK PRE-STORM (Oklahoma-Kansas Preliminary Regional Experiment for STORM-Central) experiment was conducted in the south-central United States to provide an extensive dataset from which midlatitude convective systems could be studied. A rather dense sounding network provided the data necessary to perform budget calculations on the mesoscale level. Previously, a sufficiently dense rawinsonde network to study midlatitude convection was rare. One of the more significant systems to traverse the sounding network occurred on June 10-11 (see Smull and Houze 1987; Johnson

and Hamilton, 1988; Vasiloff and Bluestein, 1988; Johnson and Gallus, 1988; Rutledge *et al.*,1988; Rutledge and MacGorman, 1988; Zhang *et al.*, 1989; Zhang and Gao, 1989; Gao *et al.*,1989). This convective system was a squall line trailed by an extensive mesoscale anvil. With time, the system grew to over 500 km in length, with a 50 km wide convective line of intense thunderstorms trailed by an over 150 km wide region of stratiform rain. The size of this system along with the amount of rain produced within the stratiform region (29%; Johnson and Hamilton, 1988) were similar to those features of a tropical squall line. The internal structure of similar midlatitude systems has been studied by Zwack and Anderson (1970), Sanders and Paine (1975), Sanders and Emanuel (1977), Ogura and Chen (1977), and Ogura and Liou (1980).

It is the purpose of this paper to use the PRE-STORM sounding data to perform mesoscale heat, moisture and momentum budgets on the June 10-11 system, to show small-scale variations within the MCS, compare the heating and moistening rates with tropical systems and document changes in the rates as the system decayed. Because the validity of the heat and moisture budgets can be checked by a comparison with actual rainfall rates, such a comparison will also be shown. A similar independent check of the momentum budget cannot be made, but results from this case will be compared with several other studies.

Chapter 2

BUDGET EQUATIONS AND COMPUTATIONAL METHODS

2.1 Budget equations

Cumulus convection occurs on scales smaller than those normally resolvable from data gathered by conventional means, and therefore, its effects on the larger-scale circulation cannot be directly measured. Instead, effects are inferred indirectly from diagnostic budgets. Cumulus convection transports heat and moisture vertically, and numerous budgets have been done to observe heat and moisture profiles within convective systems. Momentum is also transported in the vertical by convection, but because of difficulties in accurately determining the horizontal pressure gradient, and a lack of an independent method of verification, few momentum budgets have been done (Sanders and Emanuel, 1977; LeMone, 1983).

This study examines not only the heat and moisture budgets, but also the momentum budget of the June 10-11 squall line. The equations of mass continuity, heat energy and moisture continuity (Yanai, *et al.* 1973) used are:

$$\overline{\nabla \cdot V} + \frac{\partial \overline{\omega}}{\partial p} = 0 \ , \tag{2.1}$$

$$\frac{\partial \overline{s}}{\partial t} + \overline{\nabla \cdot sV} + \frac{\partial \overline{s\omega}}{\partial p} = Q_R + L(\overline{c} - \overline{e}) \ , \tag{2.2}$$

$$\frac{\partial \overline{q}}{\partial t} + \overline{\nabla \cdot qV} + \frac{\partial \overline{q\omega}}{\partial p} = \overline{e} - \overline{c} \ , \tag{2.3}$$

where an overbar refers to an area average (soon to be defined more precisely) and

$$s \equiv c_p T + gz \ , \tag{2.4}$$

is the dry static energy, q the specific humidity, c the condensation rate, e the evaporation rate of cloud droplets and rain, and Q_R the radiative heating rate. These equations can be rearranged to give

$$Q_1 \equiv \frac{\partial \overline{s}}{\partial t} + \overline{\nabla \cdot sV} + \frac{\partial \overline{s}\,\overline{\omega}}{\partial p} = Q_R + L(\overline{c} - \overline{e}) - \frac{\partial}{\partial p}\overline{s'\omega'} \,, \tag{2.5}$$

$$Q_2 \equiv -L\left(\frac{\partial \overline{q}}{\partial t} + \overline{\nabla \cdot qV} + \frac{\partial \overline{q}\,\overline{\omega}}{\partial p}\right) = L(\overline{c} - \overline{e}) + L\frac{\partial}{\partial p}\overline{q'\omega'} \tag{2.6}$$

where Q_1 represents the "apparent heat source" in the heat budget equation, and Q_2 represents the "apparent moisture sink" in the moisture budget equation.

Primes denote deviations from the horizontal average. In this study, the correlation of vertical eddy velocity components with s' and q' is assumed to be much larger than that of horizontal components within small scale eddies. From Eq.(2.5), it can be seen that Q_1 is a measure of radiative heating, latent heating from net condensation, and the vertical convergence of the eddy transport of sensible heat. In Eq.(2.6), Q_2 is a measure of the net condensation and vertical divergence of the vertical eddy moisture transport. Both the heat source and moisture sink can be expressed in units of heating rate ($^oK\ h^{-1}$) by dividing the equations by c_p. Taking the difference of (2.5) and (2.6) gives

$$(Q_1 - Q_R) - Q_2 = -\frac{\partial \overline{\omega' h'}}{\partial p}, \tag{2.7}$$

where

$$h \equiv c_p T + gz + Lq \,, \tag{2.8}$$

is the moist static energy. Eq. (2.7) is a measure of the convergence of the moist static energy transport (Arakawa and Chen, 1986). If there is no vertical transport from convective processes, $Q_1 - Q_R = Q_2$. Therefore, one indicator of stratiform rainfall is approximately equal Q_1 and Q_2 profiles (assuming a small Q_R; Luo and Yanai, 1984).

Precipitation rates can be predicted from the heat and moisture budgets by integrating Eqs. (2.5) and (2.6) from p_T (cloud top pressure) to p_s (surface pressure) (Yanai *et al.*, 1973). Integration of (2.5) gives

$$\frac{1}{g}\int_{p_T}^{p_s}(Q_1 - Q_R)dp = LP_o + S_o + S_q \ , \tag{2.9}$$

and (2.6) gives

$$\frac{1}{g}\int_{p_T}^{p_s} Q_2 dp = LP_o - LE_o + S_q \ , \tag{2.10}$$

where P_o is the precipitation rate measured as the difference between net condensation and evaporation in the column, and S_q is the storage of liquid water, due both to the transport of liquid water and ice into or out of the grid area, and to temporal changes in stored liquid water. (The surface sensible heat flux, S_o, and surface evaporation term, LE_o, found in Yanai *et al.* are small for midlatitude convection at night and are neglected in the budget computations). Storage effects are minimal when budgets are done over long time scales, but on shorter time scales, they can be substantial (McNab and Betts, 1978). This is especially true for rapidly developing convection where large quantities of liquid water are condensed from vapor but do not fall out at first, or for decaying convection where liquid water production may cease, but water that was stored earlier in the clouds later falls out as rain. Storage can also be considerable in the stratiform region of a system since ice and liquid water can be transported rearward from the convective line.

The vertical eddy flux of total heat, F, at any level can be calculated by integrating Eq. (2.7) downward to that level from the pressure at cloud top (Yanai *et al.*, 1973). If the integration is done over the same limits as that done to (2.5) and (2.6), the vertical eddy flux of total heat at the surface can be determined, and used as an additional check on the accuracy of the budgets. This integration of Eq. (2.7) yields

$$\frac{1}{g}\int_{p_T}^{p_s}(Q_1 - Q_2 - Q_R)dp \equiv F_o = S_o + LE_o. \tag{2.11}$$

Because surface sensible heat flux and evaporation are small for the conditions under which this particular squall line occurred, the vertical eddy flux of total heat at the surface, F_o, should be close to zero.

The momentum budget in this study concentrated on changes in the component of the wind normal to the squall line. This is the component emphasized in studies by Sanders

and Emanuel (1977) and LeMone (1983). The component of the momentum equation in the direction of squall movement,

$$\overline{X} \equiv \frac{\partial \overline{u}}{\partial t} + \overline{u}\frac{\partial \overline{u}}{\partial x} + \overline{v}\frac{\partial \overline{u}}{\partial y} + \overline{\omega}\frac{\partial \overline{u}}{\partial p} + \frac{\partial \overline{\phi}}{\partial x} - f\overline{v} \approx -\frac{\partial}{\partial p}(\overline{\omega' u'}) \tag{2.12}$$

is solved for a residual, $\overline{X}$ (Stevens, 1979), which can be thought of as a measure of the internal turbulent stresses caused by the convection. The acceleration of the wind, Coriolis force and pressure gradient force are computed from the rawinsonde gridded wind data. As will be discussed in the momentum budget chapter, height perturbations within the mesoscale system appeared to be large enough to allow calculation of the pressure gradient force used in Eq.(2.12) from rawinsonde height measurements. In many earlier studies, these perturbations were too small compared to errors in the data to allow such a direct computation (Fankhauser, 1974; Sanders and Emanuel, 1977).

The rawinsonde height measurements used in this study, however, are calculated hydrostatically, using a virtual temperature that does not take liquid water loading into account. The virtual temperature that should be used in the hypsometric equation to provide accurate height measurements in regions of strong radar echoes is defined as

$$T_v^* \equiv \frac{T_v}{1 + q_l}, \tag{2.13}$$

where q_l is the liquid-water mixing ratio, and T_v is the virtual temperature taking only specific humidity into account. Sanders and Emanuel (1977) have determined that the neglect of the liquid water in a column in calculating height measurements from rawinsonde data can cause errors in the pressure field as large as 1 or 2 mb in regions of heavy precipitation. Within the stratiform rain region of convective systems, liquid water loading should not be significant since radar reflectivities are usually low. However, within the convective line region, which consists of strong radar echoes, the failure to include the liquid-water mixing ratio when calculating heights can cause errors that may reach 10 or 20 m at mid-levels. In addition to these errors, other errors in the height measurements can occur in intense convection due to dynamic processes that make the heights non-hydrostatic.

2.2 Computational methods

In the heat, moisture and momentum budgets, finite differences are used to determine horizontal and vertical derivatives, and because the horizontal grid spacing is approximately 50 km, the barred variables represent averages over horizontal areas of 50 × 50 km centered at the grid points. Vertical velocities used in the equations are calculated at each grid point from the kinematic technique using the mass continuity equation. Adjustments are made using a procedure described by O'Brien (1970) to make ω vanish at 125 mb. A linear adjustment, increasing with height, is then made to divergence. The equations used are:

$$\omega_{adj}(p) = \omega(p) - \frac{(p_s - p)^2}{(p_s - p_T)^2}\omega(125) \tag{2.14}$$

$$div_{adj}(p) = div(p) - 2\frac{(p_s - p)}{(p_s - p_T)^2}\omega(125) \tag{2.15}$$

where p_s (surface pressure) is taken as 975 mb, and $\omega(125)$ is the value of ω at 125 mb before adjustment. The tropopause is chosen to be at the 125 mb level because that is the highest tropopause reported within the region, and that is the highest level at which the majority of rawinsondes reported data. Vertical velocities are also calculated at high levels using a different method independent of the kinematic technique (Nitta, 1977). Eq. (2.2) can be re-written as

$$\overline{\omega} = -\frac{\frac{\partial \overline{s}}{\partial t} - \overline{v}\cdot\nabla\overline{s} + Q_R}{\frac{\partial \overline{s}}{\partial p}} \tag{2.16}$$

assuming condensation and evaporation are small which is true in the upper troposphere. Using this equation with reasonable values of Q_R, ω was found to drop off quickly to less than 1 μb s^{-1} at most grid points by 125 mb. Therefore, the choice of 125 mb as the level of zero vertical motion appears to be good.

Chapter 3

DATA SET AND ANALYSIS PROCEDURES

3.1 PRE-STORM

During the period 1 May through 27 June 1985, a field experiment known as the Oklahoma-Kansas Preliminary Regional Experiment for STORM-Central (OK PRE-STORM) was conducted to study in detail the structure of Great Plains mesoscale convective systems. A dense network of surface mesonet stations was established to observe the surface features of these systems. In addition, supplemental soundings were taken over the two-state region in order to study the effects of mesoscale convection throughout the troposphere. Both data-collection networks, along with radar, NWS rawinsonde, and profiler sites can be seen in Figure 3.1. Although this budget study relied most heavily upon the upper air data, radar and surface data were also used to partition the squall line into convective and stratiform sections, and to determine actual rainfall rates at the surface.

3.2 Upper air data

3.2.1 Data network and compositing technique

The upper air network operating during this case consisted of NWS sites and eleven supplemental sounding stations. Soundings were taken from these supplemental sites at approximately 90 minute intervals, and were spaced about 150 km apart. In order to decrease station spacing and increase the amount of data available for budget calculations, soundings were composited over three-hour periods centered at 0300 ,0600 and 0730 UTC, using an estimated squall line motion. It was felt that the best velocity to use for compositing over the entire PRE-STORM region was the average movement of the central

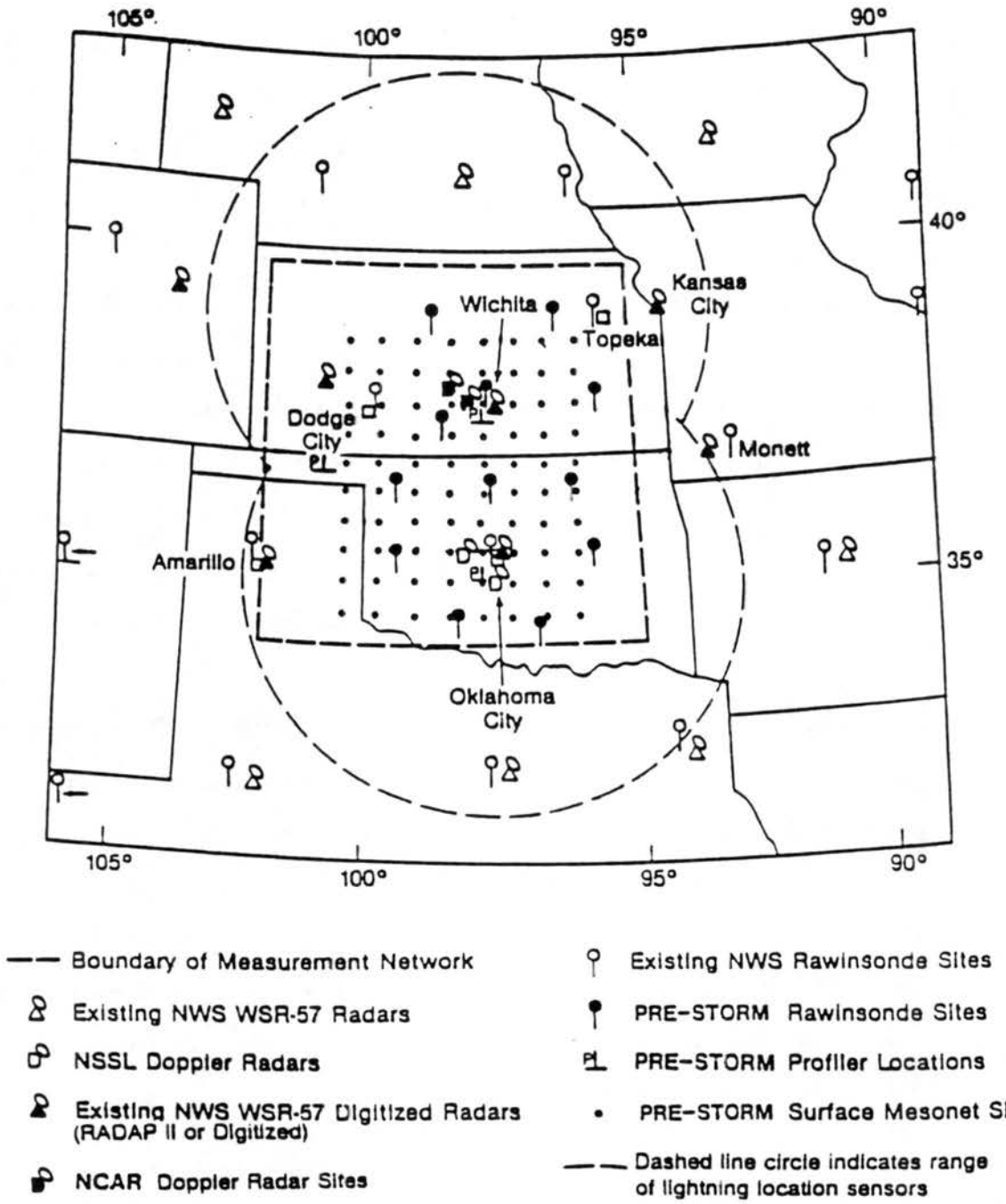

Figure 3.1: The OK PRE-STORM observational mesonetwork (from Meitín and Cunning, 1985).

axis, leading edge, and back edge of the radar echo over each three hour period. This averaging was done since the stratiform region was moving at a slower speed than the convective line. From this procedure, the system appeared to move from 315° on average with a speed decreasing from 16 $m\ s^{-1}$ at 0300 UTC to 13 $m\ s^{-1}$ at 0600 UTC, and then increasing again to 14 $m\ s^{-1}$ by 0730 UTC. A storm motion of 14 $m\ s^{-1}$, the motion of the convective line alone, was assumed during the period from 0130 through 0530 UTC in the Doppler radar study of this case by Rutledge *et al.* (1988). This compositing procedure assumes a steady-state system. Although at this time the squall line was weakening, and precipitation rates were slowing, the three-hour time interval used in compositing was believed to be brief enough to allow the steady-state assumption.

The compositing procedure increased the number of stations used in the analyses and budget calculations to around 30. The station spacing decreased to approximately 80 km. The locations of the composited soundings for all three time periods, along with the outlines of the radar echoes can be seen in Fig. 3.2. In general, rawinsondes adequately sampled the atmosphere not only within the convective system, but also ahead of and behind it. Figure 3.2 also shows the level at which the rawinsondes terminated. Within the convective system, especially in the stratiform rain region, data from the soundings often ended in the 450-650 mb layer. NWS soundings were included in the analyses only when they were taken within the three-hour time interval and were needed to help fill data-sparse areas. A few bogus soundings were included at 0600 UTC, and these are shown with circles. The justification for these additional soundings can be found in the next section. Balloon drift, which is important on this scale (Fankhauser, 1974), was also figured into the locations of the reported data at all levels.

3.2.2 Treatment of and adjustments to upper air data

Sounding data used in the budget calculations were interpolated to 25 mb levels, and checked for spurious features. Where these features occurred over a small vertical layer, inaccurate data were replaced by values interpolated from outside the layer. Specific humidity and dry static energy data used in the moisture and heat budgets were calculated from the sounding data and then smoothed in the vertical with a 1-2-1 filter.

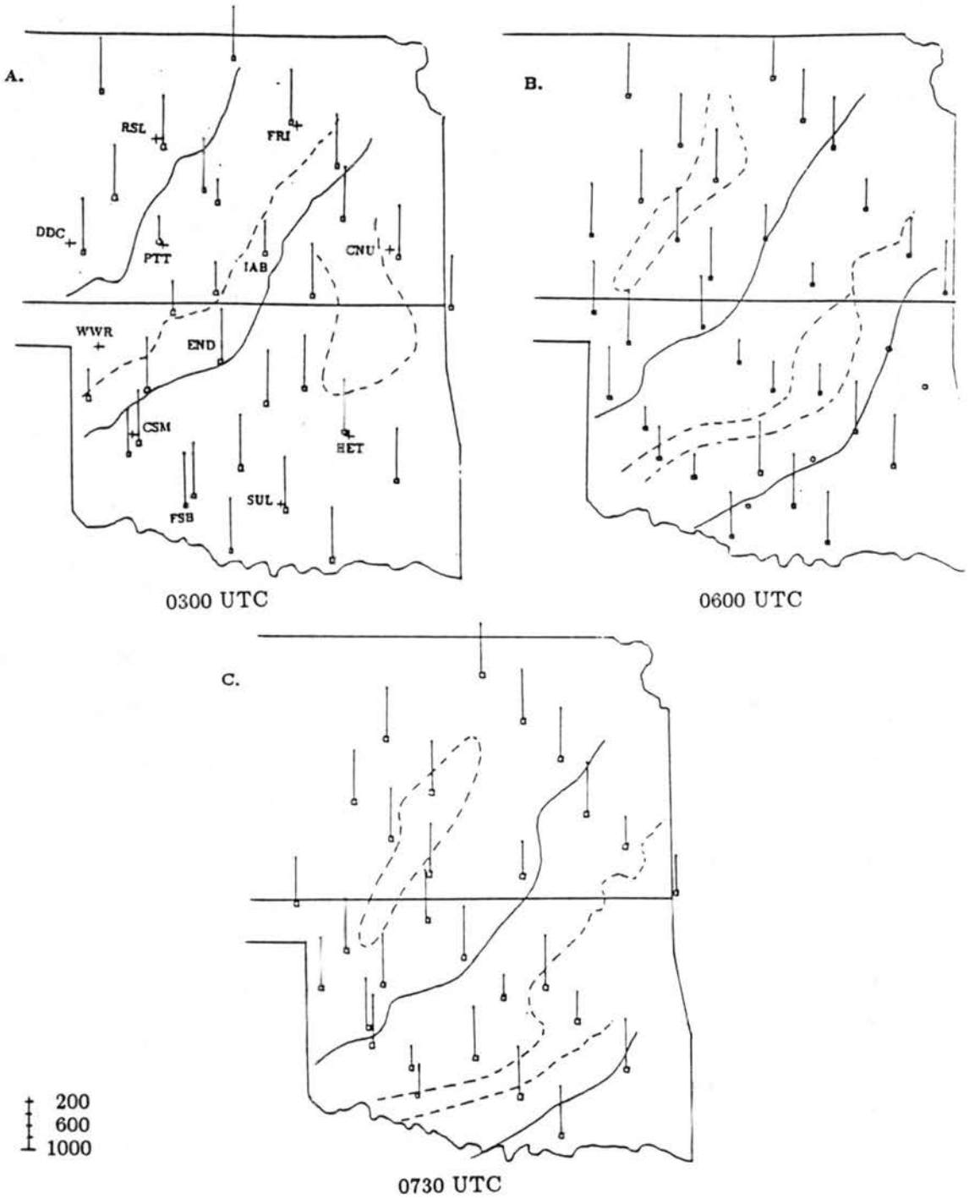

Figure 3.2: Locations of composited soundings used in the budget studies at a.) 0300, b.) 0600, and c.) 0730 UTC. Squares represent rawinsonde sites, and circles mark locations of bogus soundings. The length of the vertical line at each station is proportional to the balloon ascent distance. The composited radar echo is marked with a solid line, and dashed lines divide it into stratiform and convective precipitation sections. The region between the dashed lines in b.) and c.) is the transition zone. Dashed lines outside the squall line mark regions of scattered small echoes. Station names are shown at 0300 UTC.

Because the average sounding spacing of the composited data was around 80 km, small-scale features could not be resolved in the analyses, and aliasing of data from one distinct region into another was common. At all times this aliasing meant that the small convective line features were not adequately resolved and these features were smoothed to some degree into the stratiform region (e.g., aliasing of negative omega into the stratiform mesoscale downdraft). The most obvious problems arose at 0600 UTC when aliasing of specific humidity data from ahead of the squall line into the convective region appeared to adversely affect budget results in that part of the system. Therefore, four bogus soundings were included into that composite time. One was placed equidistant between two pre-squall soundings into a region where the spacing significantly exceeded the average over the PRE-STORM region. Sounding parameters for this station were taken as the average between the pre-squall soundings to the north and south of it. In general, the winds, humidity, and temperature were similar at the two real soundings, and the inclusion of this bogus point helped to prevent aliasing of convective line values into the pre-squall environment near the edge of the grid. The other three bogus soundings were added into the leading-edge of the convective line, and were assumed to have a nearly-saturated profile like that of the Chanute 0535 UTC sounding. The justification for these soundings can be found in Appendix A.

3.2.3 Objective analysis procedure

Data from the 30 or so PRE-STORM rawinsondes used at each composite time were gridded onto a $1/2^o$ by $1/2^o$ grid using a Barnes objective analysis scheme (Barnes, 1964). The program used allowed the radius of influence to be adjusted to allow a balance between the amount of smoothing done and the amount of points where data would be assigned a missing value. The response function curves associated with the objective analyses at different vertical levels are shown in Fig. 3.3. The lower troposphere curve is representative of analyses done below approximately 400 mb, and the upper troposphere curve is that associated with analyses above 400 mb. According to Barnes (1973), features smaller than twice the average station spacing should be filtered out, and the percent of the amplitude of the smallest definable scale depicted in an analysis should be adjusted to filter noise.

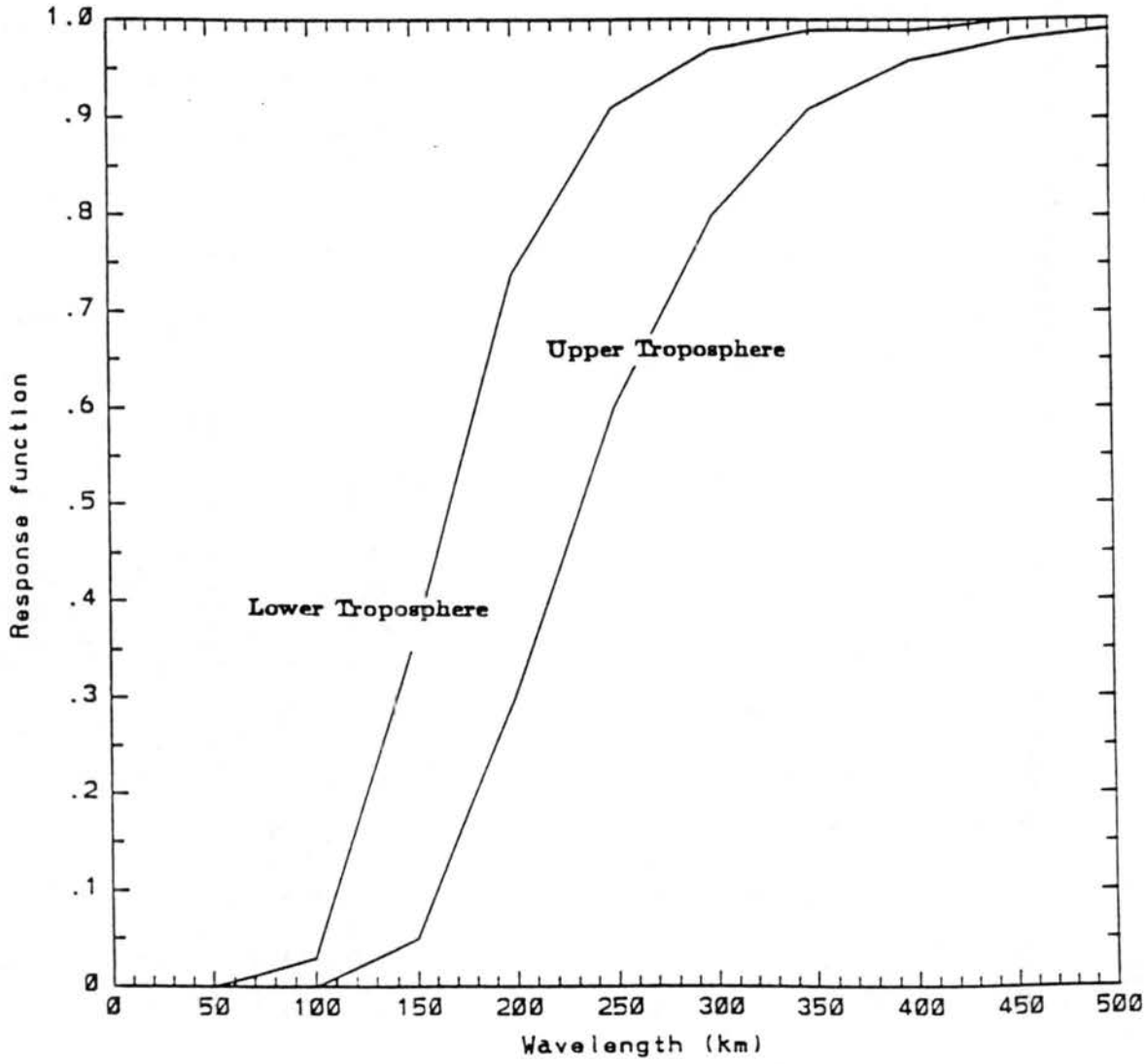

Figure 3.3: Response function curves as a function of horizontal wavelength for Barnes objective analyses in the lower and upper troposphere.

In this analysis, the average spacing of the data points was roughly 80 km at low levels. Therefore, a response of approximately 50% at 160 km was desired, to reduce noise. At higher levels where data were missing, the average station spacing increased, and therefore, the smallest scales accurately resolvable increased toward 250 km. Ooyama (1982) shows that a horizontal scale of 160 km falls within those typically found in mesoscale convective systems. Convective cells occur on scales of a few kilometers to several tens of kilometers at most, so the structure of individual cells is not resolvable in these analyses. The mesoscale anvil with this system was over 160 km wide, and its structure therefore should be fairly accurately resolved by the analyses. The convective line portion of the system was generally closer to 50 km wide, and therefore it is not as accurately represented by the analyses as the stratiform region. Because of the small scale of the convective line region, magnitudes of quantities like vertical velocity are underestimated to a large degree in this area. Since this is a common problem (Ogura and Liou, 1980; Kuo and Anthes, 1984), though, relative comparisons can still be made between other cases.

Because the PRE-STORM region slopes significantly (undisturbed surface pressures fall from around 980 mb in the east to 930 mb in the west), lower pressure levels often intersected the surface. At these levels (950 mb and 975 mb), an objective analysis was done using surface data for stations where that level was below the surface. Then, for the wind components, values were set to zero west of a line that approximated the surface. The 950 mb level was assumed to intersect the surface at 99° W, and the 975 mb level at 96° W. Since terms involving the vertical velocity tend to be the largest in the budget equations, omega was checked to see the difference that a sloped versus non-sloped surface would cause. The non-sloped surface was assumed to be at 975 mb, with surface data assumed to represent the below-surface pressure levels at stations where 975 mb was below ground. Differences in the west where the surface is highest and the pressure lowest were on the order of a few microbars per second. Since typical descent in the mesoscale downdraft and ascent in the convective line and mesoscale updraft were on the order of tens of microbars per second, the differences were not significant, especially in light of the inherent errors in the rawinsonde winds used to compute omega.

Throughout this study, vertical cross-sections are presented that condense the three-dimensional squall-line into two dimensions by taking averages of variables at grid points that lie roughly equidistant from the leading edge of the system. Bands 50 km wide were taken on both sides of the leading edge of the squall line, and all grid points lying within the bands were used to compute average values of a particular variable. This procedure is analogous to that used by Ogura and Liou (1980). These values were then assumed to be representative of the state of the atmosphere at these distances ahead of and behind the leading edge of convection. Since the line was basically two-dimensional, this procedure helped to maximize the amount of data used in the figures without distorting the true meteorological situation in the vicinity of the system. Other figures showing horizontal cross-sections across the system depict smaller features missed by the averaging used in the vertical cross-sections, and these reveal the three-dimensionality within the squall line. In general, the line is similar to the highly two-dimensional ones studied by Sanders and Paine (1975) and Ogura and Liou (1980).

3.3 Radar data

Radar data from the NWS WSR-57 radars located at Wichita KS and Oklahoma City OK were used in this study. Smull and Houze (1985) have identified three main features in the low-level reflectivity field for a squall line with a trailing stratiform region: a leading convective line (10-50 km in width having heavy rainfall), a transition zone (weak reflectivity with little or no surface precipitation, due to increased evaporation and the bimodal size distribution of hydrometeors and their differing fallspeeds) and the trailing stratiform region (100-300 km in width, having light to moderate surface rainfall, 1-10 $mm\ h^{-1}$). Gamache and Houze (1982) were the first to partition a convective system into stratiform and convective line regions using radar data. In this paper, a different technique using the low-level radar reflectivity images was used to partition the system into those regions. The back edge of the convective line region was approximated by the 25dBZ contour, and the front edge of the stratiform region was assumed to lie where the reflectivity values began increasing behind the convective line. A simple composite was

made at each analysis time by taking the average position of the leading edge of radar echo at the beginning, middle, and end time of the three-hour interval. The same procedure was used to determine the position of the back edge of radar echo, the leading edge of the stratiform rain region, and the back edge of the convective line region. The evolution of the composited echo can be seen in Fig. 3.2. At 0300 UTC, a transition zone was not yet wide enough to appear in the composited echo. (The CP-3/CP-4 Doppler radars did indicate a well-defined transition zone well before 0300 UTC.) By 0600 UTC, a transition zone, nearly as wide as the convective line, was located between the two regions, and by 0730 UTC, the gap between the two regions had more than doubled in area. Grid points lying within the different regions were averaged to present the stratiform, convective line, and total system components of meteorological variables used throughout this study.

3.4 Surface data

Unlike other observational studies of PRE-STORM MCSs, (Johnson and Hamilton, 1988; Stumpf, 1988; and others), this budget study concentrated on upper air data far more than surface data, and therefore relied little on the PRE-STORM surface mesonetwork. The 84 automated observing platforms which were spaced about 50 km apart were used to calculate an observed precipitation rate. These stations measured accumulated rainfall, from which rates were calculated and compared in the study with vertically-integrated budget estimates.

Chapter 4

MESOSCALE FLOW AND THERMODYNAMIC STRUCTURE

The June 10-11 squall line grew to maximum intensity while almost centered within the PRE-STORM data network, and therefore has been the subject of numerous studies. The convective system had a very well-developed flow structure with a pronounced rear-inflow jet, and strong front-to-rear inflow from the southeast. The purpose of this chapter is to show how the wind field, divergence, vertical velocities, and temperatures within the system evolved from 0300 UTC through 0730 UTC, roughly during its mature to decaying stages, and to compare its structure with similar squall lines having trailing stratiform regions.

4.1 Squall line history

The June 10-11 squall line began as "broken line" convection (see Bluestein and Jain, 1985) over southwestern Kansas and the Oklahoma panhandle ahead of a cold front before 2100 UTC on June 10, and later grew to include a transition zone and broad stratiform rain region as it passed through the PRE-STORM network. The convective line portion of the system intensified, and reflectivity values peaked around 0300 UTC, the first composite time considered in this budget study. At this time, a broadening stratiform rain region could be seen on radar images. Figure 4.1 shows radar images taken at various times during the life cycle of this squall line. After 0300 UTC, the leading edge of the system showed a decrease in reflectivity values, while the stratiform region increased in size through 0600 UTC, the second budget study time. The convective line and stratiform echo gradually separated during this time, and a transition zone of near-zero low-level reflectivities broadened between them. After 0600 UTC, the entire system began to decrease markedly in intensity. The third budget time, 0730 UTC was

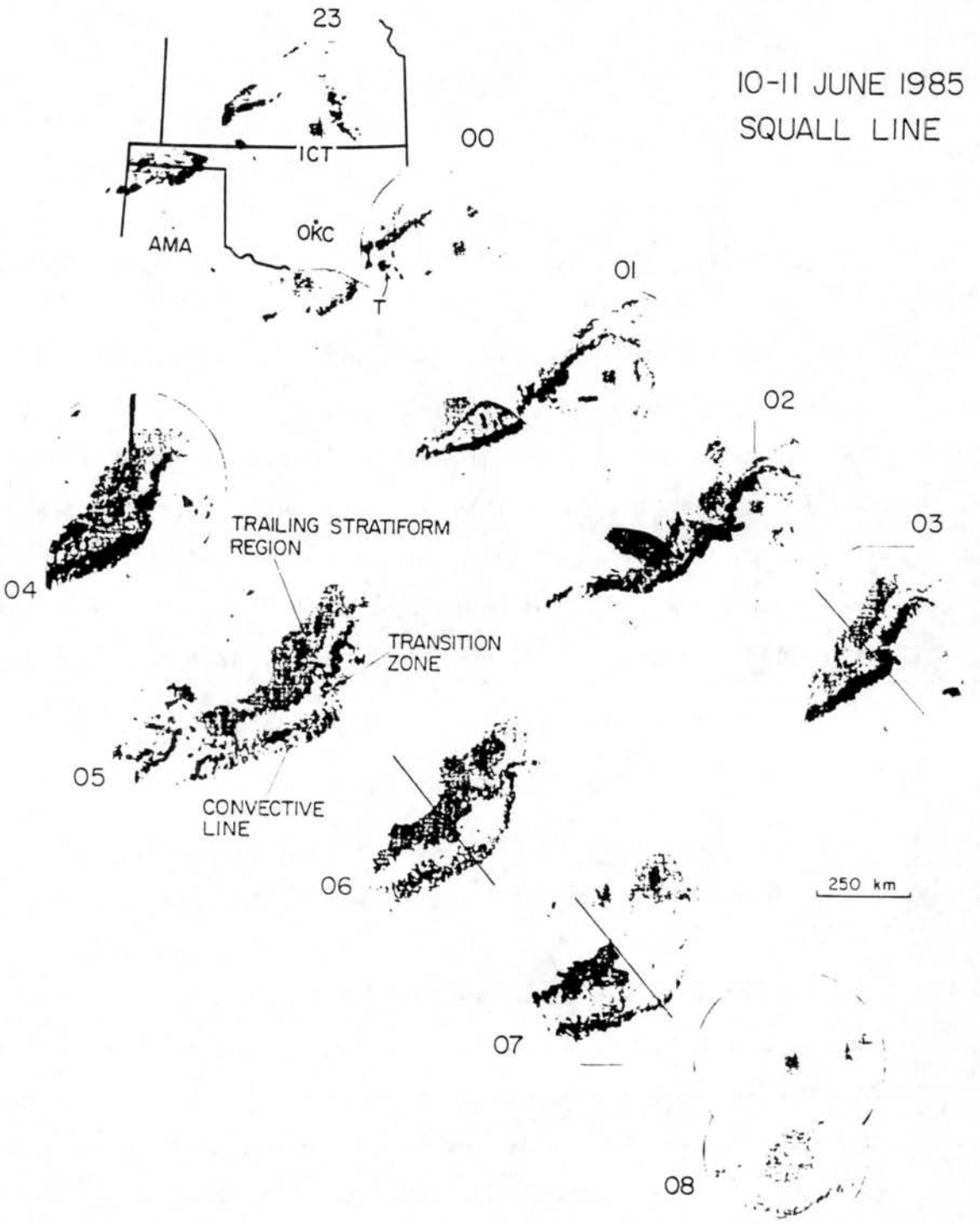

Figure 4.1: Composited hourly low-level reflectivity displays during the lifetime of the June 10-11 squall line. From Johnson and Hamilton (1988). Upper diagonal from 2300-0300 UTC, and lower diagonal from 0400-0800 UTC. Reflectivities shaded from lightest to darkest for 15, 25, 35 and 50 dB(z). Lines at 0300, 0600 and 0700 UTC show the axes on which the 50 km strips used in the vertical cross-sections are centered.

during this period of fairly rapid decay. A more detailed description of the squall line history, along with the synoptic situation can be found in Johnson and Hamilton (1988).

4.2 Relative winds

The airflow within the June 10-11 squall line consisted of a series of well-developed mesoscale jets. A strong front-to-rear jet carried moisture and heat from low levels ahead of the system through the convective line and out the rear of the system through the trailing anvil. A rear-inflow jet entered the stratiform region at mid-levels and descended toward the convective line, where relative flow from rear-to front eventually reached to within 1 km of the surface. Another front-to-rear jet, the result of an overturning downdraft fed by divergence underneath the stratiform region, cut under the rear-inflow and had peak intensities within 100 mb of the surface. These jets have also been documented using profiler and Doppler data in addition to the rawinsonde data by Augustine and Zipser (1987), Smull and Houze (1987), Johnson and Hamilton (1988) and Rutledge *et al.* (1988). Figure 4.2 shows the evolution of the system-relative flow along the direction of motion during the three budget times considered in this paper. The squall line motion used in compositing was subtracted from the gridded wind components to compute relative velocities. Values shown in the figure are the averages along 50 km strips at the given distances away from the leading edge of the radar echo, as described in chapter three. These strips are centered along axes shown by the lines indicated in Fig. 4.1. Because the values shown are averages, the magnitudes of windspeed are less than those found in this same system using other methods such as Doppler radar (Smull and Houze, 1987). However, some grid point values taken within regions of strong flow were approximately equal to those obtained using Doppler methods (Rutledge *et al.*, 1988).

At 0300 UTC (Fig. 4.2a), when the convective line was most intense, strong front-to-rear flow can be seen at low levels ahead of the system (nearly 24 $m\ s^{-1}$ at 900 mb), and at high levels over the stratiform region (over 28 $m\ s^{-1}$ at 250 mb). The rear-inflow jet at this time, averaged for the cross-section, was rather weak (less than 4 $m\ s^{-1}$) and did not extend far down from mid-levels where it entered the stratiform

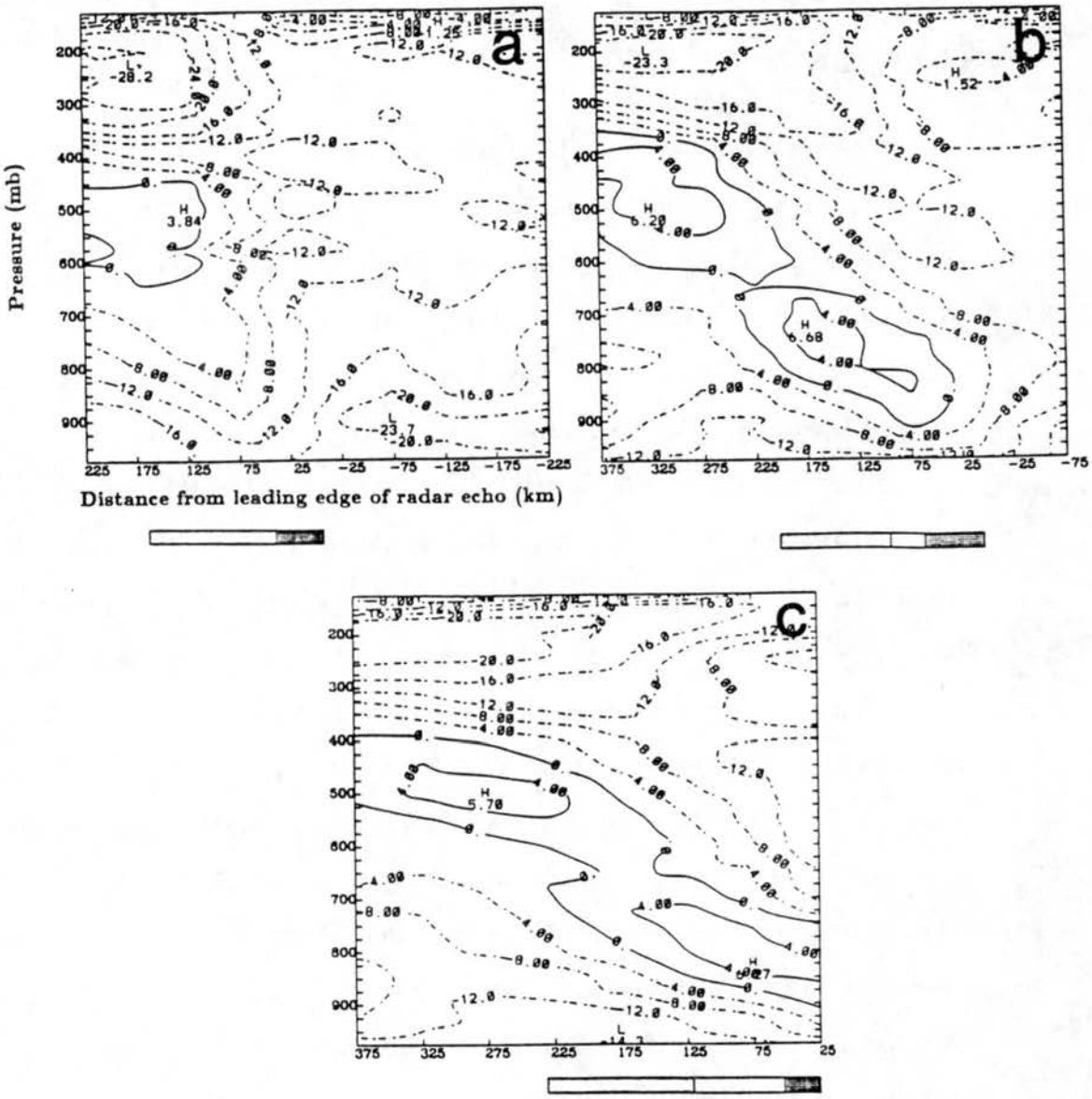

Figure 4.2: Component of the relative wind (in $m\ s^{-1}$), normal to the squall line for a.) 0300 UTC, b.) 0600 UTC and c.) 0730 UTC June 11. Positive numbers indicate flow from rear to front (left to right). Approximate locations of convective region (darkest shading), stratiform region (lighter shading) and transition zone (no shading) are shown in the bar below each figure.

region. The two-dimensional figure is somewhat misleading at this time, because a rear-inflow jet could be found with speeds locally of over 10 $m\ s^{-1}$ at 500 mb; however, it was very narrow compared with its size at later times, and much weaker flow was found to its right and left. In addition, the convective system was still close to the western edge of the data network at 0300 UTC, so the lack of much sounding information to the rear of the system may have prevented accurate measurement of the strength and size of the jet. Smull and Houze (1987), Rutledge *et al.*, 1988, and Houze *et al.*, 1989, using Doppler radar data, and Augustine and Zipser (1987), using wind profiler data which could resolve scales much smaller than the rawinsonde data, also found speeds of 10 $m\ s^{-1}$ or more in a well-established rear-inflow jet at or shortly after this time.

By 0600 UTC, when the system was centered best within the data network and the stratiform region was most widespread, the rear-inflow jet is quite apparent extending from around 400 mb at a distance of over 100 km behind the back edge of radar echo down to 850 mb within the convective line (Fig. 4.2b). Rutledge *et al.* (1988) also found from single Doppler radar analysis that this jet existed at very high levels, above 400 mb, at the rear of the system and descended to low levels near the convective line. With the exception of having a slightly steeper slope from the vertical, the location of the jet relative to the squall system at 0600 UTC and its magnitude are nearly identical to that found in the squall line studied by Ogura and Liou (1980). Peak velocities were generally 6-7 $m\ s^{-1}$ in two regions. One was near the back edge of the stratiform region, and the other at a higher level behind the radar echo. Some point values reached 15 $m\ s^{-1}$. Within the stratiform region, the axis of the jet sloped downward, lying generally within 1 km of the melting level which was approximately 625 mb. The axis of the jet was also found to descend beneath the anvil cloud across the melting level, or bright band within the radar reflectivity field, by Smull and Houze (1987). The front-to-rear flow can be seen ahead of the rear-inflow jet, and the strength of this flow at high levels had weakened since 0300 UTC, a result also found by Zhang and Gao (1989).

At 0730 UTC, the convective line portion of the system was rapidly weakening and was beginning to break into segments as it left the eastern edge of the mesonetwork. Therefore,

the front-to-rear inflow can only be seen at middle and high levels on the cross-section (Fig. 4.2c). The rear-inflow jet at this time continued to be quite pronounced with no real weakening from 0600 UTC. Again, two speed maxima existed, and each was centered roughly 50 km ahead of its 0600 UTC position relative to the leading edge of the radar echo. The jet can be seen extending from mid-levels several hundred kilometers behind the back edge of radar echo in a continuous current toward the leading edge of the echo, which was east of the data network. This extensive current beginning far behind the system was also found in the modelling study of this case by Zhang and Gao (1989). Smull and Houze (1987) have suggested that processes operating in two different areas of the system may work together to produce this extensive rear-inflow jet. Accelerations due to pressure gradients are caused by both a hydrostatically induced mesolow that forms immediately under and behind the warm convective updrafts (LeMone, 1983), and another mesolow, also generated hydrostatically, within the stratiform region (Brown, 1979; Johnson and Gallus, 1988). Pressure gradient forces directed toward the two lows, along with the vertical flux of horizontal momentum in the convective line region (LeMone, 1983) may develop this type of extensive strong rear-inflow jet. This will be discussed in more detail in Chapter 6, along with the height fields associated with this system.

It therefore appears that the rear-inflow jet, which may have been present prior to this analysis (Zhang and Gao, 1989), began to strengthen and descend at the time the system began weakening, and reached its maximum intensity three hours or more after the leading convective line had reached its peak intensity. Smull and Houze (1985) noted a similar development with the formation of such a jet when the 22 May 1976 Oklahoma squall line began weakening. Eventually, the leading edge of the jet approached and overtook the gust front. At all three times examined in this study, no rear-to-front flow was present at high levels ahead of the line, although at 0300 UTC (around 150 mb), and at 0600 UTC (near 250 mb), a stagnation zone with near-zero velocities was located near the leading edge of the system. The lack of rear-to-front flow in this area is consistent with the observed absence of a leading anvil cloud.

4.3 Divergence and vertical motion

The opposing jets in this system helped to produce strong mid-level convergence throughout the time period of this study. This convergence, occurring at or above the 0°C level in many regions, may also be related to the downward motion occurring below that level due to the melting of ice and evaporation of falling rain. Figure 4.3 shows the evolution of convergence/divergence within the system. The strongest convergence, $\approx 1.7 \times 10^{-4}\ s^{-1}$ at 0300 UTC, occurred at 900 mb near the leading edge of the system, with nearly as strong convergence sloping rearward with height just above the same region as occupied by the rear-inflow jet. The mid-level convergence was strongest in a layer just above the melting level, a result also found by Rutledge *et al.* (1988). The low-level and mid-level convergence peaks were in the same positions relative to the leading edge of the system as those found in Ogura and Liou (1980); however, the intensities were less because the spacing of the rawinsonde sites used in this analysis was greater than that used by Ogura and Liou. Strong divergence, $\approx 1.0 \times 10^{-4}\ s^{-1}$, can be found at low levels in the stratiform region, below the rear-inflow jet. This band of divergence increased in size as the system decayed. Strong divergence can also be found at the top of the system, and this divergence weakened markedly with time. The center remained in the stratiform region. The high level divergence was stronger, especially at 0300 UTC, than that found by Ogura and Liou. The alternating bands of convergence and divergence in the vertical were also detailed by Smull and Houze (1987) using Doppler radar on this case, and by Srivastava *et al.* (1986) in a study of another midlatitude squall line. The increasing tilt of the convergence axis is consistent with the radar observations showing an increasing separation between the convective line and stratiform rain regions.

Upward motion in the squall line is shown in Fig. 4.4. This figure illustrates the weakening of upward motion as the squall line decayed. Upward vertical velocities decreased from a peak of 45 $\mu b\ s^{-1}$ (85 $cm\ s^{-1}$) at 400 mb at 0300 UTC to only 25 $\mu b\ s^{-1}$ (45 $cm\ s^{-1}$) at 450 mb by 0600 UTC. The upward motion at 0300 UTC was more intense than that found in Ogura and Liou (1980), 30 $\mu b\ s^{-1}$, but the 0600 UTC values were closer, since both squall lines were probably in a similar state of dissipation at that time.

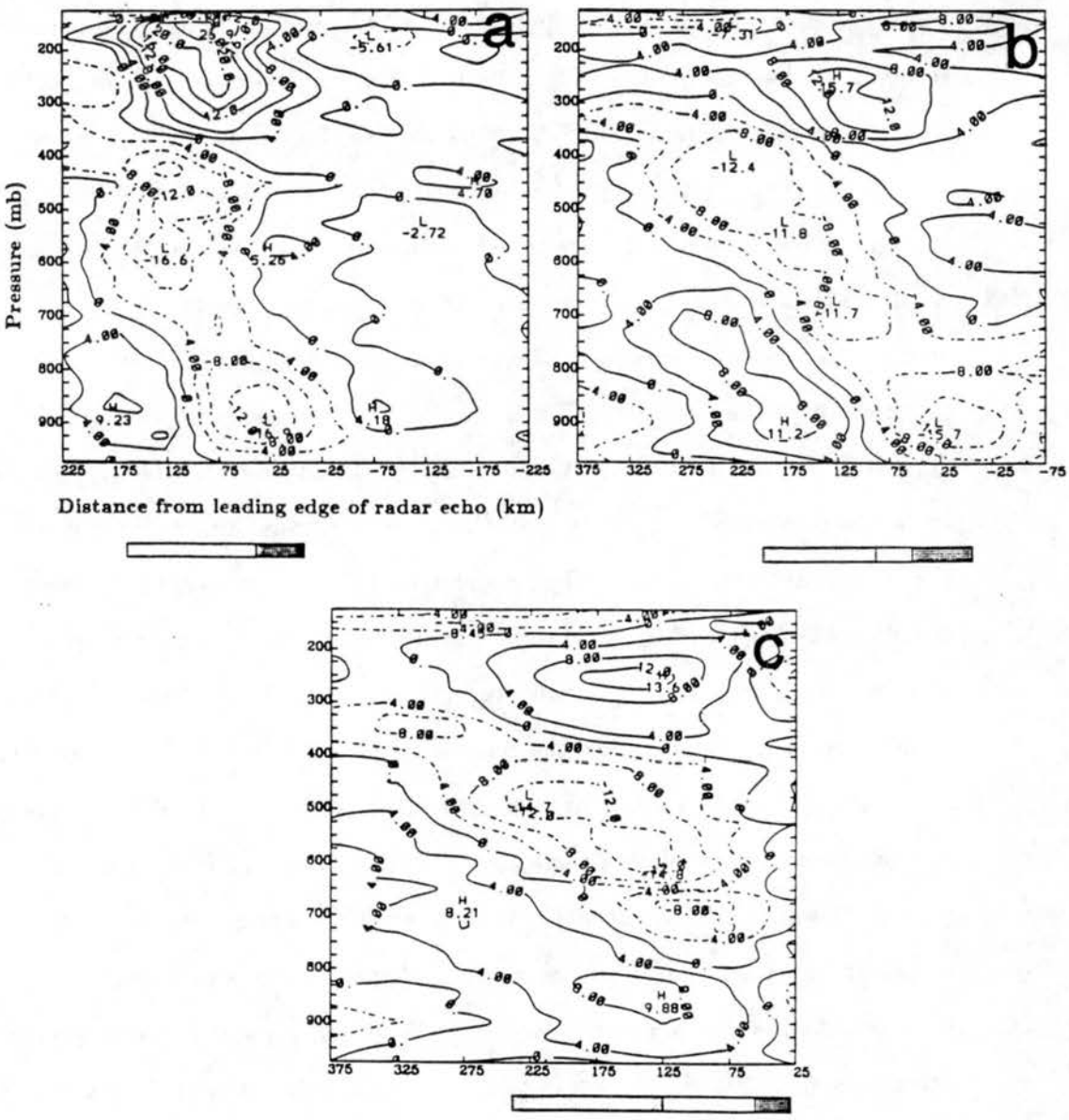

Figure 4.3: As in Fig. 4.2 except for divergence, in units of $10^{-5}\ s^{-1}$.

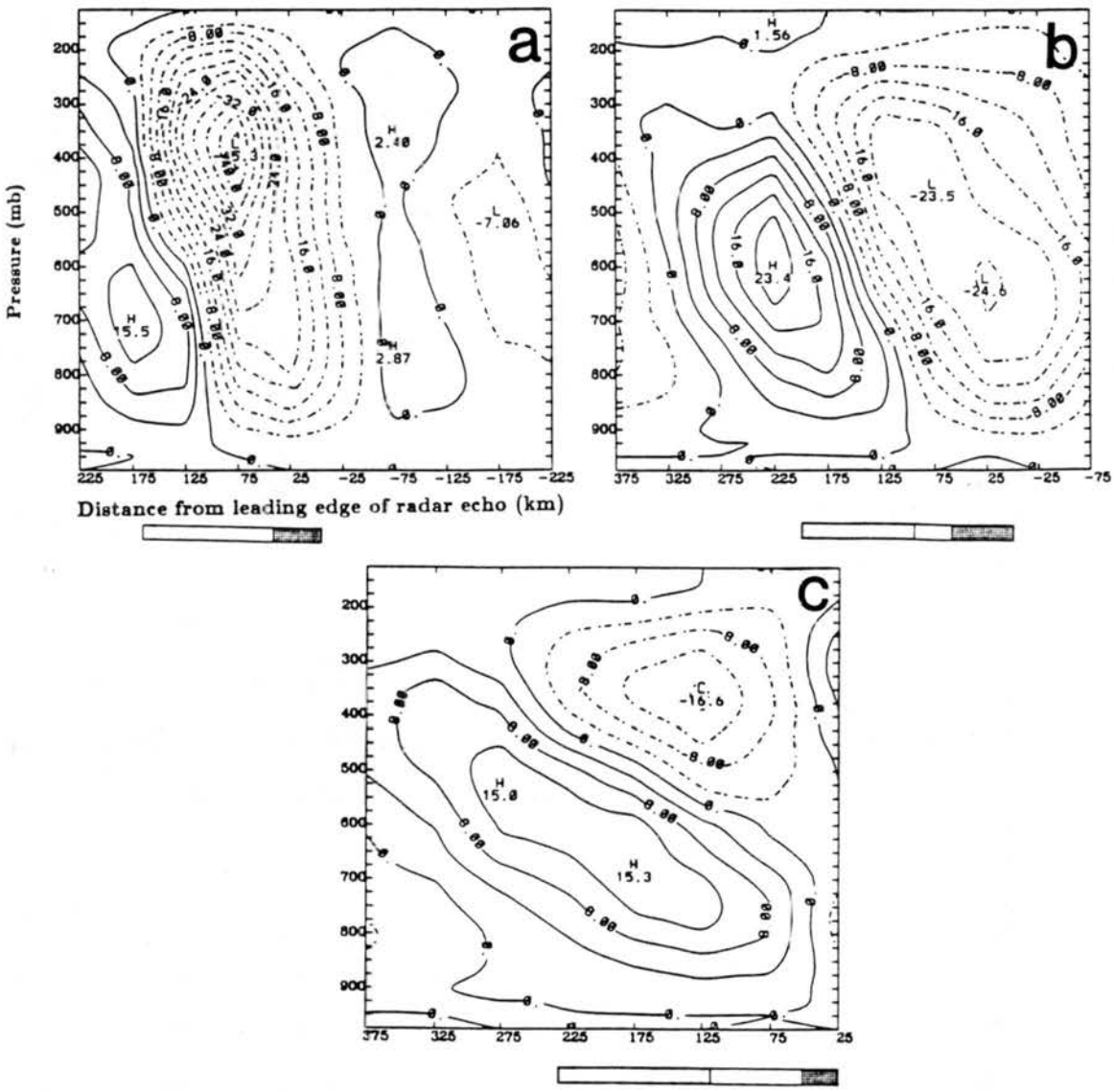

Figure 4.4: As in Fig. 4.2 except for vertical velocity (ω), in units of $\mu b\ s^{-1}$. ($1\ \mu b\ s^{-1} \approx 1\ cm\ s^{-1}$ at 840 mb, $2\ cm\ s^{-1}$ at 360 mb, and $3\ cm\ s^{-1}$ at 210 mb.

Some grid point values of upward motion at 0300 UTC at 400 mb exceeded 1.3 $m\ s^{-1}$. The small values of upward motion at 0730 UTC are due partly to the proximity of the convective line to the edge of the grid. Zhang and Gao (1989) found in a model simulation of this line that the peak updraft speeds were fairly constant from 0200 to 0600 UTC, and then dropped off very rapidly. The locations of the peak velocities were generally lower, around 500 mb, than those found in this study, and the magnitudes were typically twice those found using the rawinsonde data. The fact that the peak updraft speeds are found at higher levels in this study may be evidence of aliasing of the high-level mesoscale ascent within the stratiform anvil into the convective line updraft. Compositing over a three-hour time interval in this study accounts for the earlier time of rapid decrease in upward motion than that found by Zhang and Gao.

The strong mid-level convergence found within the stratiform region helped to drive a mesoscale updraft above it, and downdraft below it. Because of the resolution afforded by rawinsondes, some aliasing of convective motion into the stratiform region occurs in the analyses. In addition, the lack of sounding data above mid-levels at many points within the stratiform region results in smoothing of data from the convective region and post-squall region into the stratiform region. Only one profiler site was positioned well within the stratiform region, and the addition of that data appeared to cause more problems with noise (due to its close proximity to other data points) than it alleviated by reducing aliasing. These factors result in the appearance of just two main regions of differing vertical velocity (especially at 0600 and 0730 UTC) in the figures: a large area of upward motion toward the leading edge of the system and a similarly large area of downward motion centered near the back edge of the radar echo. Upward motion can be seen in the trailing anvil above the stratiform region, but a pronounced separate maximum as seen in Ogura and Liou (1980) is not obvious. At 0600 UTC, a hint of enhanced upward motion can be seen near and behind the back edge of radar echo at 300 mb. By 0730 UTC, there appears to be a well-defined peak in upward motion over the stratiform region, but unfortunately the convective line had left the data network, and a direct comparison with Ogura and Liou cannot be made. The upward velocity minimum over the transition zone, detected

with Doppler radar (Smull and Houze, 1987) around 0300 UTC, cannot be seen because its scale (a few tens of kilometers) was smaller than that resolvable with the rawinsondes. It is possible that by 0730 UTC, this upward motion minimum was resolvable, and is depicted at mid-levels near the right edge of Fig. 4.4c.

The area covered by downward motion at low levels in the stratiform region grew with time, although maximum intensity was reached at 0600 UTC when the stratiform region was most intense. At this time, the peak descent was over 23 $\mu b\ s^{-1}$ (30 $cm\ s^{-1}$). This is substantially lower than the peak descent of 40 $\mu b\ s^{-1}$ found in Ogura and Liou (1980), but can be explained by the fact that the station spacing used in their study was roughly half of that used for this case. The mesoscale downdraft indicates both mid-level convergence in the stratiform region, and the cooling of low-level air by melting of snow and evaporation of falling rain (Leary and Houze, 1979). Because the mid-level convergence was not weakening noticeably between 0600 and 0730 UTC, a decrease in the rain rates and cooling was probably responsible for the weakening of the subsidence. [1] The level of maximum downward motion rose with time, and was near or just above the melting level at 0600 and 0730 UTC. Rutledge *et al.* (1988) also found that the level of peak downward motion rose with time, occurring near the melting level early and rising somewhat above it at later times. In some other squall lines (e.g. Ogura and Liou, 1980; Smull and Houze, 1987), the peak descent was found below the melting level, closer to 700 or 800 mb. The location of maximum downdraft intensity was very near the back edge of radar echo, supporting the analyses of Johnson and Hamilton (1988).

As was the case with the convergence axis, the slope of the axes of maximum positive and negative vertical motion also changed dramatically over time. At 0300 UTC, the system appeared to be nearly vertical, with the peak updraft at high levels within 75 km of the leading edge of the system. By 0730 UTC, the peak updraft had shifted to 125 km behind the leading edge. The axis of peak downward motion shows the increasing

---

[1] It will be shown later that stratiform rainfall rates were decreasing quickly at this late stage in the squall line lifetime.

slope most dramatically. These results agree with radar and satellite observations showing that the system was spreading out, with the convective line separating from the trailing stratiform cloud. The increasing slant of the system is not necessarily an indication of an increasing tilt of the convective line elements as discussed in Rotunno *et al.* (1988).

Some squall lines have been shown to produce regions of compensating descent just ahead of their leading edges (Fankhauser, 1974; Fritsch, 1975; Sanders and Paine, 1975; Gamache and Houze, 1982). At 0300 UTC, a weak region of downward motion did exist throughout the depth of the troposphere just ahead of the squall line. Its average magnitude never exceeded a few $\mu b\ s^{-1}$, although at certain points ahead of the system, grid values exceeded 10 $\mu b\ s^{-1}$. Sanders and Emanuel (1977) conclude that this feature is characteristic of the "early mature" stage of large convective systems. The lack of a forward anvil with this case suggests that the Hoxit *et al.* (1976) mechanism for this downward motion is unlikely. This downward motion does not show up at later times as the system approaches the edge of the data network. Because the squall line was exiting the region, it is not known whether the descent ceases as the system decays, or if subsidence continues throughout its demise. The area of weak upward motion at 0300 UTC ahead of the pre-squall descent was associated with earlier convection that was now decaying.

Figure 4.5 shows vertical profiles of omega taken in the stratiform and convective line portions of the system at different times as it weakened. Grid values over the entire area defined as stratiform and convective line echo were averaged. These profiles are similar to those determined by Gamache and Houze (1982) for a tropical squall line. By referring to Fig. 4.4, it can be seen that vertical profiles would vary substantially depending upon the section of the stratiform region in which they were taken. As would be expected with a resolution on the order of 50 km, magnitudes within the convective line region are at least an order of magnitude less than the observed values associated with convective updrafts. Since motion within the stratiform region is more on the mesoscale, these values should be closer to the real velocities. As the upward motion at high levels in the stratiform region weakened over time, the downward motion averaged over the entire area strengthened, and the level of maximum descent rose, reaching 700 mb at 0730 UTC. This level, averaged

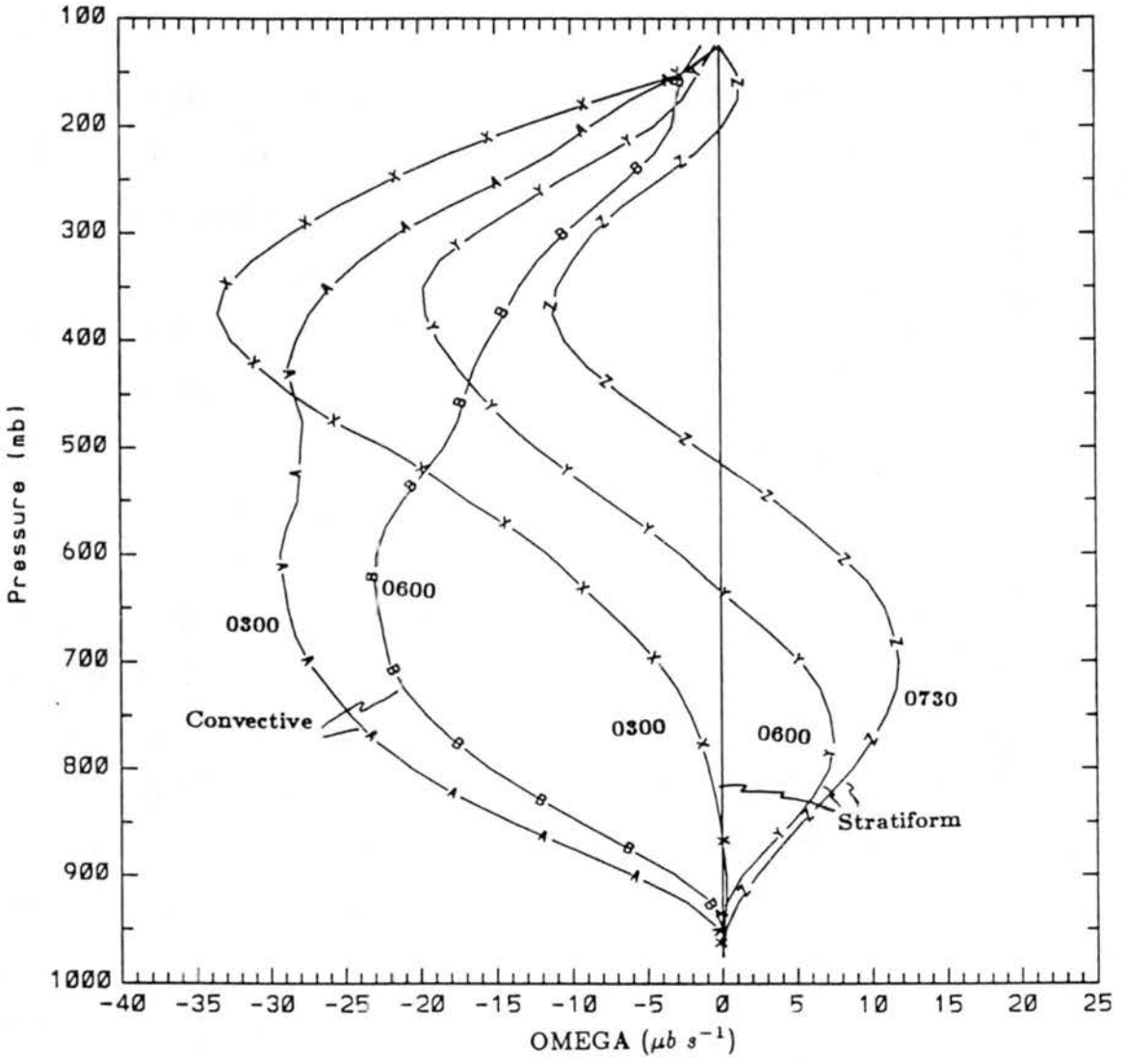

Figure 4.5: Vertical profiles of omega averaged over the convective and stratiform portions of the squall line at different times. Line A taken in the convective region at 0300 UTC, B in the convective region at 0600 UTC, X in the stratiform region at 0300 UTC, Y in the stratiform region at 0600 UTC, and Z in the stratiform region at 0730 UTC. See Fig. 4.4 for conversion from $\mu b\ s^{-1}$ to $cm\ s^{-1}$.

over the stratiform region, is lower than that of the peak downward motion seen in the vertical cross-sections (Fig. 4.4). This is a result of averaging over the large stratiform region where the level of maximum descent lowers toward the convective line.

Also, at the later time, descent is apparent near the tropopause. This result has occasionally been found in other studies (Johnson and Young, 1983; Balsley, *et al.* 1988; Menard and Fritsch, 1989). It may simply be a result of the adjustment made to omega. However, vertical velocities calculated from the dry static energy in Eq.(2.16) also show weak downward motion at 0730 UTC and 0600 UTC, especially when radiative cooling is taken into account. (See Fig. 4.6). As another check, vertical velocity was calculated using the kinematic method integrating from 100 mb downward, instead of upward from the surface. Because of convergence at the highest levels with divergence beneath at the rear edge of the radar echo, this method also showed subsidence of a few $cm\ s^{-1}$ near the tropopause. Because of the stability of the lower stratosphere, weak descent like this extending above the tropopause should result in substantial heating.

Figures 4.7 and 4.8 illustrate some of the three-dimensionality within the vertical velocity field at approximately the level of maximum subsidence in the stratiform region (700 mb; Fig. 4.7) and the level of maximum upward motion within the system (400 mb; Fig. 4.8). Although the strong upward motion toward the front of the system and the subsidence behind it lied in two prominent bands at 700 mb, the bands did show some structure. The two downward motion centers to the rear of the line maintained their identity throughout the time period of study, and are consistent with the arguments presented in Johnson and Hamilton (1988) linking the two wake lows in this squall line to two suggested enhanced regions of subsidence at the back edge of the trailing stratiform region. These two features were also associated with two stratiform rainfall maxima (see Fig. 5.20). The southern downward motion maximum was associated with the strongest rear-to-front flow. The northern maximum, however, was in a region of relatively weak rear-to-front flow at this level (700 mb). This may be due to the presence of a mesolow at mid-levels just to the south of this location (as will be shown in Chapter 6). The pressure gradient caused by this low would oppose rear-to-front flow in the vicinity of the northern

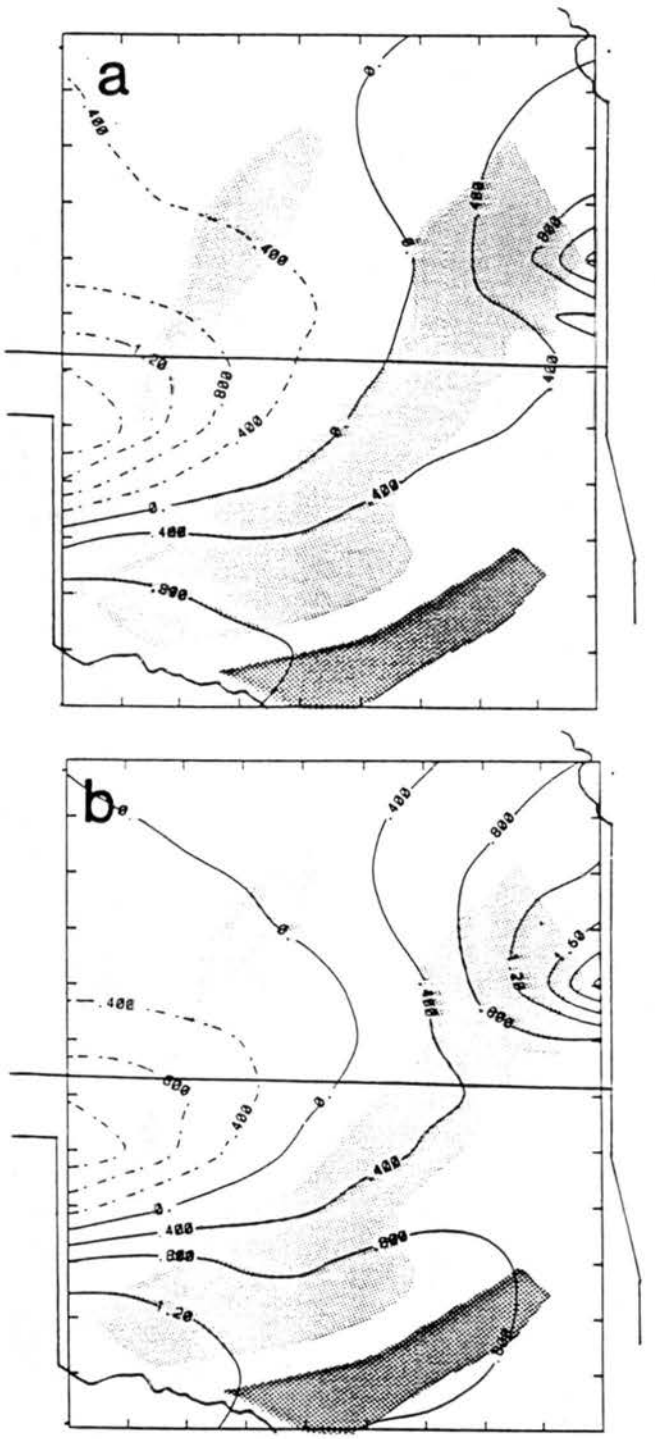

Figure 4.6: Vertical velocity (omega) at 125 mb calculated from dry static energy data, assuming a.) no radiative cooling and b.) radiative cooling of 0.5 $^{o}Chr^{-1}$. Values in $\mu b\ s^{-1}$, with 1 $\mu b\ s^{-1} \approx 5\ cm\ s^{-1}$. Composited 0730 UTC radar echo is shown by shading with darkest shading representing convective line, large area of light shading the stratiform region, and small area of light shading behind the main system showing region of light scattered showers.

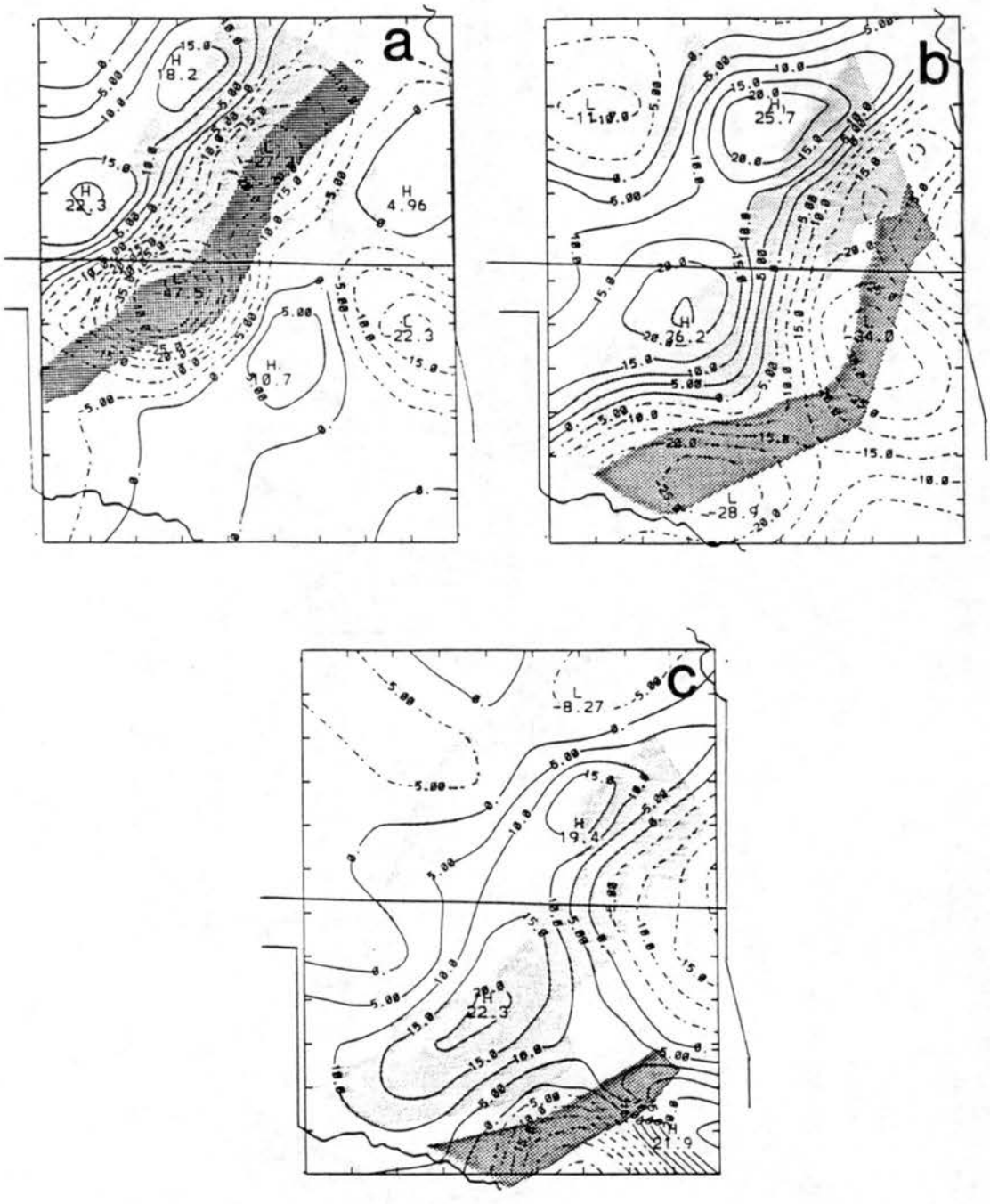

Figure 4.7: Vertical velocity (omega) at 700 mb in the PRE-STORM region for a.) 0300 UTC, b.) 0600 UTC and c.) 0730 UTC. Values in $\mu b\ s^{-1}$, with $1\ \mu b\ s^{-1} \approx 1.2\ cm\ s^{-1}$. Composited radar echoes are shown by shading. Darkest shading is the convective line region, large area of light shading the stratiform region, and small areas of light shading ahead of the line at 0300 UTC, and behind it at 0600 and 0730 UTC regions of scattered light showers.

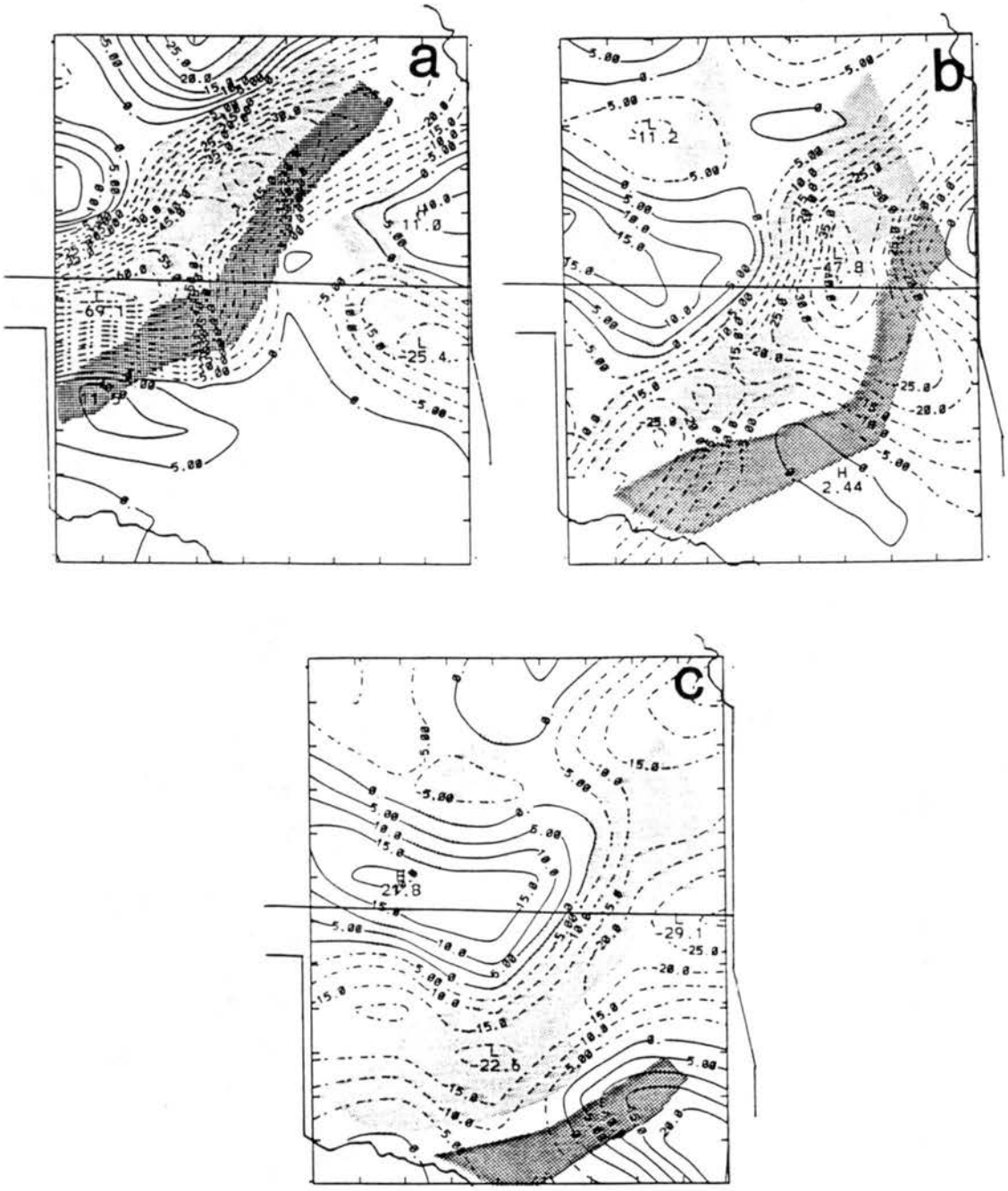

Figure 4.8: As in Fig. 4.7, except at 400 mb. 1 $\mu b\ s^{-1} \approx 1.8\ cm\ s^{-1}$.

subsidence maximum, possibly accounting for the lack of a corresponding enhancement of the rear-inflow jet there, as was found with the southern downward motion maximum. At 400 mb (Fig. 4.8), the band of upward motion was still evident, but the downward motion no longer occupied a line-parallel band, but rather a band perpendicular to the squall line.

Pre-squall descent can be seen only at 0300 UTC at low levels (Fig. 4.7), but this subsidence can be seen in small regions at all times at 400 mb (Fig. 4.8). Upward motion associated with weak or weakening echoes can be seen ahead of the squall line at 0300 UTC, and behind the mesoscale downdraft at 0600 and 0730 UTC. The ascent at 700 mb (Fig. 4.7) behind the downdraft is believed to be due to low-level convergence occurring as surface winds blow through the wake low and meet the ambient flow. On this day, the strong subsidence within the rear-inflow jet appeared to dry out the environment, restricting new convective growth. However, more intense convective development has been observed in this region of convergence behind other MCSs by Menard *et al.* (1988), and Stumpf and Gallus (1989).

The axis of strong downward motion at high levels (Fig. 4.8) extended from behind the squall line into a"notch" in the radar echo at the back edge of the stratiform region. This downward motion can be seen as early as 0300 UTC, but becomes more well-defined at later times. The band was roughly 100 km wide and descent at 400 mb reached 22 $\mu b\ s^{-1}$ (40 $cm\ s^{-1}$) at 0730 UTC. This band was also aligned toward the direction in which the leading edge of convection had "bowed". Smull and Houze (1985) found in another midlatitude squall line that the notch and bowing were aligned in the zone of maximum rear inflow at mid-levels. Relative wind data from the rawinsondes for this case showed that the notch and bowing in the radar echo were close to the axis of strongest rear inflow, with errors in the data, or smoothing in the analysis causing some differences in location of 50 to 100 km. It appears that this current of sinking air coming into the anvil from the post-squall environment was somehow associated with the evaporation of cloud droplets and the resulting notch in the radar echo. The bowing of the echo has been attributed to the development of new convection ahead of the system as low-level

convergence is enhanced when the rear-inflow jet reaches the leading edge of convection (Zhang and Gao, 1989).

4.4 Temperature structure

The temperature field associated with this squall line demonstrates the important role that heating from condensation and cooling from evaporation play, along with adiabatic warming and cooling, in altering the synoptic-scale pattern. Figures 4.9-4.11 show the temperature fields at all 3 times at low levels (Fig. 4.9), middle levels (Fig. 4.10) and high levels (Fig. 4.11). At low levels (850 mb), the lowest temperatures, with readings as low as 287 K, were found within the front side of the stratiform rain region, where evaporation of the rain within the mesoscale downdraft was causing cooling. These temperatures were generally over 5 K cooler than those ahead of the convection. At 0300 UTC, a band just ahead of the convective line had the warmest temperatures in the region. This was the same area experiencing weak descent through the depth of the troposphere. Also at low levels, some enhanced warming appeared just behind the back edge of radar echo, particularly at 0600 and 0730 UTC. Both of these warm anomalies were also found in a GATE squall line by Johnson and Nicholls (1983). The region near the back edge of the radar echo would be experiencing strong subsidence with its accompanying adiabatic warming, with less of the offsetting cooling caused by evaporation which occurs within the stratiform rain region. This was the area occupied by a wake low in the surface pressure field. (See Johnson and Hamilton, 1988). At all three times, the warmest temperature anomaly was in the vicinity of the lowest pressure within the wake low (see Fig. 13 of Johnson and Hamilton; 1988). The positive temperature anomaly was associated with the northern maximum in downward motion shown earlier in Fig. 4.7. The southern subsidence maximum did not show up as a positive temperature anomaly, possibly because that strong descent was occurring more within the stratiform rain region. As will be seen later in Figs. 5.5 and 5.6, evaporative cooling was stronger at low levels in the southern part of the stratiform region than in northern areas.

At mid-levels (500 mb), the heating from condensation within the squall line is apparent. At all times, a weak temperature maximum is found within the system, near

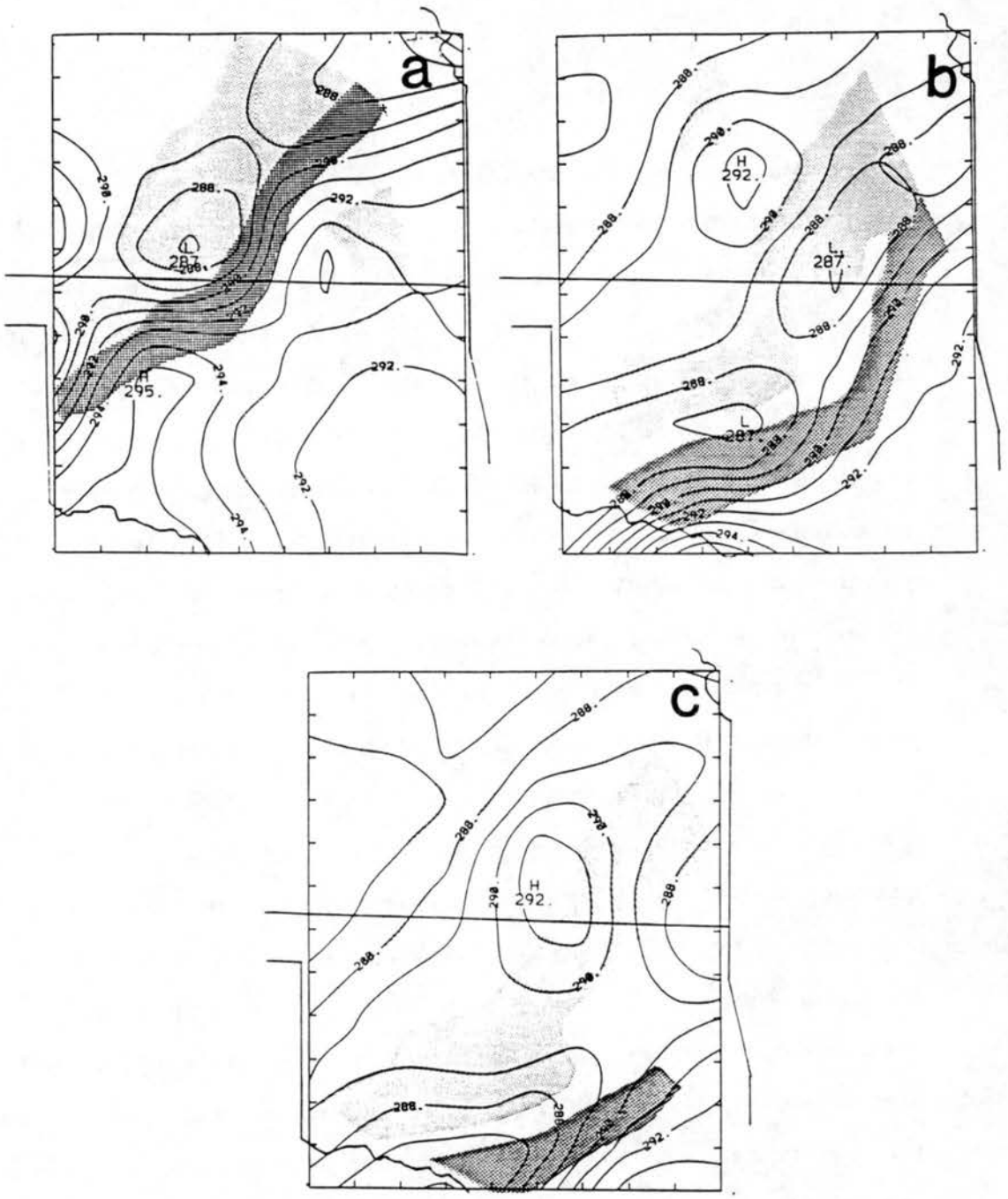

Figure 4.9: Fig. 4.9 Temperature (in K) across the PRE-STORM region at 850 mb for a.) 0300 UTC, b.) 0600 UTC and c.) 0730 UTC.

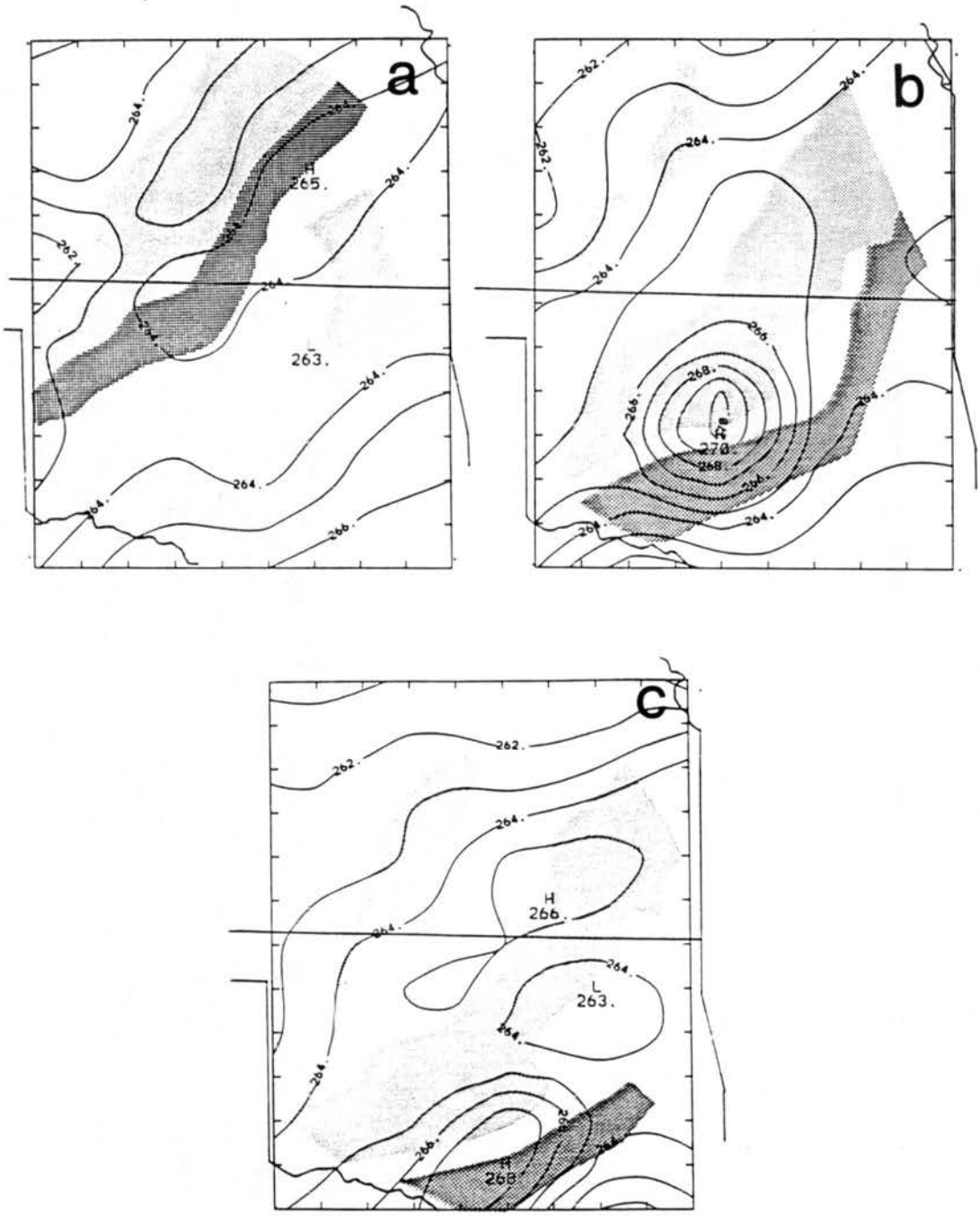

Figure 4.10: Same as Fig. 4.9, except for 500 mb.

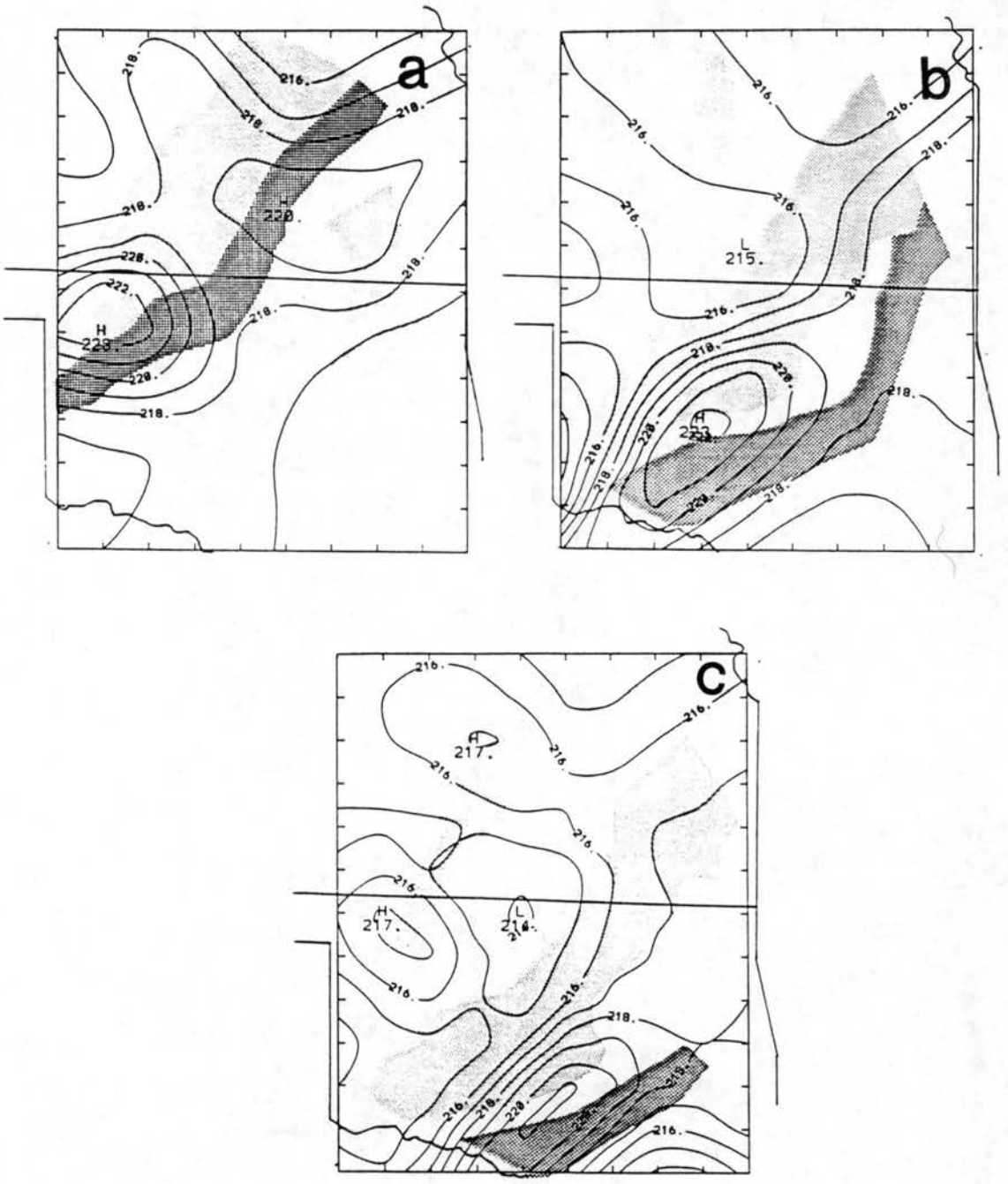

Figure 4.11: Same as Fig. 4.9, except for 200 mb.

the convective line region. At 0600 UTC, a concentrated area with temperatures over 5 K warmer than the surroundings can be found in the southern part of the system. It is possible that one of the balloons ascended in an updraft, resulting in abnormally high temperatures at mid and high levels (Davies-Jones, 1974; Smull and Houze, 1987; Bluestein, 1988). By 0730 UTC, when the system was almost entirely separated into two sections, two temperature maxima can be seen, one toward the back of the stratiform region, and the other near the remaining convective line. The more intense anomaly may be due in part to the ascent of one balloon in an updraft, while the weaker anomaly is the one above the surface wake low, caused by subsidence warming that is not opposed by evaporative cooling.

Finally, at high levels (200 mb), the warming within the squall line is most pronounced. At all three times, there was at least one area with temperatures greater than 4K higher than the "undisturbed" environment ahead of the system. Warm anomalies within high-level anticyclonic circulations have been found in other MCSs by Maddox *et al.* (1981) and Menard and Fritsch (1989). Wetzel *et al.* (1983) have found a mean temperature excess of 3K in the 500-250 mb layer within another midlatitude MCS. Some general cooling possibly due to radiational losses appears to have occurred by 0730 UTC, as the peak temperature in the network has dropped from 223 to 221K, and the coolest temperature found anywhere has also dropped from 215 to 214K. Within the temperature field at 200 mb, a region of low temperature can be found behind the radar echo, in the same location as a band of strong 400 mb descent. Descent was also occurring at this level, 200 mb, although intensities were weaker (figure not shown). Descent would normally be expected to result in a warm anomaly; however, the lapse rates at this level were nearly dry adiabatic. At higher levels, the position of the tropopause would be important in determining the temperature patterns. Because the tropopause was elevated over this system, temperatures tended to be lower over the system than in this post-squall environment. This agrees with the results of Maddox *et al.* (1981). It appears from the 0300 UTC data (not shown) that the air behind the squall line near the tropopause level was originally colder than elsewhere, and it began sinking. The existence of a high-level region

of cool air and the resulting influence on this squall line was also discussed by Zhang and Gao (1989). They simulated the squall line using a three-dimensional mesoscale nested-grid model, and found that the rear-inflow jet began to descend at roughly 0000 UTC as a consequence of a deep cooling that occurred from 550 mb to the tropopause near the rear of the system. At the later stages of the system, the strongest subsidence was still associated with low temperatures.

Chapter 5

MESOSCALE HEAT AND MOISTURE BUDGETS

The purpose of this chapter is to present results of the heat and moisture budgets for the mature to decaying stages of the June 10-11 squall line. In this budget study, the apparent heat source, Q_1 , and the apparent moisture sink, Q_2 , were calculated at each grid point using gridded wind, moisture, and dry static energy data along with the values of ω calculated from the kinematic method. Averages over regions were then calculated from the gridded values of Q_1 and Q_2 . This differs from many budget studies (e.g. Nitta, 1972; McNab and Betts, 1976) which are performed using an integration over a closed region encircled by a few rawinsondes. This chapter will show differences in the heating and moistening profiles between the convective line and stratiform precipitation regions of the system, document the evolution of the budgets as the system decayed, make comparisons with other midlatitude and tropical heat and moisture budgets, and compare budget-integrated predictions of rainfall rates with those observed.

5.1 Spatial and temporal variations of the heat budget

From Eq. (2.5) it can be seen that the apparent heat source, Q_1 , at a grid point, calculated by taking the total derivative of the dry static energy, is a function of the radiative heating rate, the release or loss of latent heat due to condensation or evaporation, and the vertical eddy heat flux. Because the rawinsonde data for this study were taken from composited stations only 80 km apart, the resolution allows magnitudes of the latent heating term that are large compared with other budget studies done over larger temporal and spatial scales. These rates from condensation and evaporation are typically several $^oC\ h^{-1}$, much larger than the radiative cooling rates which are generally a fraction of $1^oC\ h^{-1}$. Therefore, Q_1 , except perhaps at the highest levels of the stratiform cloud, is

primarily a measure of the amount of latent heating or cooling, and the convergence of eddy sensible heat transport taking place at a point.

Figure 5.1 illustrates with vertical cross-sections the evolution of the Q_1 field at 0300, 0600 and 0730 UTC. The most noticeable feature is the weakening of the apparent heat source from 0300 UTC through 0730 UTC. Heating rates of over $13°C\ h^{-1}$ decreased to less than $8°C\ h^{-1}$ by 0600 UTC, and to $5°C\ h^{-1}$ by 0730 UTC. This corresponds well with the weakening of the system and the decrease in low-level radar reflectivities (see Fig. 4.1). The maximum heat source was consistently at high levels (around 400 mb), and located 75 km behind the leading edge of the system at 0300 and 0600 UTC, and 125 km behind it at 0730 UTC. Cooling due to evaporation, and to a lesser extent melting, can be seen to the rear of the system with peak intensity of over $6°C\ h^{-1}$ at 0600 UTC when the mesoscale downdraft was most intense. The maximum cooling was found around 550 mb within 50 km of the rear edge of radar echo. The cooling extended throughout the depth of the troposphere. Leary and Houze (1979) found in a study of five GATE convective systems that cooling due to melting of ice within a 1 km melting layer was similar in magnitude to cooling from evaporation of raindrops below the melting layer. Both processes could produce cooling rates from less than 1 $°C\ h^{-1}$ to over 6 $°C\ h^{-1}$. Additional weak warming found ahead of the system at 0300 UTC and behind it at 0600 and 0730 UTC is associated with condensation taking place in weak showers. Weak cooling at high levels to the rear of the systems may be an indication of cloud top radiative cooling (Webster and Stephens, 1980).

Vertical profiles of Q_1 averaged over the convective line and stratiform precipitation regions at different times can be seen in Fig. 5.2. The weak cooling below 850 mb in the convective line regions was due to evaporation within the heavy rainfall below cloud base. Convective heating can be found in this region above 850 mb, and it was a maximum around 400 or 450 mb. The values of heating in this portion of the system are underestimated because the rawinsondes cannot resolve the true intensity of the convective updrafts. Evidence of this underestimation will be discussed later, and shown in Fig. 5.4b.

The cooling associated with the mesoscale downdraft in the stratiform region occupied a deeper layer as the system decayed (Fig. 5.2), and by 0730 UTC, cooling was occurring

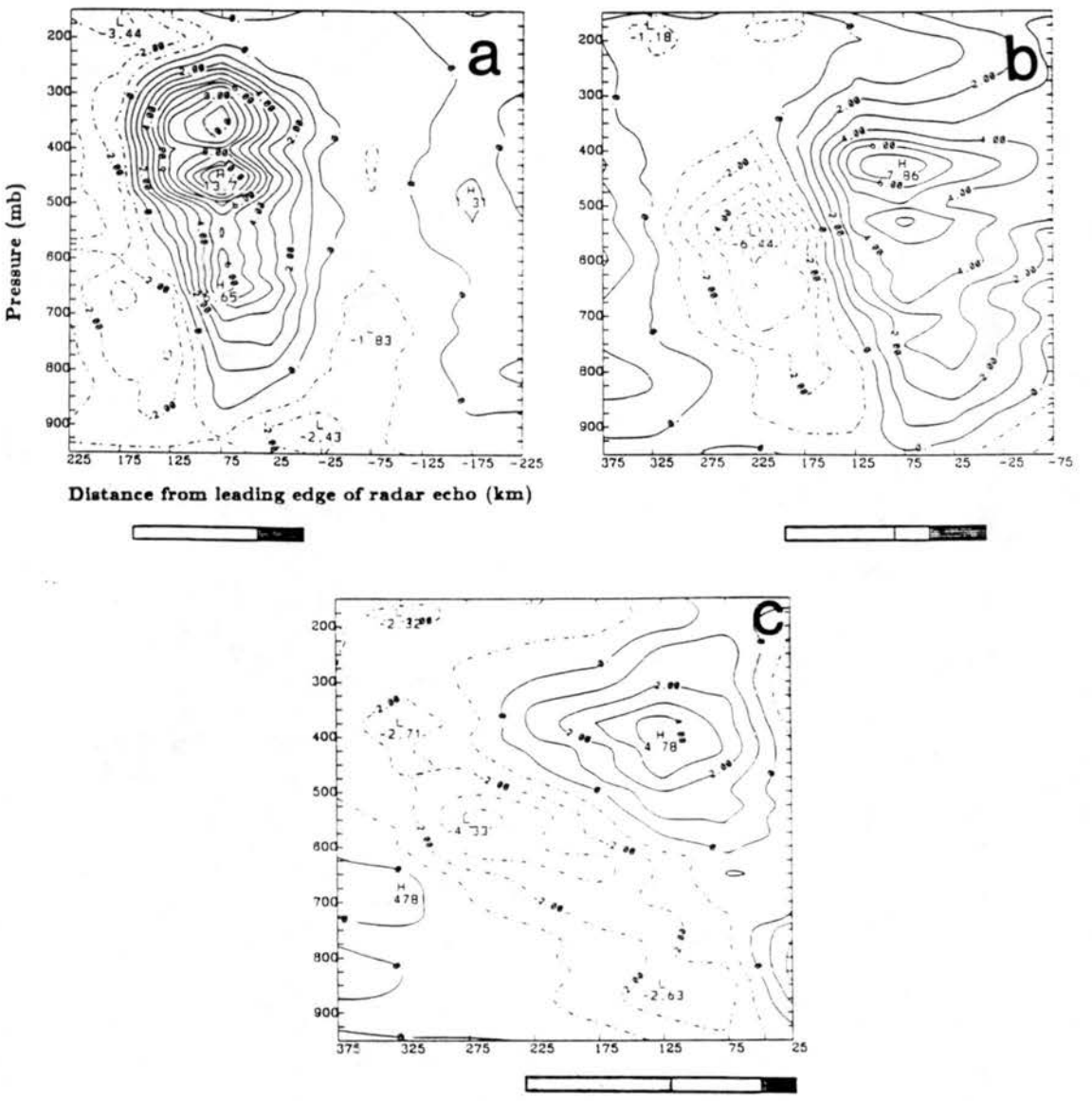

Figure 5.1: Apparent heat source Q_1 (in $^oC\ h^{-1}$) at a.) 0300 UTC, b.) 0600 UTC, and c.) 0730 UTC.

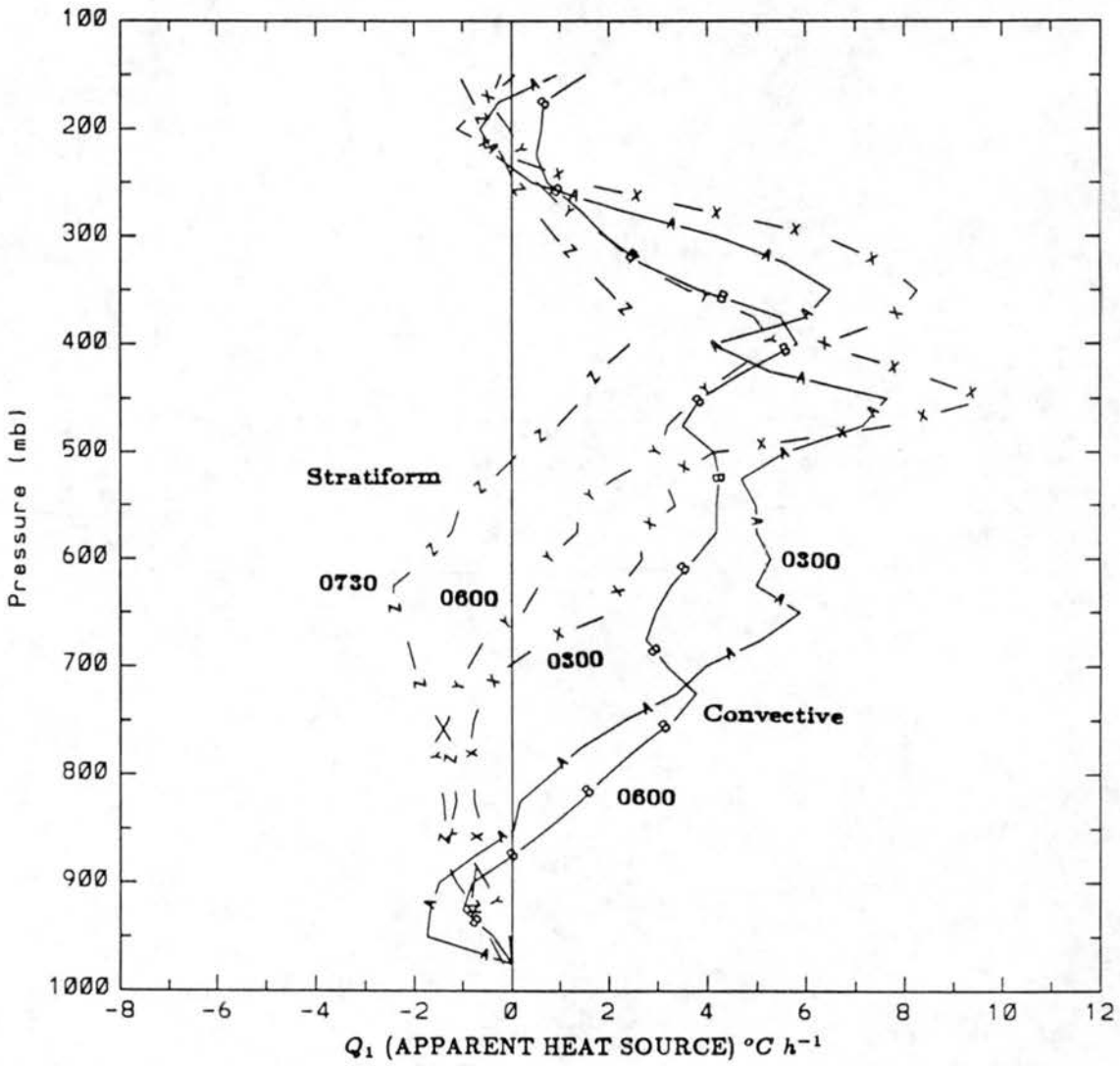

Figure 5.2: Vertical profiles of Q_1 averaged over the convective and stratiform rain regions of the squall line at different times. Solid lines represent the convective line region and dashed lines the stratiform region. Line A taken in the convective region at 0300 UTC, B in the convective region at 0600 UTC, X, Y and Z in the stratiform regions at 0300, 0600 and 0730 UTC.

from the surface to almost 500 mb. The level of maximum heating within the mesoscale updraft increased slightly from 450 mb at 0300 UTC (the lower of two peaks at high levels at this time) to around 400 mb at 0600 UTC and 0730 UTC. The magnitudes of heating within this updraft were similar to those at high levels within the convective line region of the system. The increasing height of the heating peak could also be found in the convective line from 0300 to 0600 UTC (the convective line region at 0730 UTC was at the eastern edge of the grid, and therefore data cannot be shown). The similarity of the Q_1 curves between the convective line and stratiform regions at high levels is evidence of the aliasing taking place at these heights above the levels where many rawinsondes terminated.

Comparisons between the system-average (convective line region, transition zone and stratiform precipitation area) vertical profiles of Q_1 for this case, and several other mid-latitude studies can be seen in Fig. 5.3. Figure 5.3a shows vertical profiles of Q_1 averaged over the entire June 10-11 system at 0300 and 0600 UTC. Houze (1982) and Johnson (1984) found that the heating profile of an entire mesoscale convective system is a combination of the profiles due to two distinctly different circulation features: the stratiform region with a heating peak at 400 mb and a cooling peak near 700 mb, and the cumulus clouds with a heating peak at mid-levels (600 mb). Because of aliasing of data, the heating peak in the stratiform region and convective line region in this case were at roughly the same level, 450 mb at 0300 UTC, and 400 mb at 0600 UTC (Fig.5.2). This lies near the stratiform region peak found by Johnson. Because of the higher tropopause in the tropics, the heating peak associated with the mesoscale anvil in some tropical systems could be at higher levels than the peak in midlatitude cases. Because the stratiform region covered a larger area than the narrow convective line in this case, it is understandable that the stratiform region high-level heating peak would dominate the system average after aliasing. The stratiform region cooling peak for this case (as seen in Fig. 5.2) was somewhat lower than Johnson's at 0300 and 0600 UTC, around 800 mb. It did rise to 650 mb at 0730 UTC.

Closer to the surface, evaporation in all areas of the system produced cooling (Fig. 5.3a), a result found in other severe storms by Ninomiya (1971) and Lewis (1975) (Fig.

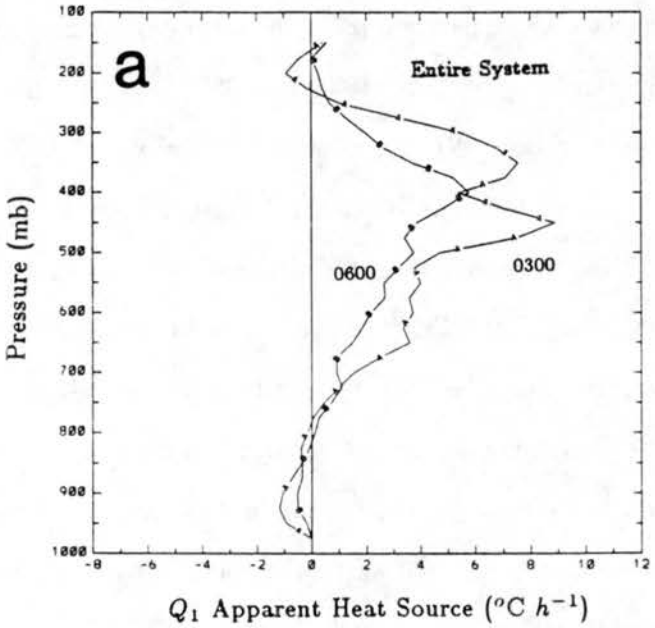

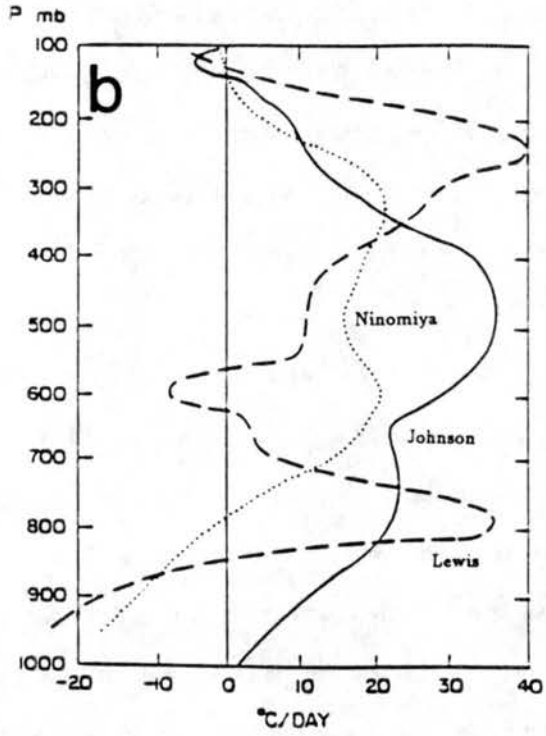

Figure 5.3: Comparison of system-averaged vertical Q_1 profiles for a.) June 10-11 case, and b.) several other midlatitude cases. In a.) curve A taken at 0300 UTC, and B at 0600 UTC. In b.) Curves are taken from Kuo and Anthes (1984) for cases by Johnson (1976, solid line), Lewis (1975, dashed line) and Ninomiya (1971, dotted line). Note different scales with each figure.

5.3b). Cooling is again evident around 200 mb, or near the top of the anvil at 0300 UTC. This cooling was relatively weak, on the order of $1^{o}C\ h^{-1}$. Because this stage of the squall line was occurring at night (2200, 0100, and 0230 local time), radiational cooling may be responsible in part for this feature. It is also possible that some errors in the vertical velocities at this high level played a role (Kuo and Anthes, 1984), although errors appeared to be small for this case. (In Chapter 4, it was shown that independent methods of calculating the vertical velocity produced values in close agreement with each other near the tropopause).

Fig. 5.3b shows heating profiles for a few other midlatitude convective systems. Cooling at low levels due to evaporation is evident in the curves from Lewis (1975) and Ninomiya (1971), but not in the curve from Johnson (1976). His case occurred in Florida, and low levels were likely moister than in the other cases, so that cooling at low levels would not be as great. Except for Lewis (1975), the curves show a gradual increase to a high-level heating peak. The peak for this case around 400 mb falls in between the other cases, and seems reasonable. The magnitudes with the June 10-11 case are greater, reflecting the smaller area over which Q_1 was averaged in this study. The cooling at 200 mb found at 0300 UTC for this squall line (Fig. 5.3a) is also apparent in the three midlatitude curves (Fig. 5.3b).

Heating rates can be normalized by dividing the rates by the observed precipitation rates within a region. This allows a better comparison of the magnitudes between different cases, since studies with close spacing of data diagnose larger heating rates, but also heavier rain rates than studies using a coarse data network. Normalized rates averaged over the entire system and also the convective line region alone can be found in Fig. 5.4. For the entire system (Fig. 5.4a), the normalized rates on June 10-11 were in close agreement with the other cases, all of which occurred in the tropics, except Johnson (1976), which occurred in Florida. The primary difference was at low levels where cooling on June 10-11 was unique. The mesoscale downdraft and rear-inflow jet were causing large evaporation rates within the June 10-11 system.

Fig. 5.4b compares the normalized heating rates within the convective line portion of this system to rates estimated from different methods. The curves for this case at

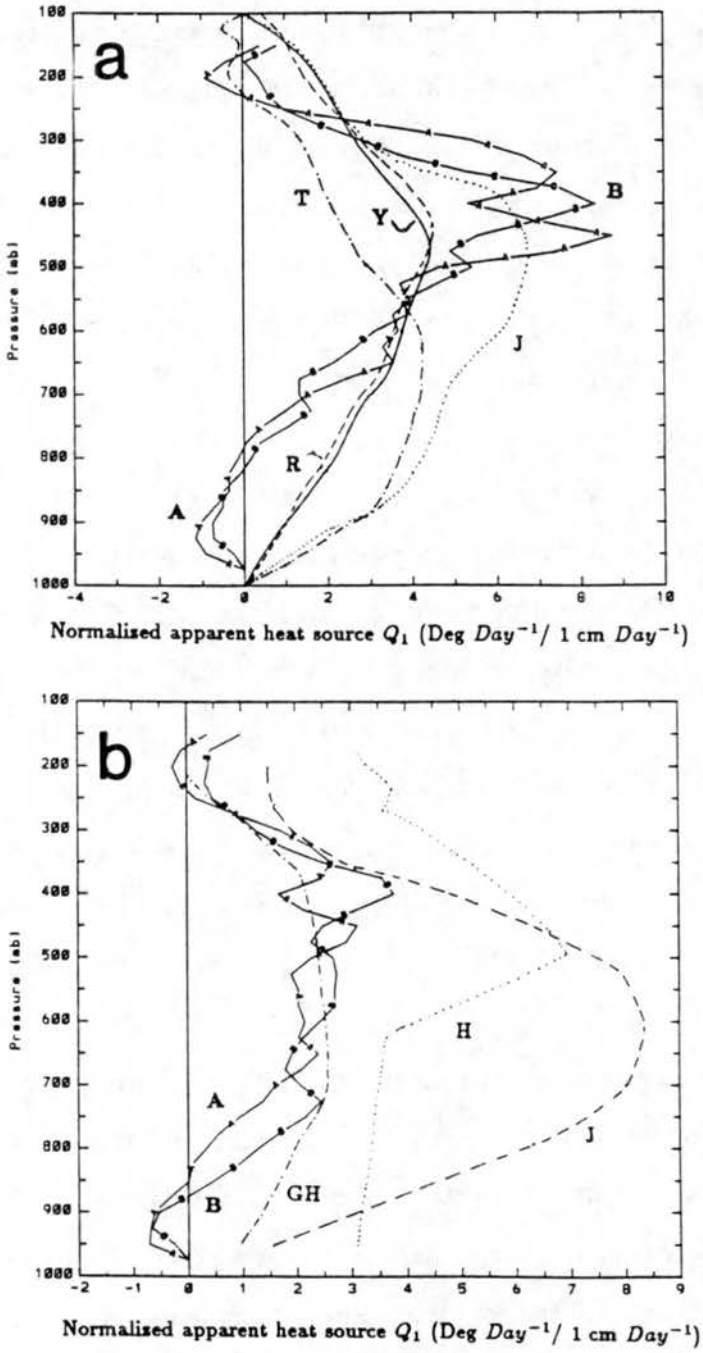

Figure 5.4: Comparison of vertical Q_1 profiles normalized by the rainfall rate for averages taken a.) over the entire system, and b.) over the convective line region. Curves A and B in (a) represent the system averages for the June 10-11 case at 0300 and 0600 UTC, respectively. Other curves (from Johnson, 1984) are from tropical or subtropical cases by Yanai et al. (1973, curve Y), Reed and Recker (1971, curve R), Thompson et al. (1979, curve T), and Johnson (1976, curve J). Curves A and B in (b) represent the convective line averages again for the June 10-11 case at 0300 and 0600 UTC; other curves (after Houze, 1988) include an estimate from a simple cumulus model (Houze, 1982, curve H), a residual inferred from rawinsonde data and stratiform region profiles (Johnson, 1984, curve J), and a computation using diagnosed vertical velocities (Gamache and Houze, 1985, curve GH).

0300 and 0600 UTC, and another observational study by Gamache and Houze (curve GH; 1985) have much weaker heating rates than the curves associated with methods that do not depend so much on rawinsonde data alone. Curve J (from Johnson, 1984) was solved for as a residual after the partitioning of a system into convective line and stratiform regions. Curve H (from Houze, 1982) was estimated from a simple cumulus model. Both of these methods show mid-level peaks in Q_1 , with magnitudes almost double those from observational studies which cannot resolve the large vertical velocities within the convective line adequately. The magnitudes with the June 10-11 case (curves A and B) do agree well with the tropical study of Gamache and Houze (1985). A difference can be found between the level of the peak heating rates for the June 10-11 case and the observational tropical study. Peak rates on June 10-11 were found at higher levels, agreeing with observations of a higher level of peak upward motion in midlatitude convection as compared to tropical convection.

The three-dimensionality of the apparent heat source at different levels within the squall line system can be seen in Figures 5.5 - 5.8. At 850 mb (Fig. 5.5), heating from condensation in the convective line was weak (usually 2 or $3^{o}C\ h^{-1}$). (The over $4^{o}C\ h^{-1}$ rate found in the convective line at 0730 UTC may be unreliable since that portion of the system was at the edge of the data network). Cooling was more widespread than warming at this low level, primarily an indication of extensive evaporation of rainfall. Nighttime radiative effects may have had a small influence, but the Q_1 cooling rates are much larger than what radiative cooling could have caused. Maximum cooling was taking place within the stratiform rain region. Slightly higher up, at 700 mb (Fig. 5.6), more intense heating was occurring near the convective line, especially when the line was strongest at 0300 UTC. Rates in one region were over $10^{o}C\ h^{-1}$. Cooling at this level was also stronger, except at 0730 UTC. The maximum cooling rates, on the order of 4 or $5^{o}C\ h^{-1}$, were located at the back edge of the radar echo, with the absolute peak values near the notch in the echo. This is the region where the downdraft was most intense, and evaporative cooling maximized.

Fig. 5.7 shows the Q_1 field at 500 mb. The maximum heating at this level was displaced toward the rear of the system showing the influence of processes within the

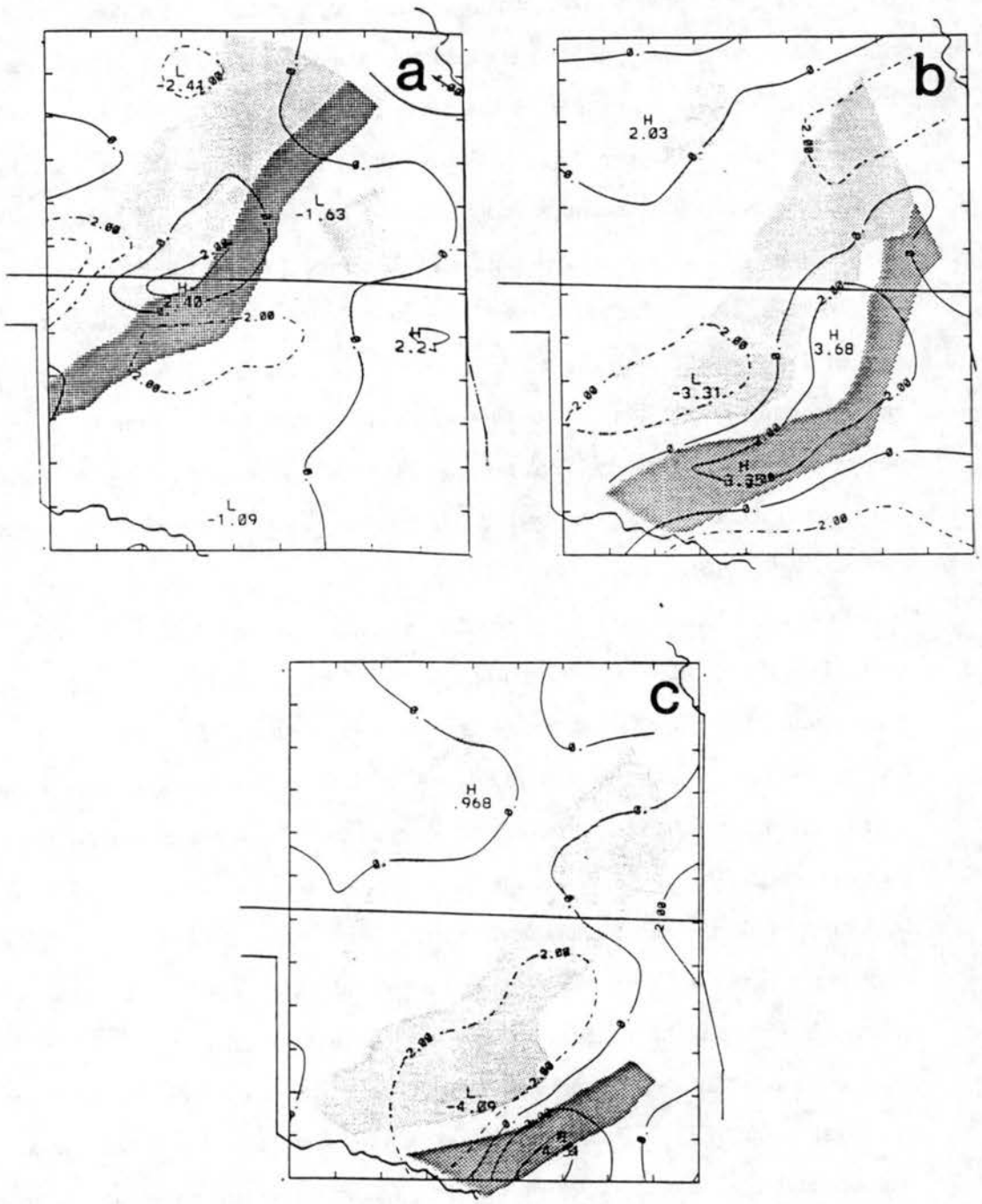

Figure 5.5: Q_1 (in $^oC\ h^{-1}$) at 850 mb in the PRE-STORM region for a.) 0300 UTC, b.) 0600 UTC and c.) 0730 UTC.

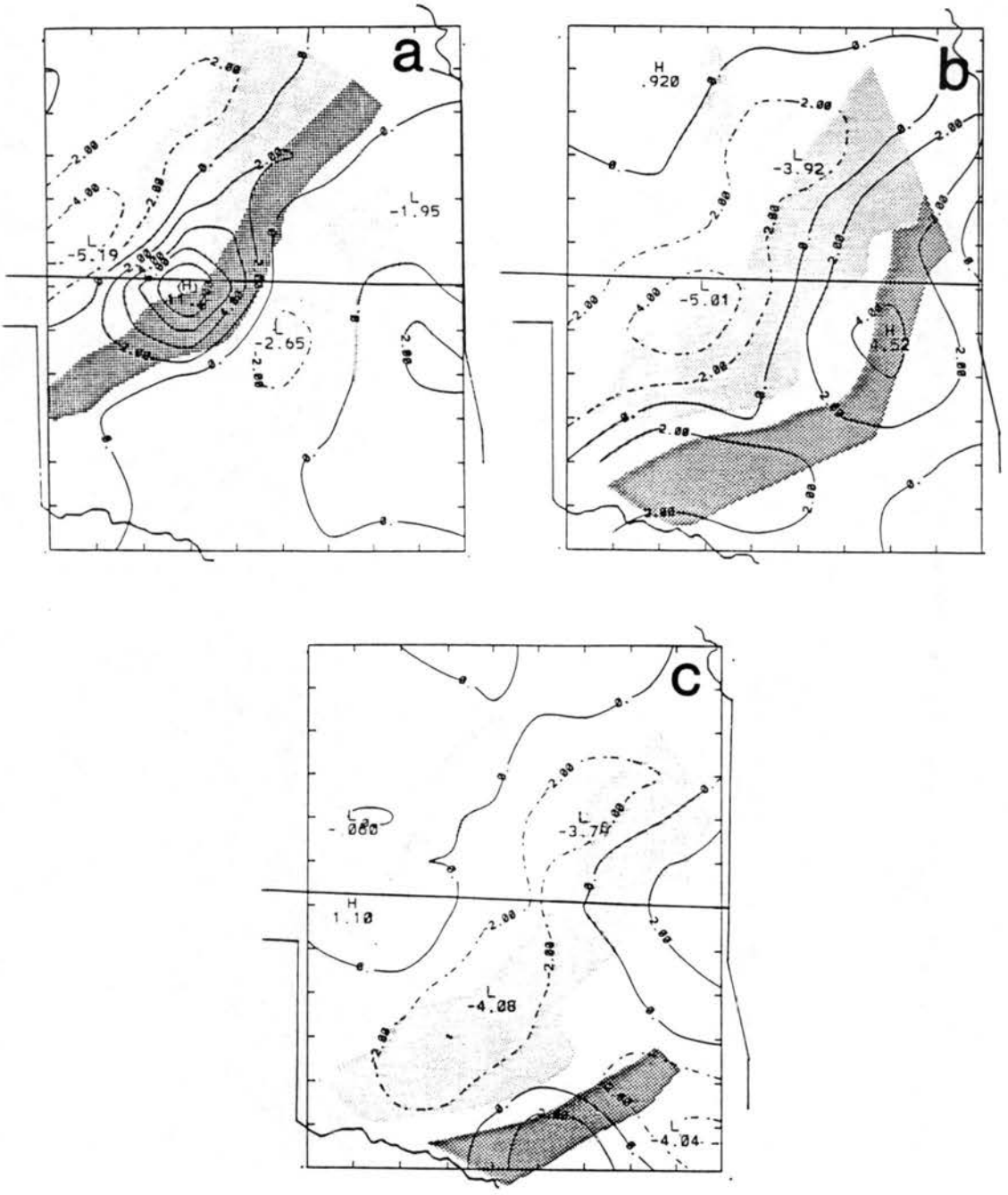

Figure 5.6: Same as Fig. 5.5, except for 700 mb.

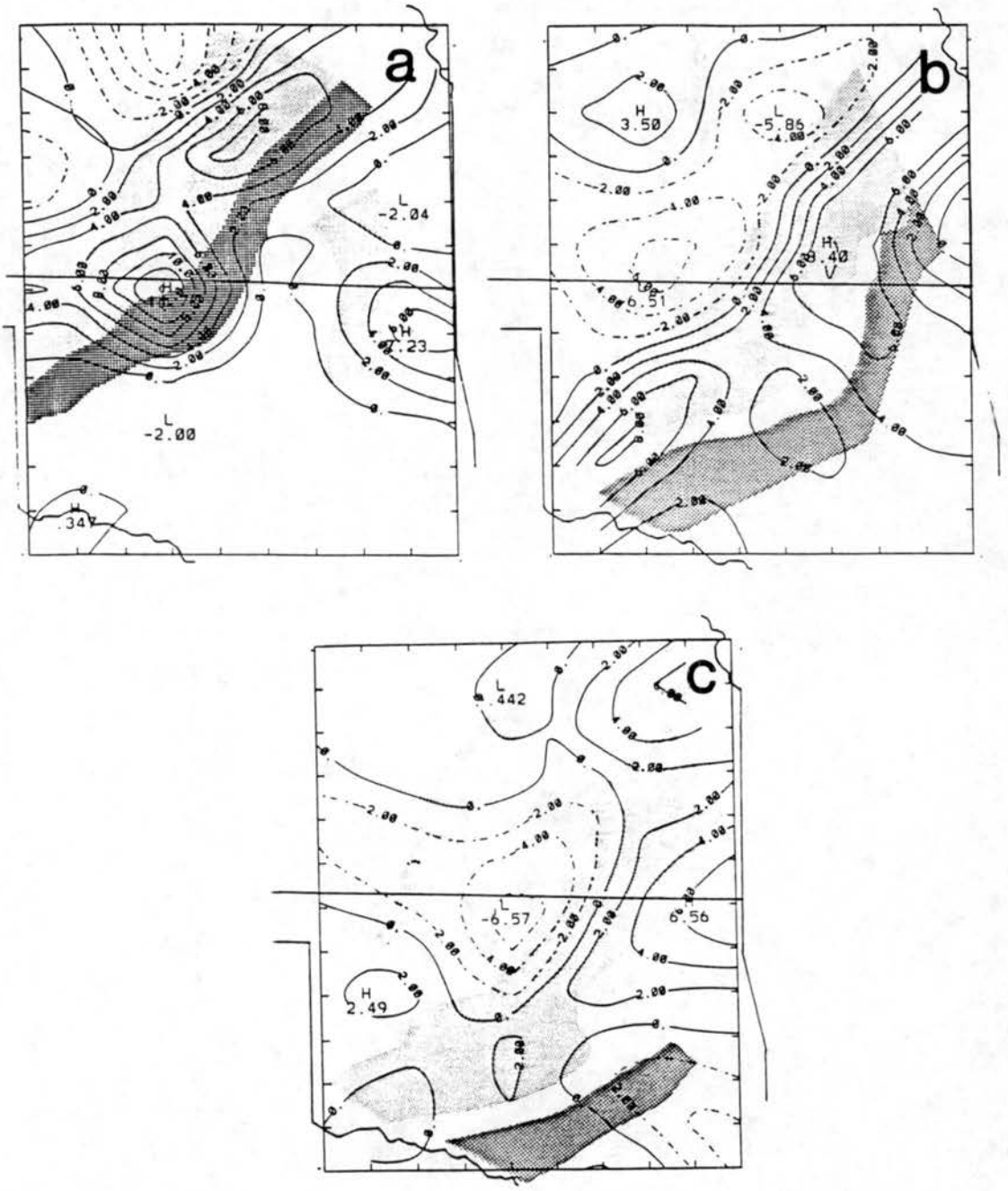

Figure 5.7: Same as Fig. 5.5, except for 500 mb.

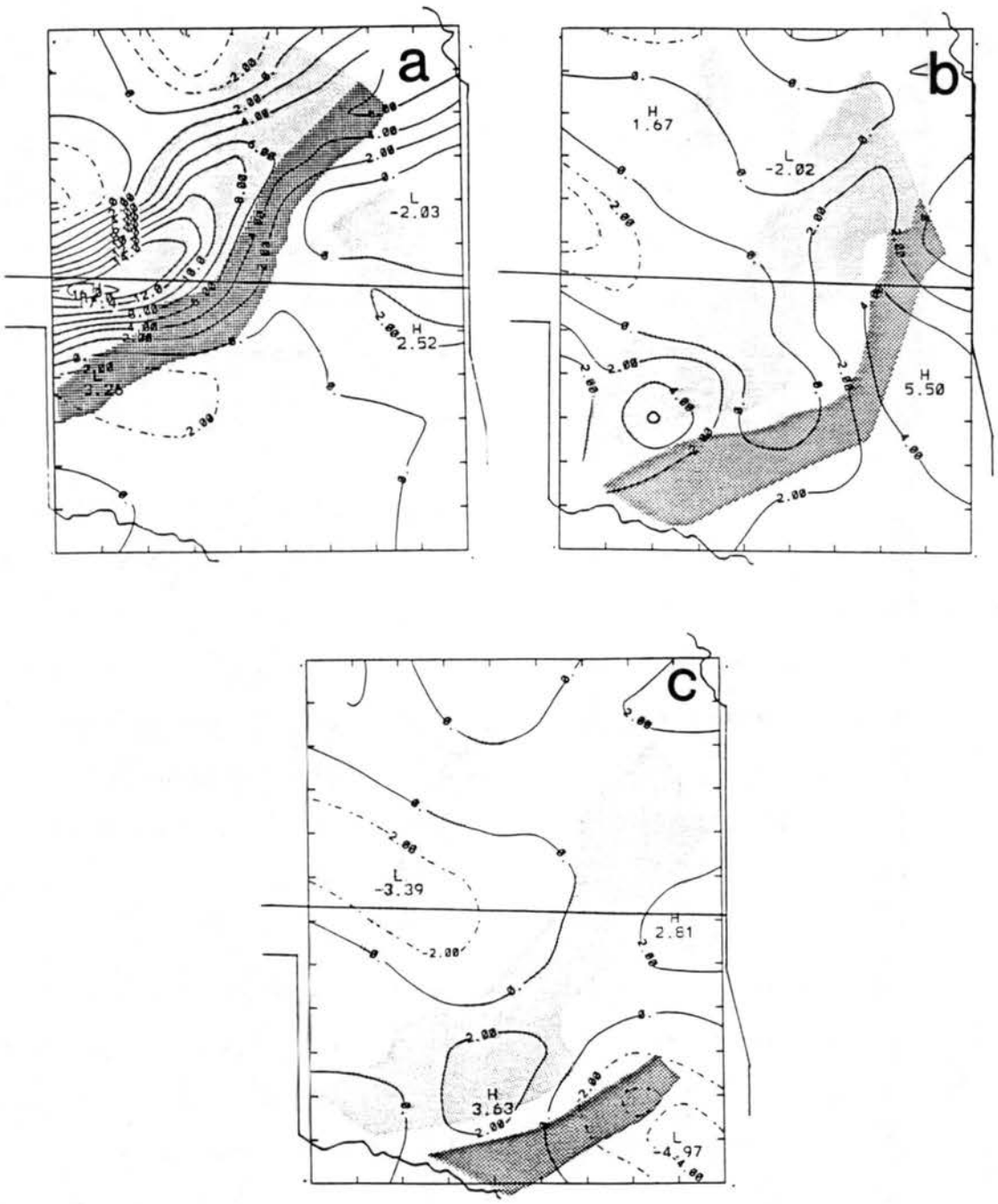

Figure 5.8: Same as Fig. 5.5, except for 300 mb.

mesoscale anvil over the stratiform region. Peak heating rates exceeded $14°C\ h^{-1}$ at 0300 UTC, but fell to 6-8$°C\ h^{-1}$ at later times. Maximum cooling rates are now found behind the radar echo, with peak values again aligned with the echo notch. This observation is consistent with the erosion of the stratiform precipitation area in this region. The cooling rates were greatest at this level, exceeding $6°C\ h^{-1}$ at all times. At 300 mb (Fig. 5.8), heating of nearly $18°C\ h^{-1}$ can be found over the southern part of the stratiform region at 0300 UTC, but heating rates at later times have fallen off from their lower-level values. Little cooling can be found at this level, and the maximum cooling rates were within the narrow zones of strong descent aligned with the echo notch.

5.2 Spatial and temporal variations of the moisture budget

The apparent moisture sink, Q_2 in Eq. (2.6), is calculated by taking the total derivative of the specific humidity. Q_2 is a measure of the drying that occurs as water vapor condenses into liquid water, or the moistening that occurs as liquid water evaporates at a point, along with the change in vapor due to the vertical divergence of the eddy moisture flux. Condensation results in positive values of Q_2 , or a sink in moisture. The apparent moisture sink is typically expressed in units of heating rate (Yanai *et al.*, 1973; Johnson, 1980; Houze, 1982; Kuo and Anthes, 1984; Johnson, 1984), and though these rates resemble those obtained from the heat budget, differences in the locations of extrema between budgets are common.

Figure 5.9 shows the evolution of Q_2 on vertical cross-sections. Because narrow dry layers were occasionally present in certain regions of the data network, the field of Q_2 is noisier than that of Q_1 . Moisture varied in the vertical more than temperature. At 0300 UTC, the condensational drying within the squall line is easily seen within a vertical band roughly 150 km wide. A double peak structure can be seen, with the lower peak of $6°C\ h^{-1}$ near the leading edge of convection, and the higher peak of over $8°C\ h^{-1}$ in the stratiform region. The double peak structure is commonly found in moisture budgets and will be discussed further at a later point. Drying can also be seen in the shallow convection ahead of the line (at -200 km). Evaporational moistening was located near the rear of the

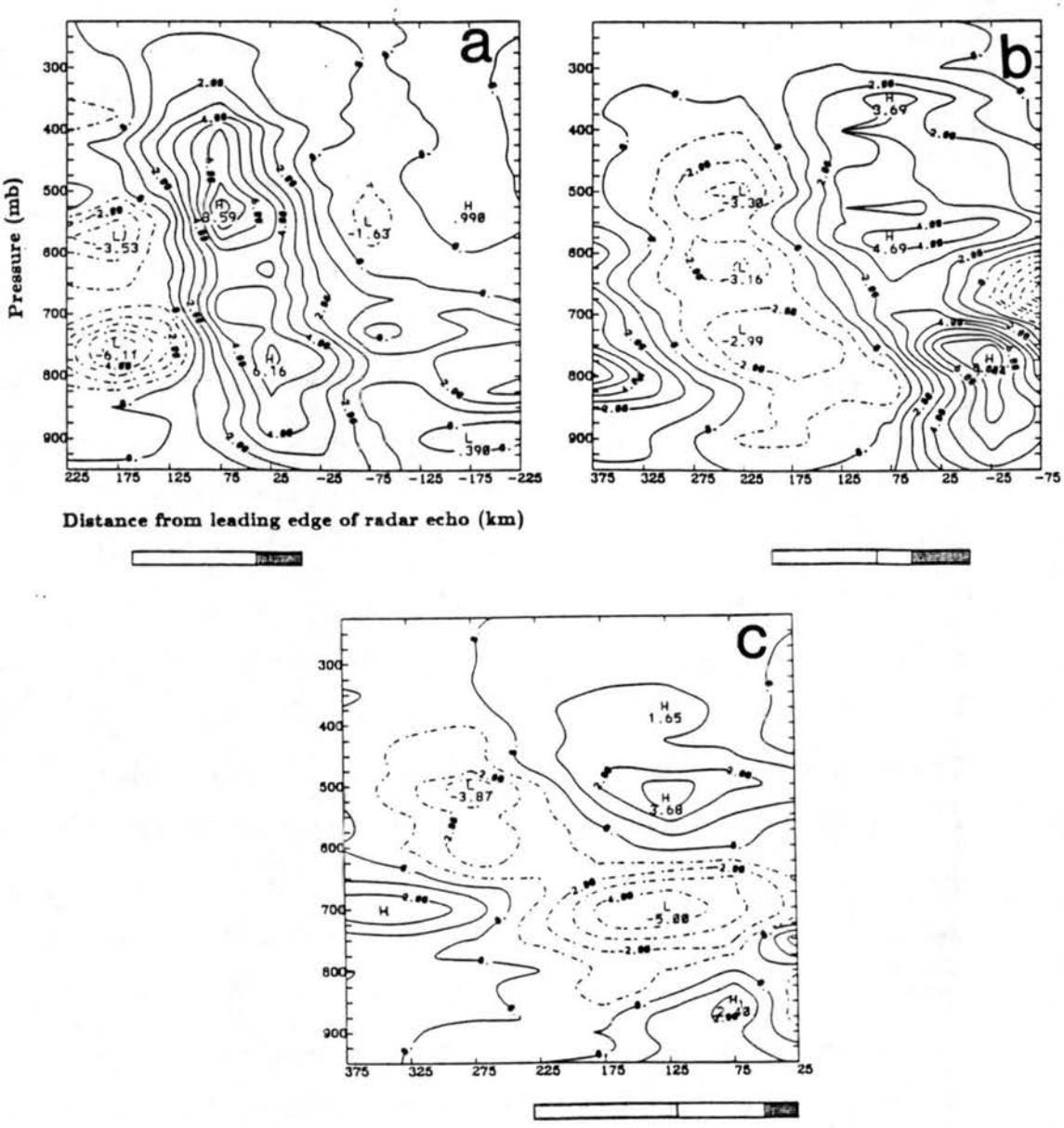

Figure 5.9: Apparent moisture sink Q_2 (expressed in $^oC\ h^{-1}$) at a.) 0300 UTC, b.) 0600 UTC, and c.) 0730 UTC. Positive values indicate drying, negative values moistening.

stratiform region in two small bands. There are some significant differences between the Q_2 field and the Q_1 field shown earlier (Fig. 5.1a). The axis of highest Q_2 , particularly at low levels, is displaced toward the front of the system compared to the axis of highest Q_1 . This displacement reaches 50 km at 0600 UTC. In addition, peak Q_2 values are found at lower levels.

The differences in the budgets are due to differences in the vertical profiles of dry static energy and moisture. Specific humidity drops off most rapidly with height at low levels, whereas dry static energy has its largest gradient at higher levels. As stated earlier, aliasing of data occurred in this study due to the 80 km spacing of the rawinsonde data used in the analyses. Convective line vertical motion was smoothed into regions ahead of the system and the stratiform region behind the line. Because the updraft sloped rearward with height, the most serious aliasing ahead of the line occurred at low levels where the updraft was closest to the leading edge of the system. Because the specific humidity gradient is a maximum in these low levels, the aliasing of high values of ω from the line to areas ahead of it resulted in the forward displacement of high Q_2 values at low levels. This displacement was not evident in the Q_1 fields because Q_1 depends on the gradient of dry static energy which is greatest at a much higher level where aliasing of intense upward motion into areas ahead of the system was not as great. At these high levels (for instance, 400 mb), the peak upward motion was located 75 - 125 km rearward of its peak at lower levels.

Another difference between the budgets can be seen in the area experiencing cooling due to evaporation. Although there was some evidence of two centers of cooling in the Q_1 field at 0300 UTC (Fig. 5.1a), the enhanced cooling was only slightly greater than that of the surrounding region, unlike the cooling (moistening) centers found in the Q_2 field (Fig. 5.9a). The magnitude of the cooling peak shown by the Q_2 field is several $^oC\ h^{-1}$ greater than that shown by the Q_1 field.

Figure 5.9b shows the field of Q_2 at 0600 UTC. Two primary peaks can still be seen in the drying profile, and the lower peak is now the greatest. Condensational drying of $9^oC\ h^{-1}$ can be found at 800 mb. The location of this peak is just ahead of the leading

edge of the radar echo. The forward displacement of this peak ahead of the radar echo is probably due in part to data aliasing, aggravated by the proximity of the leading convective line to the edge of the data network. Because pre-squall soundings were not available in front of certain portions of the system at 0600 UTC to better define the forward extent of the convective activity, data from within the convective line were occasionally smoothed forward to the eastern edge of the data grid. Moistening can be found over the stratiform region, and the area compares well with the cooling found in the Q_1 field (Fig. 5.1b). The magnitudes of the cooling in the Q_2 field are somewhat less, and the peak values are not concentrated like they were in the Q_1 field. An intense low-level zone of condensation can be found over 100 km behind the back edge of radar echo in the region of post-wake low ascent and showers.

One particularly strong dry layer diagnosed (that may be potentially spurious) was found near 650 mb in many of the soundings ahead of the line at 0600 UTC, and this feature results in a band of intense evaporation and cooling in this location. Some aliasing of this dry layer into the convective line did occur, resulting in values of Q_2 that may be a little low at this level in the convective line region. Some bogus soundings were added in this area (see Appendix A) to reduce aliasing problems, but the feature is still evident. It is possible that the convection which decayed in this region earlier produced subsidence and drying. The dry layer would appear in the soundings, but the vertical velocity calculations would not be able to pick up the small-scale sinking. Because this region is near the edge of the grid, upward vertical motion from the convective line was aliased into this area. The upward motion operating on a reversed vertical moisture gradient produces this Q_2 minimum.

At 0730 UTC (Fig. 5.9c), the field of Q_2 was quite similar to that of Q_1 . The peak drying (heating) rates were located toward the front of the stratiform region, with the peak Q_1 value only 100 mb higher than the peak Q_2 value. Because the convective line had moved away from the network, aliasing of values from that region into the mesoscale anvil was not as great here. The moistening peak near 500 mb coincides with a cooling peak found in the Q_1 field. The stronger Q_2 minimum near 700 mb was not present in

the Q_1 field. The small positive peak in Q_2 that occurs around 850 mb, 75 km behind the leading edge of the echo, is a feature not seen at earlier times. It may be a spurious feature resulting from inaccurate gridded data present near the southeastern corner of the grid network. It is also possible that this drying occurs from the entrainment downward of dry mesoscale downdraft air (Zipser, 1977) within the strong shear layer found in this region (see Fig. 4.2). The location of this Q_2 maximum is within the transition zone which was over 50 km wide at this time. Little or no rain was falling in this region, so that moistening due to evaporation of raindrops would not be occurring within the intense downdraft.

Fig. 5.10 shows vertical profiles of the moistening and drying rates in different regions of the squall line. As in the similar profile for Q_1 (Fig. 5.2), the cooling or evaporation within the mesoscale downdraft grew in depth as the system decayed. Likewise, the condensation and warming within the anvil ascent weakened over time. Peak moistening rates are found between 700 and 800 mb in the Q_2 profiles, similar to the cooling peaks in the Q_1 profiles. These moistening peaks are at somewhat higher levels than those found in a GATE case by Gamache and Houze (1983). The peak evaporation in the stratiform region of that tropical system (their Fig. 11) was typically occurring between 800 and 900 mb. The levels of maximum drying (heating) in the stratiform region are only slightly lower than those in the Q_1 profiles, but the curves are broader. Peak drying in the Gamache and Houze case was at roughly these same levels, varying from as low as 700 mb near the convective line to 400 mb at the rear of the stratiform rain area. The profiles of Q_2 in the convective line regions are noticeably different, with the two-peaked structure most evident at 0600 UTC. At that time, the maximum drying was just below 750 mb. This low level peak agrees with the results found in most other budget studies.

Comparisons between the vertical profile of Q_2 averaged over the entire June 10-11 system and several other tropical and midlatitude cases can be found in Fig. 5.11. The drying rate for this system (Fig. 5.11a) peaked between 500 and 600 mb, as opposed to the 400 mb peak in Q_1 (See Fig. 5.3a). The curve is very broad, with weak evidence of the double peak structure found in most moisture budgets (Johnson, 1976, and Lewis, 1975, in

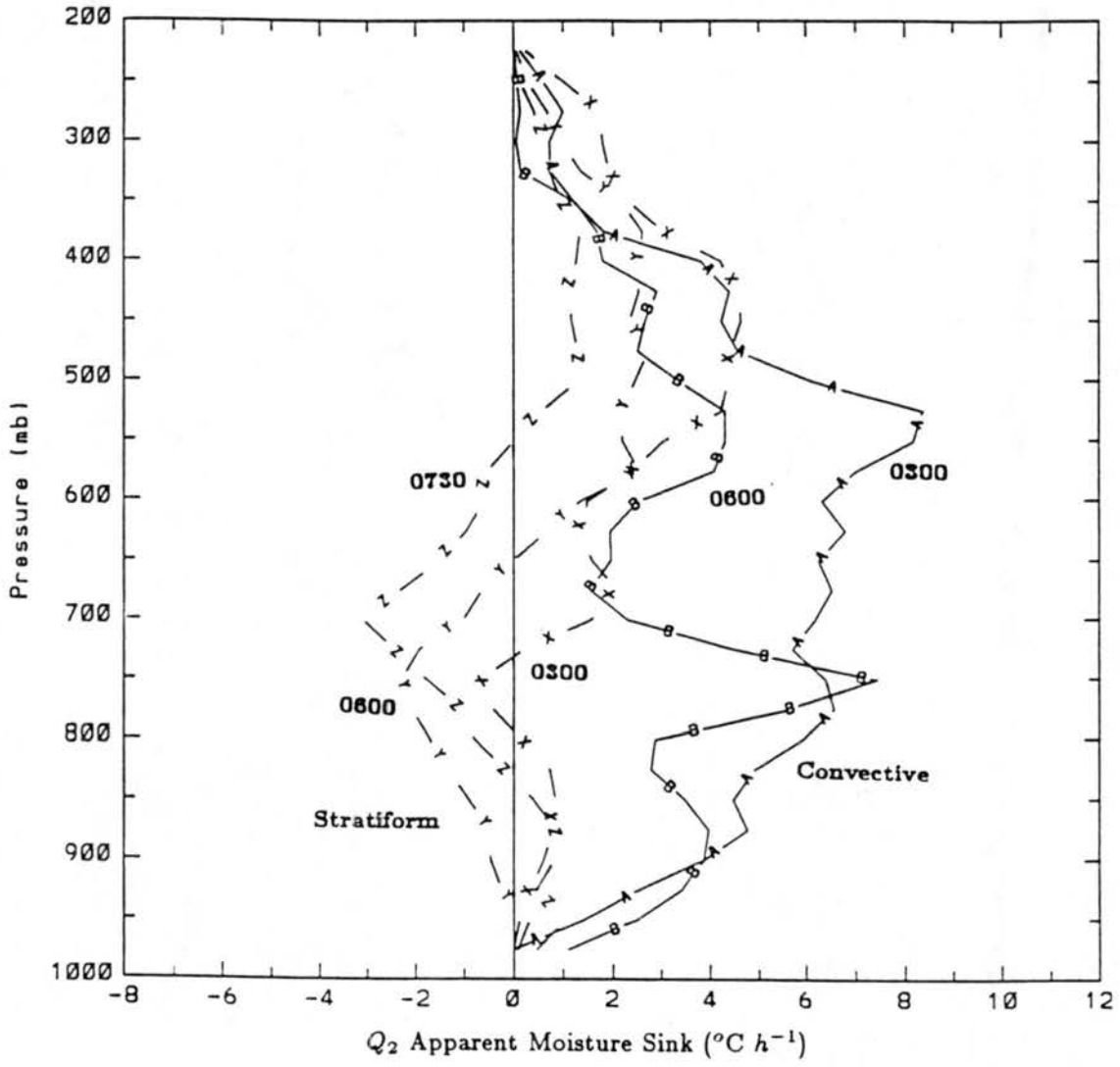

Figure 5.10: Vertical profiles of Q_2 averaged over the convective and stratiform rain regions of the squall line at different times. Solid lines represent convective line, dashed lines stratiform region. Lines A and B taken in the convective line at 0300 and 0600 UTC, respectively, and X, Y, and Z in the stratiform region at 0300, 0600 and 0730 UTC.

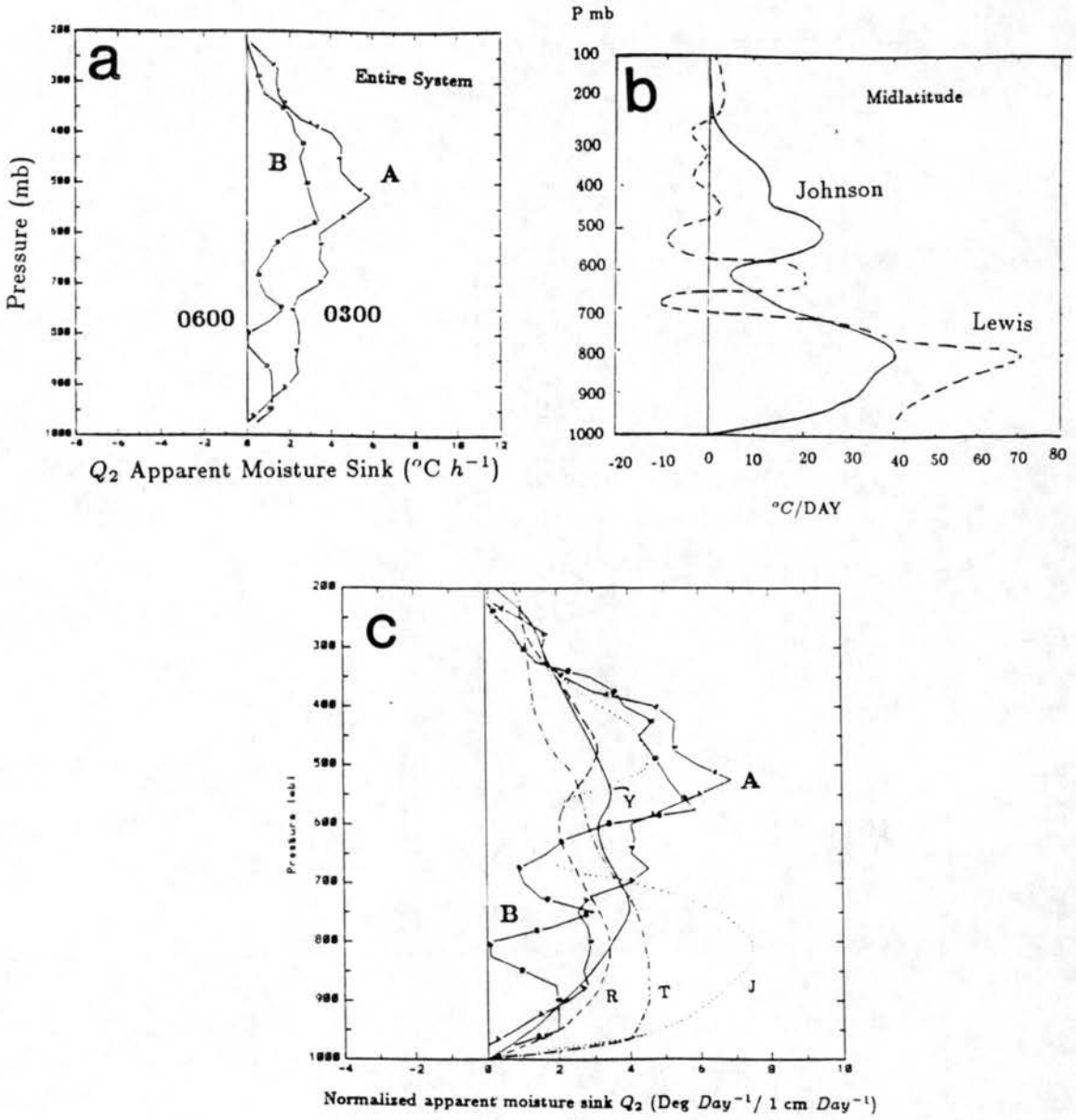

Figure 5.11: Comparison of system-averaged vertical Q_2 profiles for several cases. June 10-11 squall line shown in a.) at 0300 UTC (curve A) and 0600 UTC (curve B). In b.) midlatitude cases are shown from Johnson (1976, solid line) and Lewis (1975, dashed line). Fig. 5.11c shows the Q_2 profiles normalized to the observed rainfall rates. Curves A and B are from the June 10-11 case at 0300 and 0600 UTC. Other curves (after Johnson, 1984) are from cases by Yanai *et al.* (1973, curve Y), Thompson et al. (1979, curve T), Johnson (1984, curve J), and Reed and Recker (1971, curve R). Note different scales with each figure.

Fig. 5.11b; Yanai *et al.*, 1973, and Reed and Recker, 1971, in Fig. 5.11c). Esbensen *et al.* (1988) also found that a double-peak structure formed in the Q_2 profiles during the mature and dissipating stages of several GATE cloud clusters. The double-peak profile is a result of the combination of two different drying processes (Johnson, 1984). Cumulus drying occurs at low levels in the convective line with drying due to condensation in the anvil at high levels. The lower peak in the system average for this case was negated to a large extent by the moistening occurring at these same levels within the extensive stratiform region. The apparent sink (positive Q_2) below cloud base found in the convective regions and the 0300 and 0730 UTC stratiform regions in Fig. 5.10, and in the system averages (Fig. 5.11) for this case and the other studies has been associated with drying due to the introduction of dry air in the subcloud layer by convective processes (McNab and Betts, 1978). The low level peak in the convective line is pronounced only at 0600 UTC for this case, when it appears sharply at 750 mb (Fig. 5.10). Aliasing of data hides the low level peak in the 0300 UTC curve. As in the profiles of Q_1 , the magnitudes of the Q_2 profiles for this case study are generally much greater than those found in the other studies. The decrease in Q_2 values from 0300 to 0600 UTC is far more noticeable than the corresponding decrease in Q_1 values (Fig. 5.3a).

Fig. 5.11c shows Q_2 profiles normalized similar to the Q_1 profiles in Fig. 5.4a. Normalizing again minimizes the differences in magnitudes between the different cases. The peak values of Q_2 for the June 10-11 case appear reasonable, with magnitudes similar to the Florida case studied by Johnson (1976; curve J). The location of the peak values is different from the other four cases, with the June 10-11 peaks between 525 and 575 mb. This is near the level of the weaker, upper peak for the cases having a double-peak profile. The other cases had maximum Q_2 values below 700 mb. The moistening (negative Q_2) occurring within the stratiform region of the June 10-11 case appeared to be much more intense than in the other cases, and this moistening cancelled out the lower-level peak which normally is the greatest.

Figures 5.12 - 5.15 show the variation of gridded values of Q_2 across the PRE-STORM region. At 850 mb (Fig. 5.12), the most intense drying was located at or

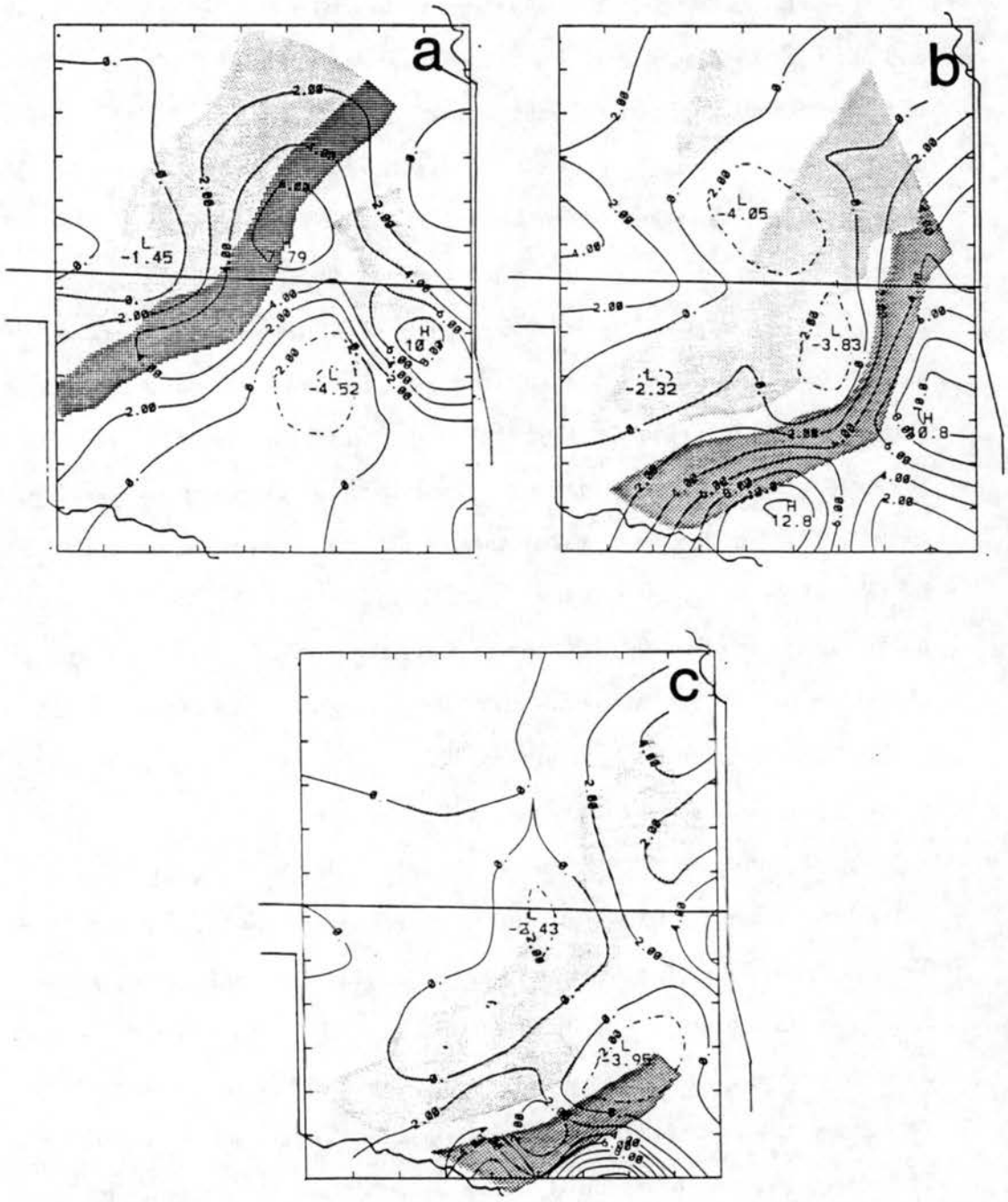

Figure 5.12: Fig. 5.12 Q_2 (in $^oC\ h^{-1}$) at 850 mb in the PRE-STORM region for a.) 0300 UTC, b.) 0600 UTC and c.) 0730 UTC.

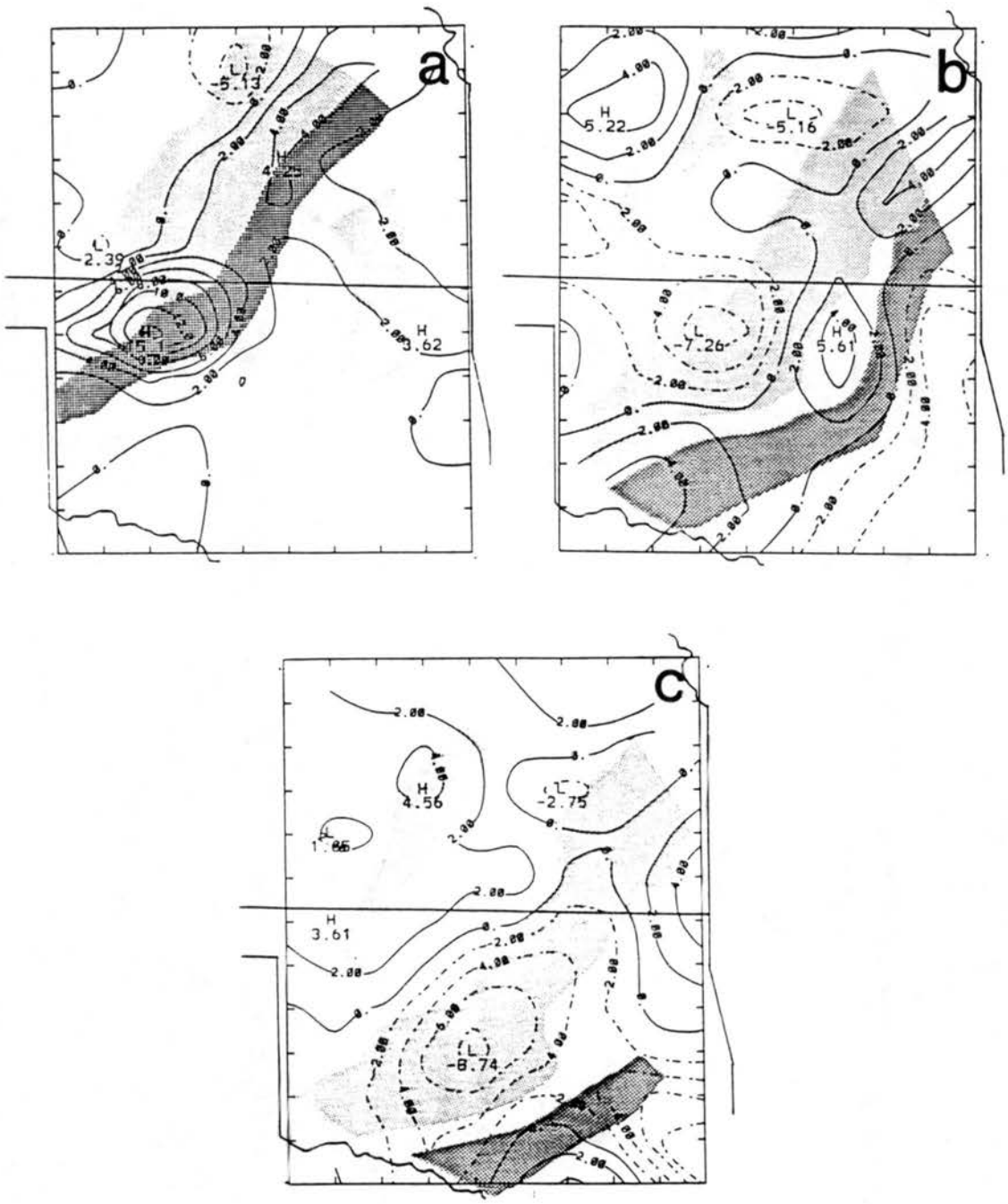

Figure 5.13: Same as Fig. 5.12, except for 700 mb.

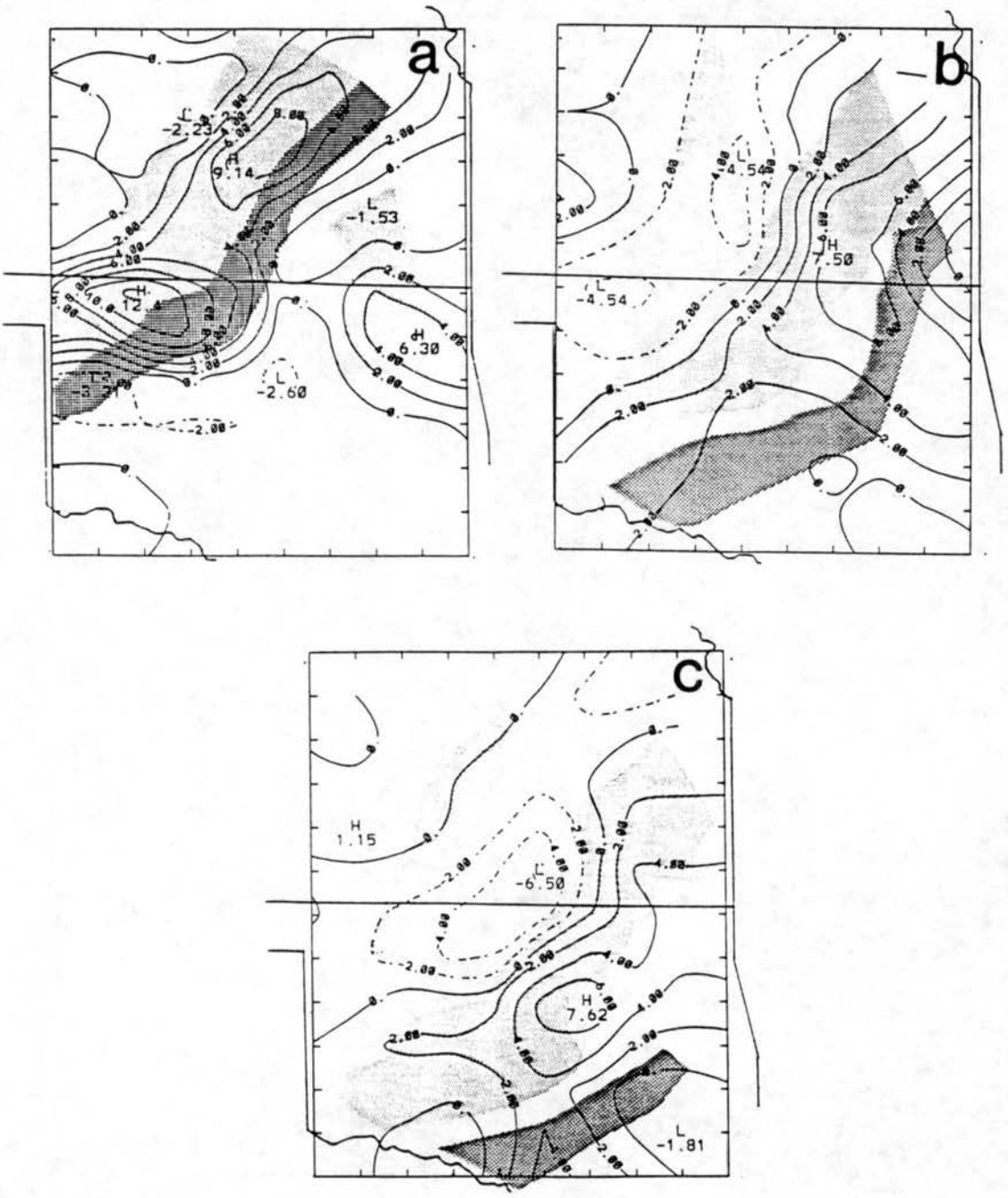

Figure 5.14: Same as Fig. 5.12, except for 500 mb.

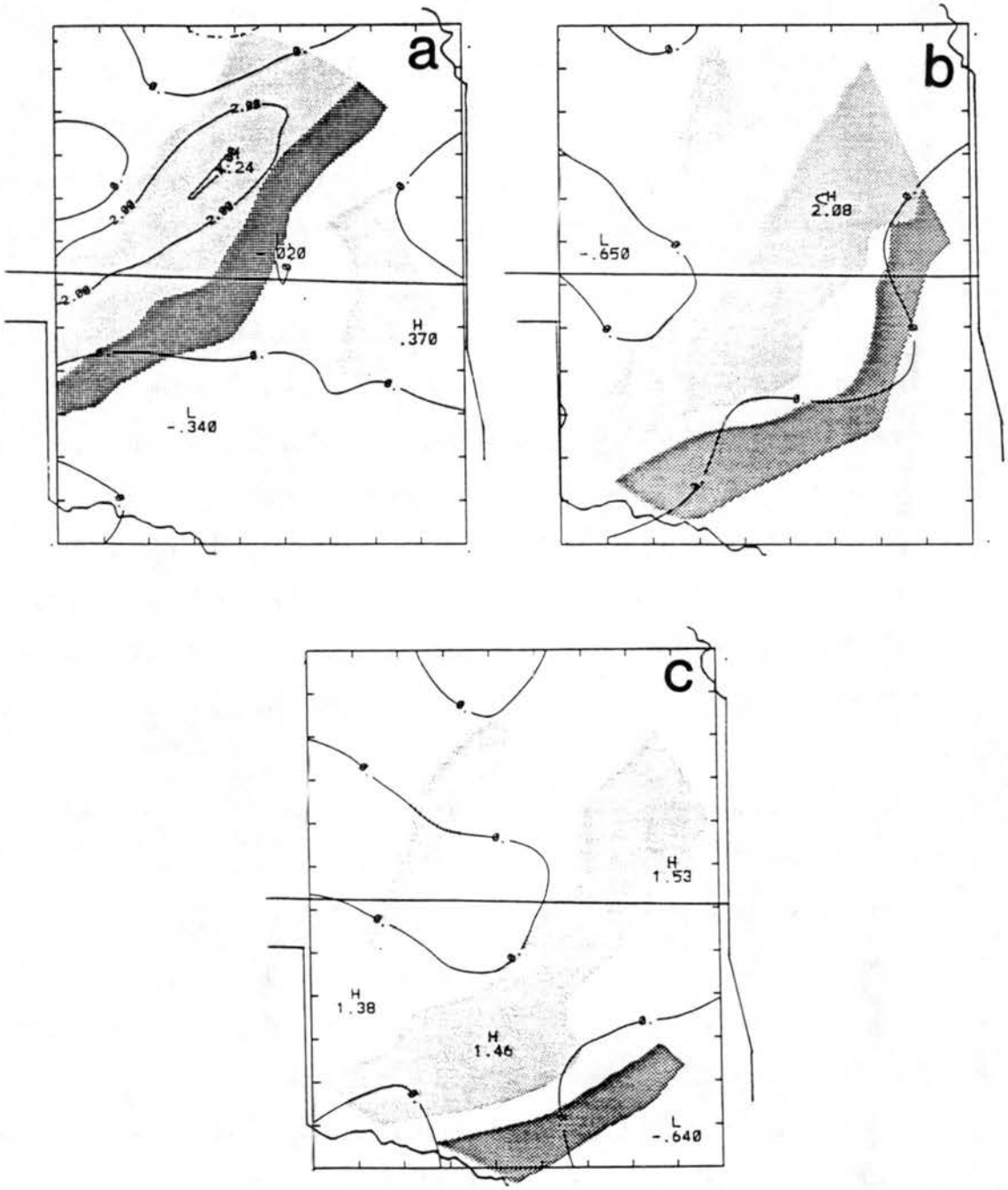

Figure 5.15: Same as Fig. 5.12, except for 300 mb.

just ahead of the leading edge of the radar echo. The aliasing of convective line ω into areas ahead of the system was most pronounced at this level, accounting for the rather high values of Q_2 found over 50 km ahead of the leading edge of echo in some areas, especially at 0600 UTC. Unlike the Q_1 field, Q_2 increased from 0300 to 0600 UTC. Peak values of drying reached $13°C\ h^{-1}$. High values of Q_2 are found at 0300 UTC near the showers ahead of the main system. Cooling associated with evaporative moistening was concentrated over the stratiform rain region, with peak values near the back edge of radar echo.

The moistening (cooling) rates near the rear of the system increased at 700 mb (Fig. 5.13), and seemed to intensify over time with peak values of nearly $9°C\ h^{-1}$ within the stratiform region at 0730 UTC. The two centers of enhanced moistening, especially visible at 0600 and 0730 UTC, are correlated well with two centers in the Q_1 field at this level (Fig. 5.6). The zone of drying (heating) near the front of the system shifted rearward from 850 mb. At 0300 UTC, rates had increased to $15°C\ h^{-1}$, but rates at the other times had decreased from lower-level values. The updraft at 0300 UTC was much stronger than at the later times, and this would account for the relatively high drying rates at this higher level.

Fig. 5.14 shows the Q_2 field at 500 mb. In general, the areas of drying had intensified and expanded. The drying was now centered more over the stratiform region, showing the condensation taking place in the mesoscale updraft within the large anvil. Moistening was still occurring behind this zone, and the maximum rates are found behind the back edge of the echo. Because moisture drops off rapidly with height, the Q_2 field at 300 mb (Fig. 5.15) is smooth with low values of drying and moistening, compared with the Q_1 field at this level (Fig. 5.8). Peak drying (heating) rates are over the stratiform region, with weak moistening (cooling) evident in narrow bands directed toward the echo notch.

The difference between Q_1 and Q_2 (assuming Q_R is small) is a measure of the vertical convergence of the vertical eddy transport of total heat, and it can be used to measure the activity of cumulus convection (Yanai *et al.*, 1973). Fig. 5.16 shows the vertical profile of this transport for the convective line (a) and stratiform (b) regions of this system. In

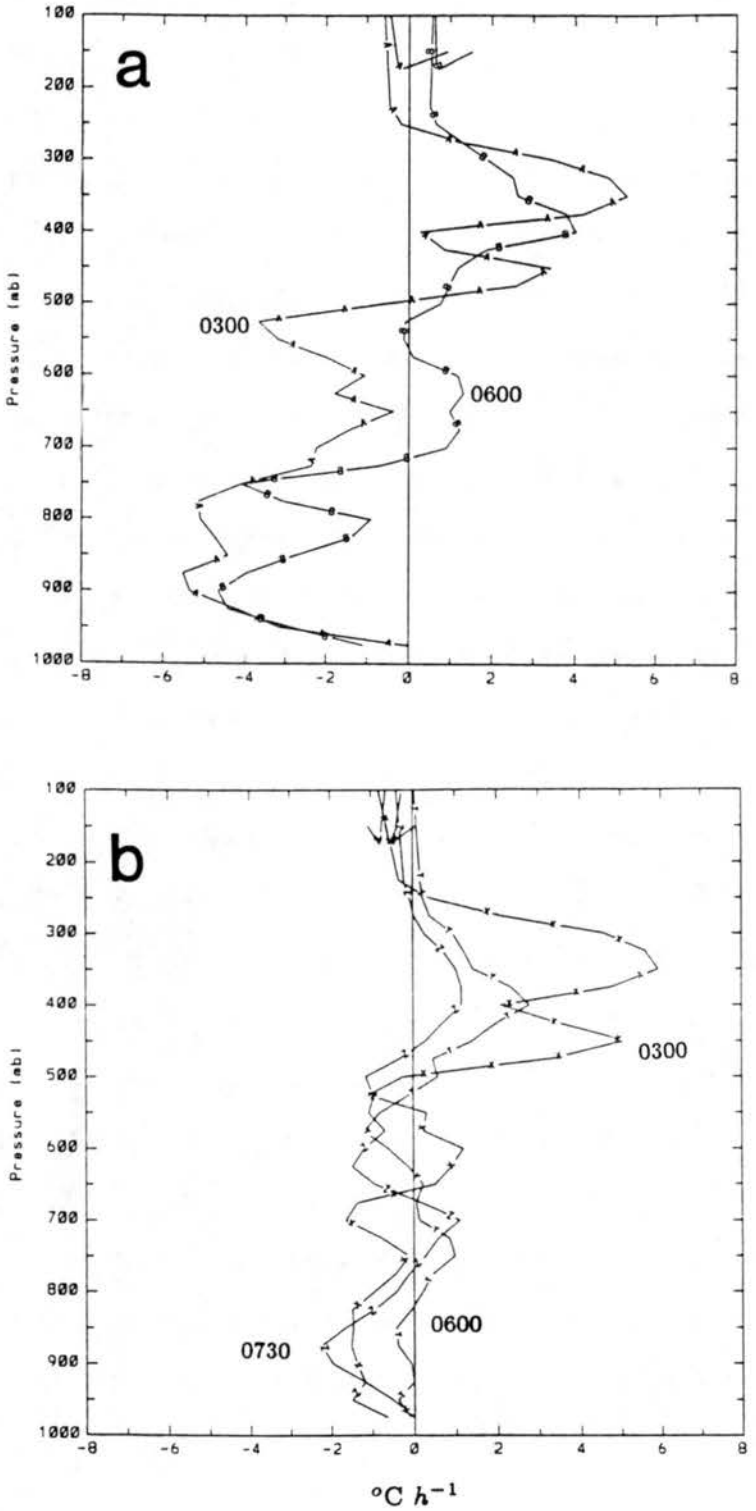

Figure 5.16: Vertical convergence of the vertical eddy transport of total heat (Q_1 - Q_2) in units of $^oC\ h^{-1}$ for a.) convective line regions, and b.) stratiform regions of the system at different times. Lines A and B in (a) taken from convective line at 0300 and 0600 UTC, respectively. Lines X, Y and Z in (b) from stratiform region at 0300, 0600 and 0730 UTC.

general, the quantity was negative below about 500 mb, and positive above that level. This is a result found also by Yanai *et al.* (1973), Lewis (1975) and Arakawa and Chen (1986), and it reflects the mid-level minimum in moist static energy. This result shows the importance of convective systems in transporting heat to high levels of the atmosphere. As stated in Chapter 2, a good indicator of whether or not stratiform rain is occurring within a convective system is whether or not the convective vertical transport is nearly zero. In spite of the aliasing that occurred between the convective line and stratiform regions in the analyses of Q_1 and Q_2 for this case, the three curves representing the stratiform regions at different times in Fig. 5.16b generally remain close to zero, except at high levels.

Eq. (2.11) predicts that the vertical eddy transport of total heat for the entire system at the surface (the integration through the depth of the troposphere of the curves in Fig. 5.16) should be relatively small since S_o and LE_o are assumed to be small, and hence F_o would also be small. Integration of (Q_1 - Q_2) from the tropopause downward yields the vertical eddy flux of total heat at any level (Fig. 5.17). This quantity was positive over all of the troposphere, except at the highest levels, with peak values of over 2000 $W\ m^{-2}$ at 0300 UTC around 500 mb, and about 1300 $W\ m^{-2}$ at 0600 UTC around 700 mb. These values are significantly larger than the 400 $W\ m^{-2}$ values found at the mid-level peaks in budgets done on larger spatial and temporal scales by Yanai *et al.* (1973) and Esbensen *et al.* (1988). Both curves in Fig. 5.17 became smaller near the surface. Eq. (2.11) predicted that the value of the transport should be relatively small there. At 0300 UTC, the value of the eddy flux was less than 50 $W\ m^{-2}$. At 0600 UTC, although the flux was small relative to its magnitude elsewhere, the value was still rather large, 500 $W\ m^{-2}$. Radiative cooling was ignored in Eq. (2.11), and the cooling if included would have resulted in slightly more positive values of the vertical eddy flux of total heat. The large positive values of the eddy flux at the surface at 0600 UTC appear to be a result, in part, of the displacement of the Q_2 maximum forward at low levels, because of aliasing problems. This displacement meant that Q_2 averaged over the system was not as large as it should have been at low levels. It is at low levels where the apparent moisture sink is greater than the apparent heat source, resulting in negative values of (Q_1 - Q_2). Without

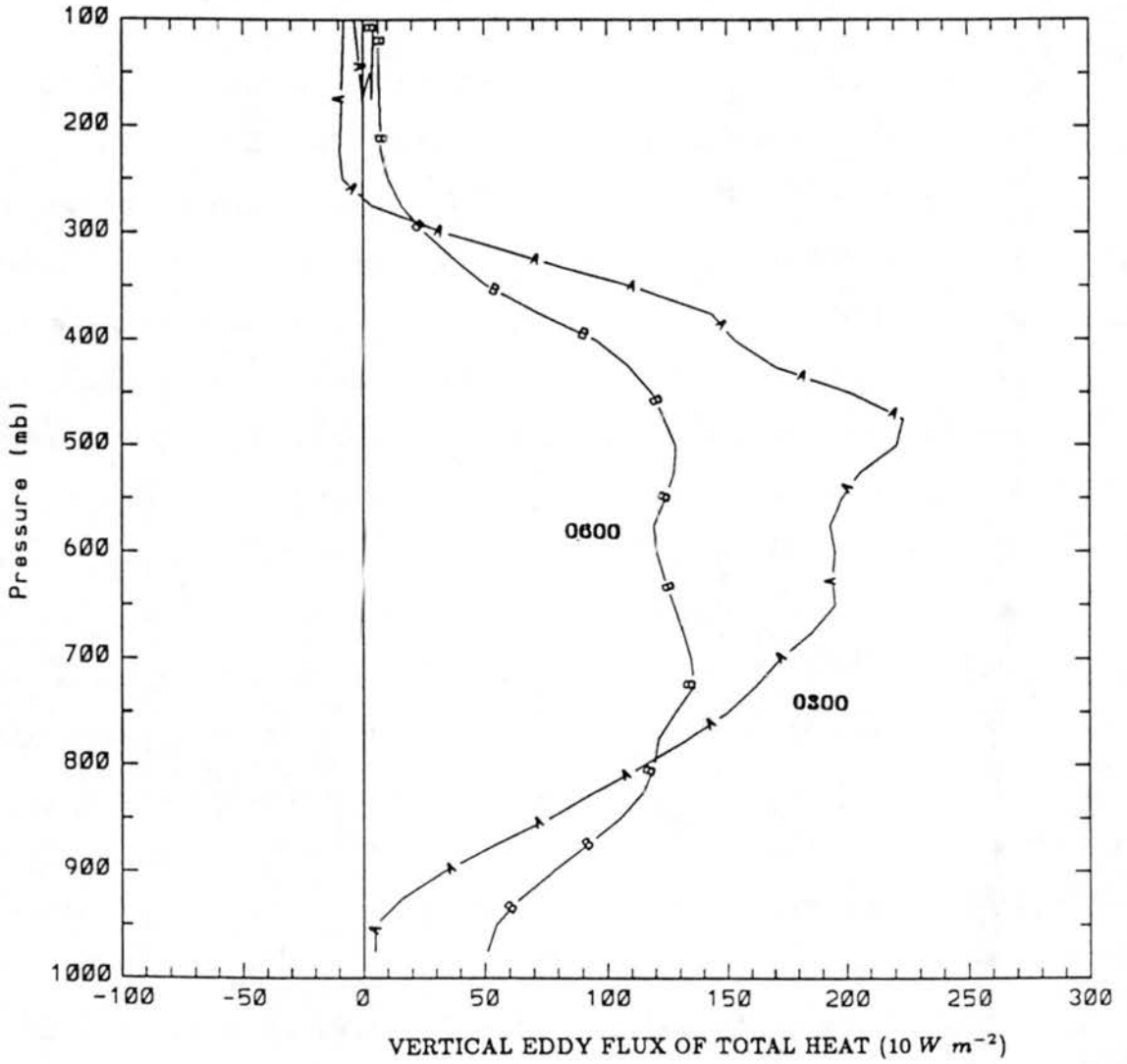

Figure 5.17: Vertical eddy flux of total heat for the entire system at 0300 UTC (curve A) and 0600 UTC (curve B).

the large aliasing problems at 0600 UTC, the vertical eddy flux of total heat at the surface would likely have been closer to zero, as expected from Eq. (2.11).

5.3 Comparison of predicted and observed rainfall rates

When heat and moisture budgets are integrated in the vertical, precipitation rates can be obtained and then compared to observations as a check to the accuracy and reliability of the budgets. (See Eqs. 2.9 and 2.10.) In budgets of tropical convection done over long periods of time, cloud storage is relatively small, and the integrated budgets should agree closely with observed precipitation rates. Any errors are typically due to problems in estimating surface heat flux, surface evaporation, radiative heating, and measuring the actual precipitation accurately. In budgets done over short time periods, radiative heating, and surface terms are small compared to condensation and evaporation within convection and can be neglected. Within the stratiform region of a convective system, the radiative heating and surface terms are not necessarily as small compared to the net evaporation or condensation and may be more important, but for this case, occurring at night, such terms would be relatively insignificant. Cloud storage, however, can be important in both regions of an MCS and can result in some discrepancy between the integrated budget results and the observed rainfall rates (McNab and Betts, 1978; Johnson, 1980). Cloud storage has been especially considered significant in regions of rapidly developing cloudcover like the formative stages of convective systems. Little research has been done on the importance of storage of liquid water during the decaying stages of large mesoscale convective systems, although Cotton *et al.* (1989) show that precipitation efficiency exceeds 100% during the later stages of an MCS, implying that storage is important.

Figures 5.18 and 5.19 show the rainfall rates calculated from the heat and moisture budgets respectively for the grid points in the PRE-STORM region. Positive values represent a predicted rainfall rate, and negative values indicate a net evaporation with no rainfall predicted. Both integrated budgets predicted a decrease in the peak rain rates as the system decayed. Rainfall rates were predicted to exceed 20 $mm\ h^{-1}$ at 0300 UTC, and fall to 15 $mm\ h^{-1}$ or so by 0600 UTC, and around 10 $mm\ h^{-1}$ by 0730 UTC. Both

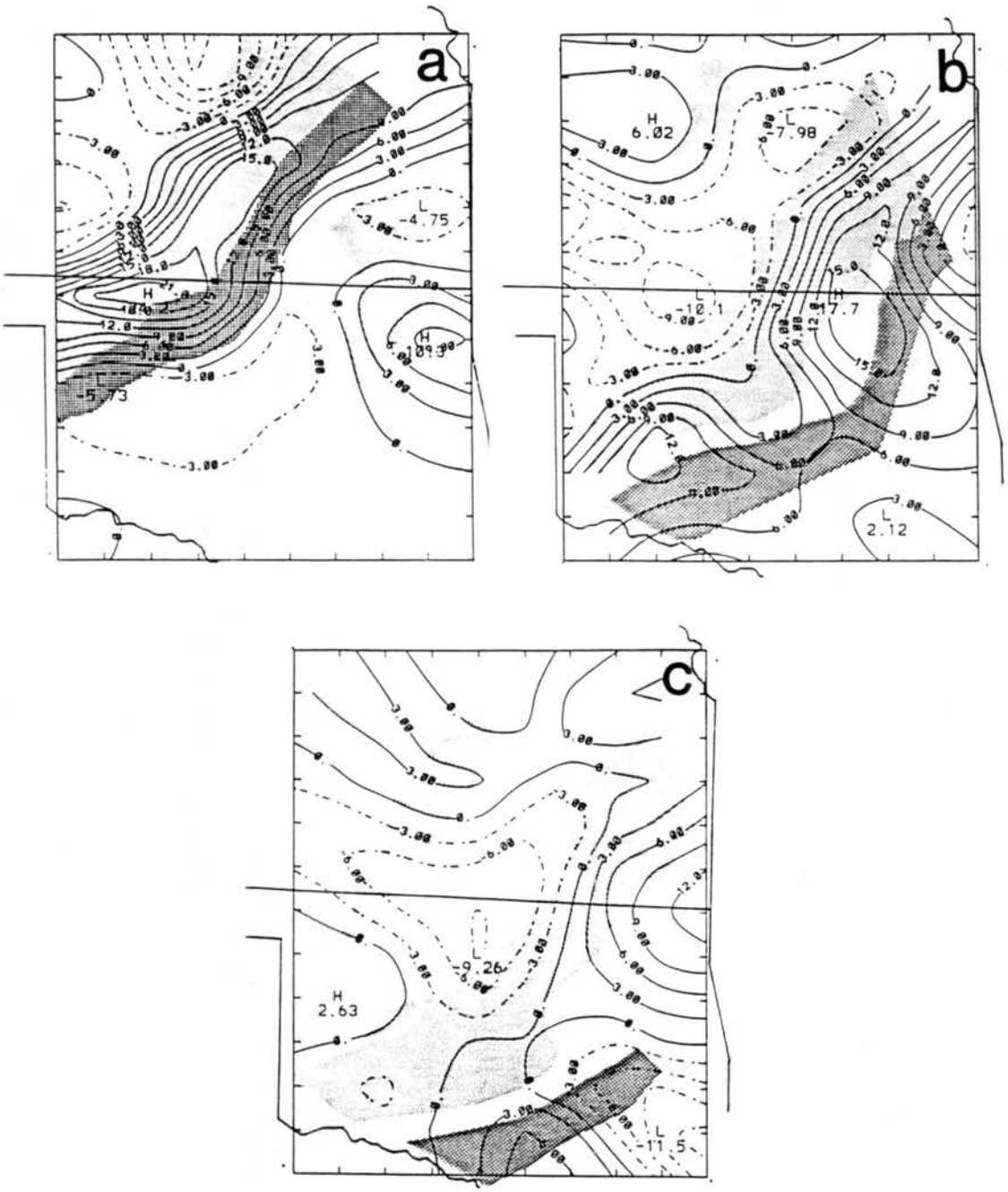

Figure 5.18: Fig. 5.18 Predicted rainfall rates (in $mm\ h^{-1}$) from the vertically integrated heat (Q_1) budget for a.) 0300 UTC, b.) 0600 UTC and c.) 0730 UTC.

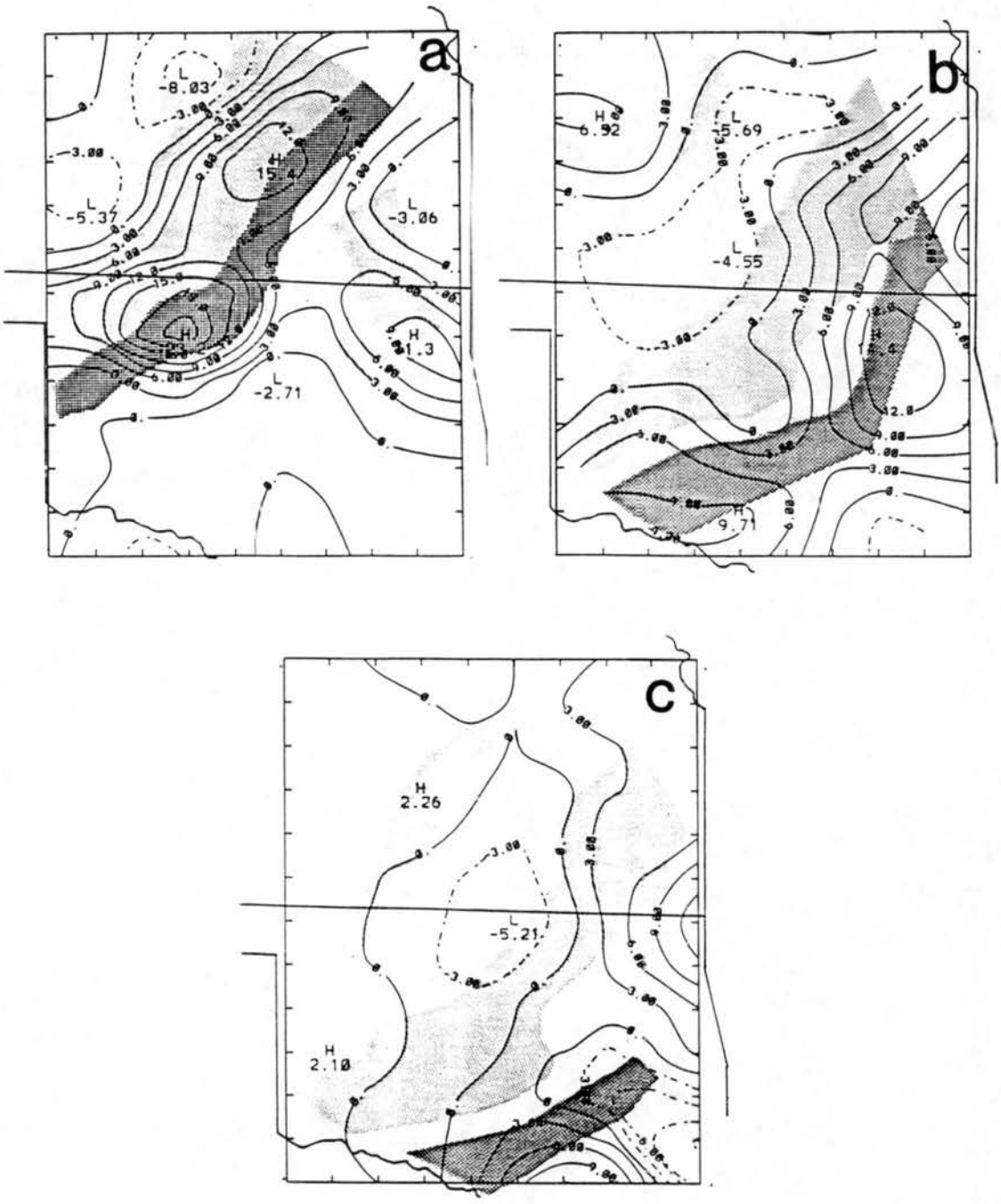

Figure 5.19: As in Fig. 5.18, except for the vertically integrated moisture (Q_2) budget.

budgets yielded estimates within a few $mm\ h^{-1}$ of each other for the peak values which were found near the convective line. The axis of heaviest rainfall rates associated with the convective line from the integrated Q_2 values (Fig. 5.19) was displaced forward from the axis determined by the integrated Q_1 values (Fig. 5.18). This is reasonable considering the displacement seen earlier in the peak values of Q_2 and Q_1 . The displacement did not affect other features in the field, and the axis of most intense evaporation, along with the zero line near the back edge of the echo were in agreement for the two methods.

The actual rainfall rates determined from the PAM/SAM mesonet surface stations can be seen in Fig. 5.20. A subjective analysis was done at the three budget times, with rainfall rates calculated by taking the accumulated precipitation over 20 minute periods centered at the times used in the compositing of the soundings. Peak rates observed within the three hour time interval were also considered and were displaced a distance from the mesonet site depending upon the time that they occurred. Because the rainfall rates varied over time more than the sounding variables, widely differing values were sometimes located in approximately the same location. When this occurred, averaging of the values was done, with more weight given to the value associated with the actual budget time. The peak rates observed by the PAM/SAM stations fell from over 50 $mm\ h^{-1}$ at 0300 UTC, to around 35 $mm\ h^{-1}$ at later times, and the area within the convective line having over 10 $mm\ h^{-1}$ of rain (shaded in Fig. 5.20) decreased steadily during the three budget times. The area covered by stratiform rain (rates generally less than 6 $mm\ h^{-1}$) increased substantially from 0300 to 0600 UTC, and then remained constant through 0730 UTC. Although the rainfall rates within the stratiform region varied far less than those within the convective line, local extrema can be found, and some areas near or within the transition zone had almost no rain at the budget times.

Horizontal cross-section maps comparing the actual and predicted rainfall rates over a small region have been shown in only a few previous studies (e.g. Chen and Zipser, 1982; Kuo and Anthes, 1984, on a larger scale) . The rawinsondes cannot resolve the small-scale structure of rainfall rate variations within the system, and grid point values of Q_1 and Q_2 can have large errors associated with them (Kuo and Anthes, 1984). Both

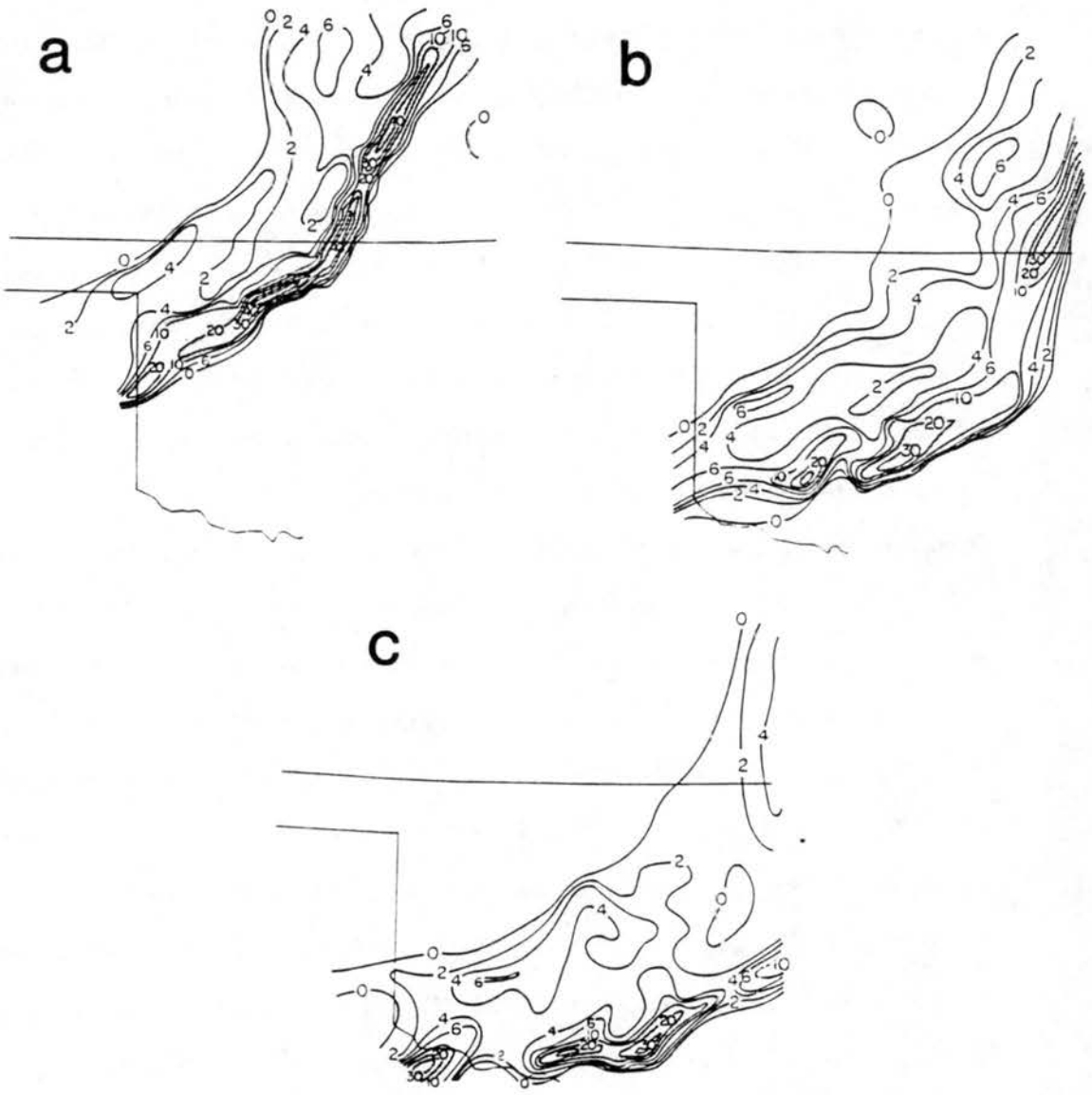

Figure 5.20: Observed rainfall rates (in $mm\ h^{-1}$) for the PRE-STORM region using PAM and SAM mesonet data at a.) 0300 UTC, b.) 0600 UTC and c.) 0730 UTC.

the integrated heat and moisture budgets at 0300 UTC showed the maximum rate in the southern part of the system, over northwestern Oklahoma. The actual rates were most intense in the southern part of the line; however, the peak predicted rates were only 40% of the observed. This is a result of the poor ability of the rawinsonde network to resolve convective-scale processes. The integrated budgets at 0600 UTC showed two regions of more intense rainfall, separated by a zone of rather light rain in the convective line. The observations are in agreement, showing two similarly-located intense rain regions and a zone between them where the rain rates were decreasing dramatically. The budgets tended to shift these features roughly 100 km south of their actual location. By 0730 UTC, the budgets did a poor job of showing the rain rates with the squall system, probably because the squall line was leaving the data network. At both earlier times, the budget-predicted back edge of rain was located a small distance (usually less than 30 km) ahead of the actual termination line. One exception is in the integrated moisture budget at 0600 UTC (Fig. 5.19b) where a narrow band aligned with the echo notch in Oklahoma, and extending into the transition zone, was predicted to have a negative rainfall rate. This band of light rainfall rates also showed up in the integrated heat budget, although the rates were slightly positive there. The actual rain rates seen in Fig. 5.20b did show a pronounced rainfall minimum in this region, with rates falling to less than 2 $mm\ h^{-1}$. Along the entire rear of the system where light rain was still occurring, the diagnosed rain rates were negative. Chen and Zipser (1982) also found negative rain rates within the stratiform region of a GATE squall line. Negative rain rates show that a rearward transport of hydrometeors along with water storage are important in producing precipitation in the stratiform region (Rutledge and Houze, 1987).

Most budget studies compare the predicted and observed rainfall rates averaged over the entire system, to minimize the problems of inadequate sounding resolution and large errors at individual grid points (e.g. Yanai *et al*, 1973; Lewis, 1975). Table 5.1 shows the predicted heat and moisture budget rainfall rates, and the observed values at 0300 and 0600 UTC for the convective line region, stratiform area, and entire system. Comparisons are also made for the stratiform region at 0730 UTC. The convective line region rates are

Table 5.1: Comparison of rainfall rate predictions (in $mm\ h^{-1}$) from the integrated heat and moisture budgets with observations averaged over different regions of the squall line. All regions are shown at 0300 and 0600 UTC. Only stratiform region data shown at 0730 UTC since convective line had left data network.

Region	Time	$\int Q_1$ dp (mm h^{-1})	$\int Q_2$ dp (mm h^{-1})	observed (mm h^{-1})
convective line	0300	9.8	13.5	20.5
	0600	8.5	8.4	12.9
stratiform	0300	8.1	5.6	3.3
	0600	3.0	1.6	3.3
	0730	0.0	0.0	2.3
total system	0300	8.8	8.7	8.5
	0600	5.6	4.4	5.8

underestimated by an average of 40%, because of resolution problems. The trend toward decreasing rates with time is evident, especially in the integrated moisture budget.

Resolution should not be such a problem for the stratiform region where processes operate more on the mesoscale. At 0300 UTC, both budgets predicted rates at least twice those observed. At least part of this overestimation is due to aliasing from the convective line region, since the system was relatively narrow at this time. At 0600 UTC, the heat and moisture budgets actually underestimated the stratiform rain rates by 10% and 50% respectively. The difference in rates was greatest with the moisture budget integration, over 1.5 $mm\ h^{-1}$. An underestimation also occured at 0730 UTC, when the integration of both budgets resulted in zero rain rates (the actual rate was just over 2 $mm\ h^{-1}$); however, at this time, the nearness of the system to the edge of the data network may have caused problems.

The discrepancy at 0600 UTC, and some of the difference at 0730 UTC can be explained in part by the transport of ice from the convective line into the anvil (Smull and Houze, 1987). This transport has been estimated to provide over 60% of the condensate within the mesoscale anvil cloud for some systems (Gamache and Houze, 1983). Precipitation content, M, (kilograms of ice per cubic meter of air) can be estimated from radar reflectivity (Smull and Houze, 1987) using

$$M = 8.0 \times 10^{-6}(4.68Z)^{.61}, \tag{5.1}$$

where Z is the liquid precipitation radar reflectivity. A crude estimate of the transport of this ice into the stratiform region and the amount that it could add to the rainfall rates, P, can then be made using

$$P = \frac{UMA}{\rho_{water}S}, \tag{5.2}$$

where U is the component of the wind normal to the back of the convective line, A is the area in the vertical through which the ice is being transported and S is the surface area over which the rain produced by the ice may fall out. Because it takes 2-3 hours from the time the ice is transported into the stratiform region to when it falls out as rain, Eq. (5.2)

was solved using average values of wind and relectivity, taken from the Doppler results of Smull and Houze (1987) for the system around 0400 UTC. An average value for the mass of water per volume at the rear of the convective line appeared to correspond to an average reflectivity of 25 dBZ, and a relative wind of 15 $m\ s^{-1}$ was used. The area in the vertical through which the transport was assumed to take place was 5 km deep and 500 km long, or $2.5 \times 10^9\ m^2$. The area of the stratiform region where the rainfall was assumed to be enhanced by this process was roughly 100 km wide and 500 km long, or $5.0 \times 10^{10}\ m^2$. Therefore, the transport of ice into the stratiform region could add

$$P = \frac{(15.0m\ s^{-1})(1.46 \times 10^{-4}kg\ m^{-3})(2.5 \times 10^9 m^2)}{(10^3 kg\ m^{-3})(5.0 \times 10^{10} m^2)} \approx 1.8mm\ h^{-1}$$

to the average stratiform rain rates. This transport of just less than two millimeters per hour would account for all of the difference between the observed rain rates and the integrated budget predictions at 0600 UTC, and most of the differences in the stratiform region at 0730 UTC. If the average reflectivity used in the equations is increased to 30 dBZ, the rain rates could be increased by 3.8 $mm\ h^{-1}$, more than enough to account for all of the underestimations. Several additional processes may also be operating. An additional transport of ice rearward due to the eddy flux within the convective cells may also increase rainfall rates. Finally, storage of liquid water within the cloud from earlier times may result in actual rain rates exceeding those predicted by the budgets. Cotton *et al.* (1989) showed that MCSs become very efficient rain producers during their later stages, with precipitation efficiencies exceeding 100%. Dual-Doppler radar data may permit estimates of these contributions to be made, but we have not conducted such an analysis.

The predicted rates for the entire mesoscale system were generally very close to the observed rates. Except for the moisture budget prediction at 0600 UTC, which was about 25% too low, the other predicted rates were within 5% of the actual rates. At 0300 UTC, both budgets predicted a rate nearly equal to the observed value. At 0600 UTC, the heat budget predicted a rate close to the observed one, but the moisture budget was over 1 $mm\ h^{-1}$ low. Low estimates may reflect the inability of the rawinsondes to measure the true intensity of updrafts within the system (as in Yanai *et al.*, 1973). In addition,

the especially low estimate from the moisture budget at 0600 UTC may be just another result of the forward shifting of the Q_2 maximum ahead of the line at that time. Kuo and Anthes (1984) found that the moisture budget was a better predictor of rainfall rates in their case than the heat budget. For this study, that does not appear to be the case. The increasing underestimation of the predicted rates within the stratiform region and the entire system from 0600 to 0730 UTC may indicate that stored liquid water falls out as the upward motion weakens. Budgets for the growing stage of the line (00 - 03 UTC) should overestimate rainfall. Lewis (1975) also found in a study of mature midlatitude convection that the budget-integrated rates were about 0.5 $mm\ h^{-1}$ lower than the observed rates over the area receiving precipitation. He showed that this discrepancy could occur if any of the larger scale terms of the budgets had an error averaging around 0.1 g $kg^{-1}\ h^{-1}$. In all of the different regions of the system, the differences between the heat budget integrations and moisture budget integrations decreased over time, showing that the precipitation was becoming more stratiform, and the convective eddy heat transport was decreasing, a result that was seen in Fig. 5.16.

Finally, the values given as observed are subject themselves to some error. Obtaining accurate surface rainfall measurements is an ongoing problem in field experiments. The SAM mesonetwork accumulated rainfall appeared to increase in increments of 1 mm, so that a steady light rain showed up in the data as occasional rises in the accumulated rainfall after periods of 20-40 minutes or more. Therefore, some subjectivity was involved is estimating the true rainfall rates. In addition, the use of PAM/SAM data meant that the actual rain rates were computed from over 200 composited data points, while the budget predictions were made from only 30 or so rawinsondes. If only those PAM/SAM sites located at the positions of the rawinsonde sites were used to determine the observed rainfall rates, the observed values would decrease, especially within the convective line region.

In general, the predicted rates for the entire system, along with the location of expected rainfall agreed reasonably well with observation, throughout the time period looked at in this study. The system-averaged rates, in particular, agreed remarkably well with

observations. This, in addition to the accurate portrayal of temporal trends, reflects the credibility of the heat and moisture budgets for this case.

Chapter 6

MOMENTUM BUDGET

The purpose of this chapter is to present the momentum budget of the component of the wind normal to the main axis of the June 10-11 squall line during its late mature through decaying stages. Comparisons will be made with momentum budget studies of midlatitude squall lines (Sanders and Emanuel, 1977; Smull and Houze, 1987) and tropical squall lines (LeMone, 1983). Because this system contained a pronounced mid-level mesolow, with relatively large height variations across the PRE-STORM region, pressure gradient forces are calculated directly from the rawinsonde height data, a technique rarely used because height variations typically are not large enough to discern from errors in the reported data (Fankhauser, 1974). Height fields documenting the evolution of the mesolow will be shown, in addition to force balances occurring within the system.

6.1 Geopotential heights

The June 10-11 squall line, like several other mesoscale convective systems, was associated with a pronounced mid-level trough or mesolow (Sanders and Emanuel, 1977; Brown, 1979; Menard and Fritsch, 1989; Stumpf, 1989). This mesolow remained evident throughout the decaying stages of the June 10-11 system. It may have developed prior to the squall line initiation, as argued by Zhang *et al.* (1989). Sounding data prior to this budget study indicate its presence at 0130 UTC with a possible closed mesolow near Pratt, KS. Analyses at earlier times are more difficult since the feature had not entered the mesonetwork.

The mesolow can be seen at 700 mb (Fig. 6.1), just below the level of its maximum intensity, with the center of lowest heights found within the stratiform region, approximately 100 km behind the leading edge of the radar echo and about 75 km ahead of the back edge

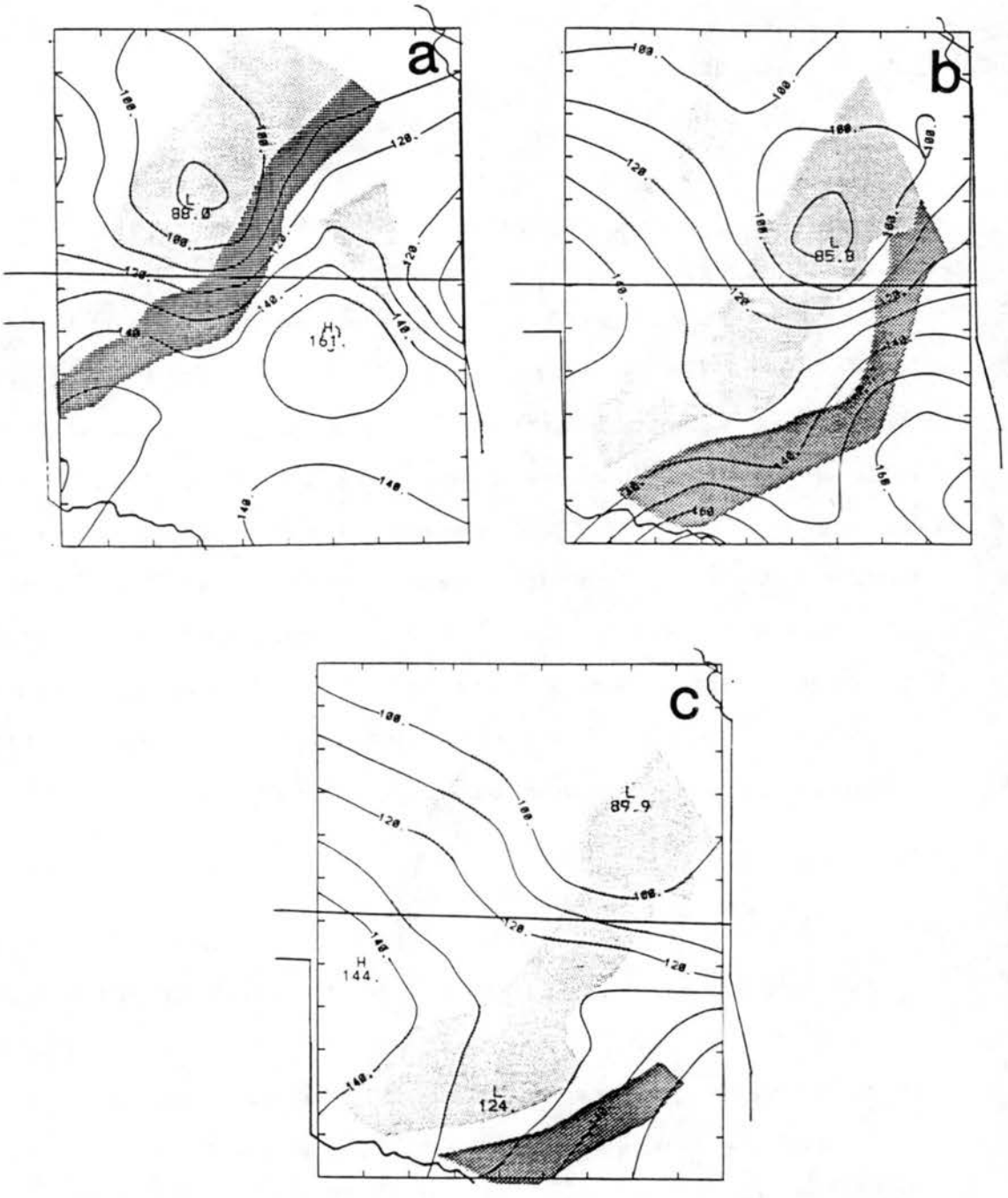

Figure 6.1: Geopotential height field at 700 mb for a.) 0300 UTC, b.) 0600 UTC, and c.) 0730 UTC. Heights are expressed in meters above 3000 m. Composited radar echoes are overlaid as explained in Fig. 4.7.

of the echo at 0300 and 0600 UTC. By 0730 UTC, the center of lowest heights had moved to the back edge of the radar echo. As stated earlier in Chapter 2, the heights used in this budget study were calculated hydrostatically without taking liquid water loading into account. At midlevels, in regions of intense convection, liquid water loading can decrease heights by 10 or 20 m (Sanders and Emanuel, 1977). Non-hydrostatic effects can also influence the heights in regions of intense dynamics. In the stratiform region, the liquid water mixing ratios estimated from the radar reflectivities appeared to be small so that heights would not be affected more than a few meters from liquid water-loading effects. We believe non-hydrostatic effects would also be small and thus the mesolow would be a real feature, fairly accurately depicted by our analyses.

The schematic of a squall line system, shown in Fig. 1.1 (Houze *et al.*, 1989), depicts a mesolow to lie at mid-levels within the stratiform region. Matejka (1989), using Doppler wind data to solve momentum equations for the height perturbations in this squall line at roughly 0400 UTC, found the mid-level mesolow to lie well inside the back edge of the radar echo. The rawinsonde heights therefore appear to agree with his results. The lowest heights within the PRE-STORM region, found toward the northern end of the squall line system, remained relatively constant over time within this mesolow, with the minimum value of 3086 m occurring at 0600 UTC. A height gradient of roughly 70 m over a distance of 150-200 km can be seen at 0300 and 0600 UTC. As heights in general fell over the region with time, the closed mesolow disappeared by 0730 UTC, but a distinct pressure trough could still be found. This mesolow within the stratiform region is hydrostatically-induced (Brown, 1979), the result of latent heat release aloft within the stratiform region anvil cloud above evaporative cooling and melting (Leary and Houze, 1979) taking place within the stratiform rain below cloud base.

A distinct and separate, yet also hydrostatically-induced low has been found near the rear of the convective line portion of a squall system by LeMone (1983) for a GATE system, and this pressure minimum was found to occur immediately under warm convective updrafts. Both mesolows have been discussed by Smull and Houze (1987) and are depicted in the squall line schematic from Houze *et al.* (1989), shown earlier (Fig. 1.1).

The convective line mesolow is too small to resolve with the rawinsonde height data used in this study. The stratiform mesolow is felt to be a distinctly-resolved feature and not an artifact due to aliasing of the convective line mesolow into the stratiform region since soundings were not positioned to capture the convective line mesolow.

The perturbation pressure minimum appeared to intensify only slightly above 700 mb, with its maximum intensity found somewhere between 575 and 675 mb. Houze *et al.* (1989) show in their squall line schematic (Fig. 1.1) that this mesolow is centered at or just above the melting level. Smull and Augustine (1989) detected a maximum amplitude of the low in the June 3-4 PRE-STORM MCS also above melting level, around 550 mb. Brown (1979), however, found the mid-level mesolow to be of maximum intensity just below the melting level, but his model simulation did not include ice microphysics. The melting level during the June 10-11 case was typically within 20 mb or so of 620 mb, so that the mesolow was indeed a maximum near the melting level. An examination of grid point height data shows that the mesolow at 0300 UTC was strongest at 575 mb, but was most intense at 0600 and 0730 UTC at 650 mb. The differences may be due to the termination of the rawinsonde nearest the mesolow at 650 mb at 0600 UTC. It is likely that had the rawinsonde nearest the mesolow continued to report data at higher levels, the level of peak mesolow intensity at 0600 and 0730 UTC would also have been slightly higher, perhaps remaining at 575 mb.

Above this level the mesolow weakened and at 500 mb, the height fields associated with this squall line were rather smooth, and seemed unperturbed (figure not shown). However, at 300 mb (Fig. 6.2), a reversal was evident from the lower level height fields, with the most prominent feature now being a perturbation pressure maximum over the southern end of the squall line. This pressure maximum can be seen at 0300 UTC, but intensifies dramatically by 0600 UTC. The anomalously high heights relative to surrounding regions at both 0600 and 0730 UTC were due to the ascent of one rawinsonde in an updraft core. Because most other rawinsondes within the squall line had terminated below this level, the data were smoothed over a large region, and do not present a completely accurate picture of the mesoscale height field. However, since high heights also appear as early as

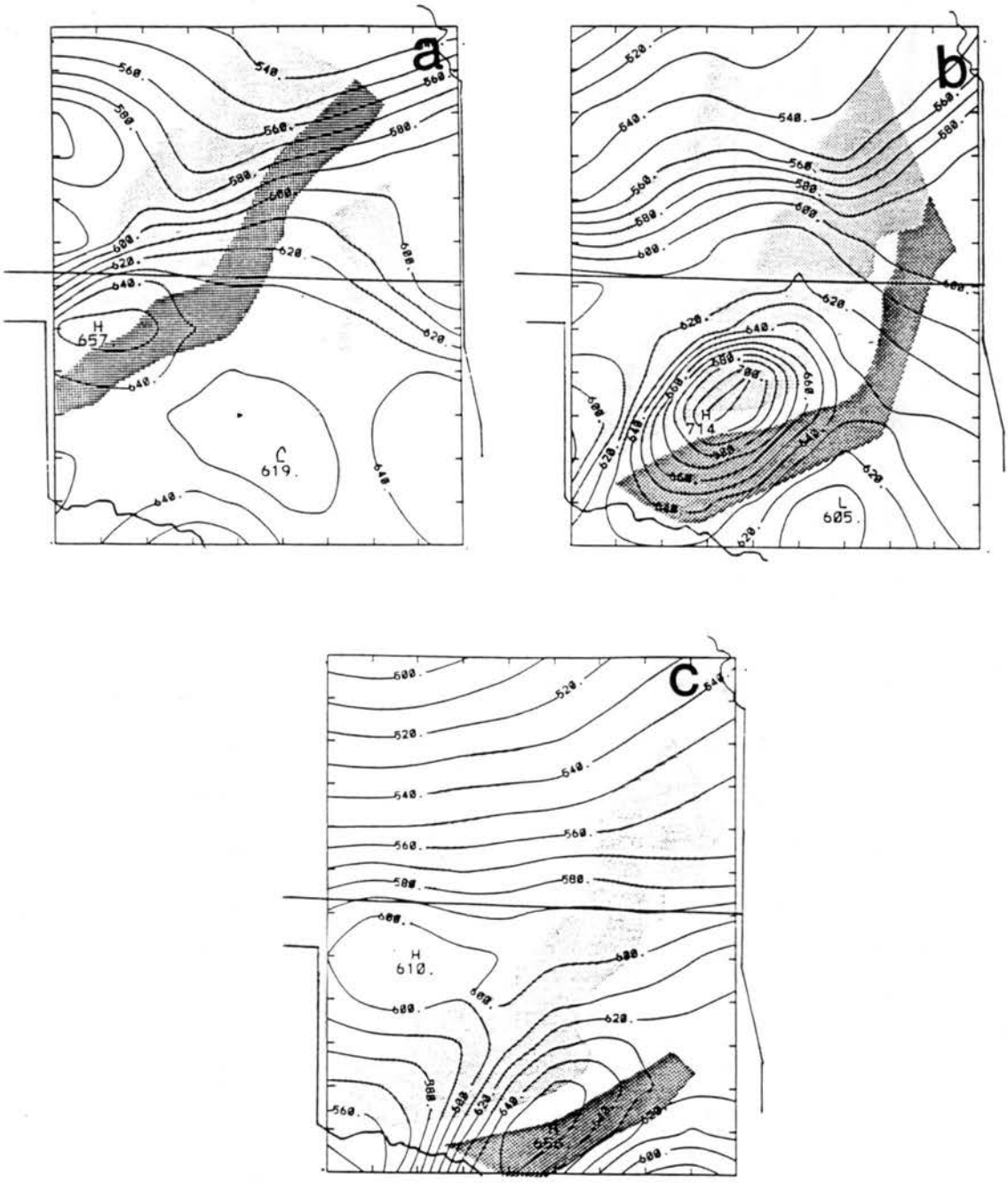

Figure 6.2: As in Fig. 6.1 except for 300 mb. Heights are in meters above 9000 m.

0300 UTC, the result of data from different rawinsondes, and strong divergence was found in the wind fields at high levels over the convective system, it is likely that this system did have an upper-level mesohigh associated with it, although not as intense as shown. Gao *et al.* (1989) found in a numerical simulation of this case that a weak mesohigh did exist at upper levels. Such a mesohigh appears in the squall line schematic (Fig. 1.1). (See Maddox *et al.*, 1981; Wetzel *et al.*, 1983; Menard and Fritsch, 1989, for similar features in other MCSs.) It is likely that the data at such a high level were too scarce in this case to accurately depict the mesohigh.

Vertical cross-sections detailing the height perturbations within the system can be seen in Fig. 6.3. Because height data in the "undisturbed" environment outside the system were not readily available at these times on June 11, the perturbation heights shown are the differences from latitudinal averages across the PRE-STORM region at each level. At all three budget times, a region of low heights can be seen just behind the convective line region, extending rearward to high levels. The tilt of the mesolow may suggest that a bit of the lower convective-line mesolow (Houze *et al.*, 1989) was being captured, although its scale is so small that it is unlikely more than one rawinsonde would have detected it. On these vertical cross-sections which involve averages taken over 50 km strips, the mid-level mesolow appears most intense between 600 and 700 mb, and has heights typically 20 m or so less than those outside of the squall line. At this level, a 20 m difference would correspond to almost 2 mb.

The vertical structure of height perturbations found from the rawinsonde data within this squall system agree with those found in a model study by Zhang and Gao (1989; their Fig. 3). They found the mid-level mesolow to be most intense at or just below 600 mb from 0300 through 0700 UTC. Behind it, and in front of it were regions of positive height perturbations, with maximum intensity at roughly the same level as that of the mesolow. These mesohighs also appear in the rawinsonde height fields shown in Fig. 6.3. The difference in heights between the mid-level mesohigh and mesolow in the model study was generally 40 - 50 m, somewhat more than the 20 - 25 m difference found from the rawinsonde data in Fig. 6.3. The rawinsonde data, however, was averaged over 50 km

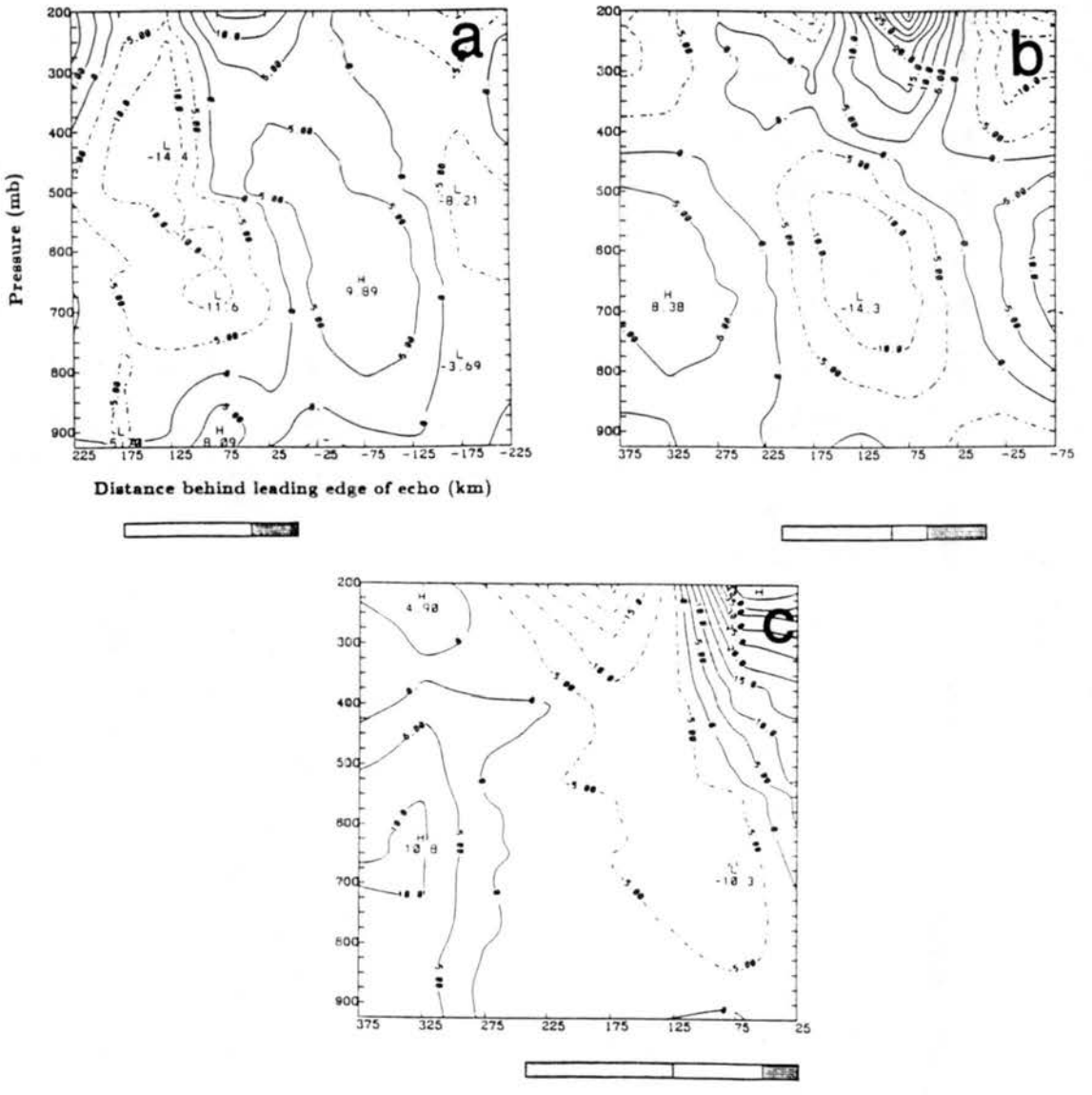

Figure 6.3: Vertical cross-sections of height perturbation (in meters) from latitude-average within PRE-STORM region for a.) 0300 UTC, b.) 0600 UTC, and c.) 0730 UTC.

wide strips, which would account for the diminished amplitude of the mesoscale high and low. Zhang and Gao also found an intense mesohigh over the system, typically in the 100 - 400 mb layer, but the feature was occasionally displaced to the rear of the strongest convective line updrafts.

The cross-sections shown extend down to 925 mb, and therefore, only the upper part of the surface mesohigh can be seen (primarily at 0300 UTC). The surface pressure features with this system, consisting of a mesohigh, and both a pre-squall and wake low, have been documented by Johnson and Hamilton (1988). The influence of the rawinsonde that ascended in an updraft core can be seen at high levels over the convective line at 0600 and 0730 UTC. Although the magnitudes of the perturbations over the system at levels above roughly 400 mb are definitely too large, qualitatively the perturbation field is correct and agrees with observations of strong divergence aloft.

6.2 Force balances

Equation (2.12) expresses the balance between forces affecting the component of the horizontal velocity normal to the squall line. Figures 6.4-6.7 detail the variation of these forces (per unit mass), or accelerations, in the vertical across the squall line. The total acceleration of the wind component normal to the line is a function of the pressure gradient, coriolis force, and small-scale forces (friction, turbulent stresses) that cannot be resolved by an analysis such as this. Figure 6.4 presents the horizontal pressure gradient force. The most prominent feature is the large region near the front of the system, extending throughout the troposphere, of acceleration from front to rear. Excluding high levels where the updraft-core sounding had an influence, peak front-to-rear accelerations reached 10 $m\ s^{-1}h^{-1}$. Near the rear of the system, some acceleration can be seen from rear-to-front, and it occured in the area of the rear-inflow jet. Peak accelerations exceeding 3 $m\ s^{-1}h^{-1}$ were found at 0300 and 0600 UTC, but the area covered by rear-to-front acceleration was largest at 0730 UTC, when the system was decaying rapidly. The large region influenced by rear-to-front pressure gradient acceleration at 0730 UTC may account for the persistent strength of the rear-inflow jet at this time, in spite of the fact the

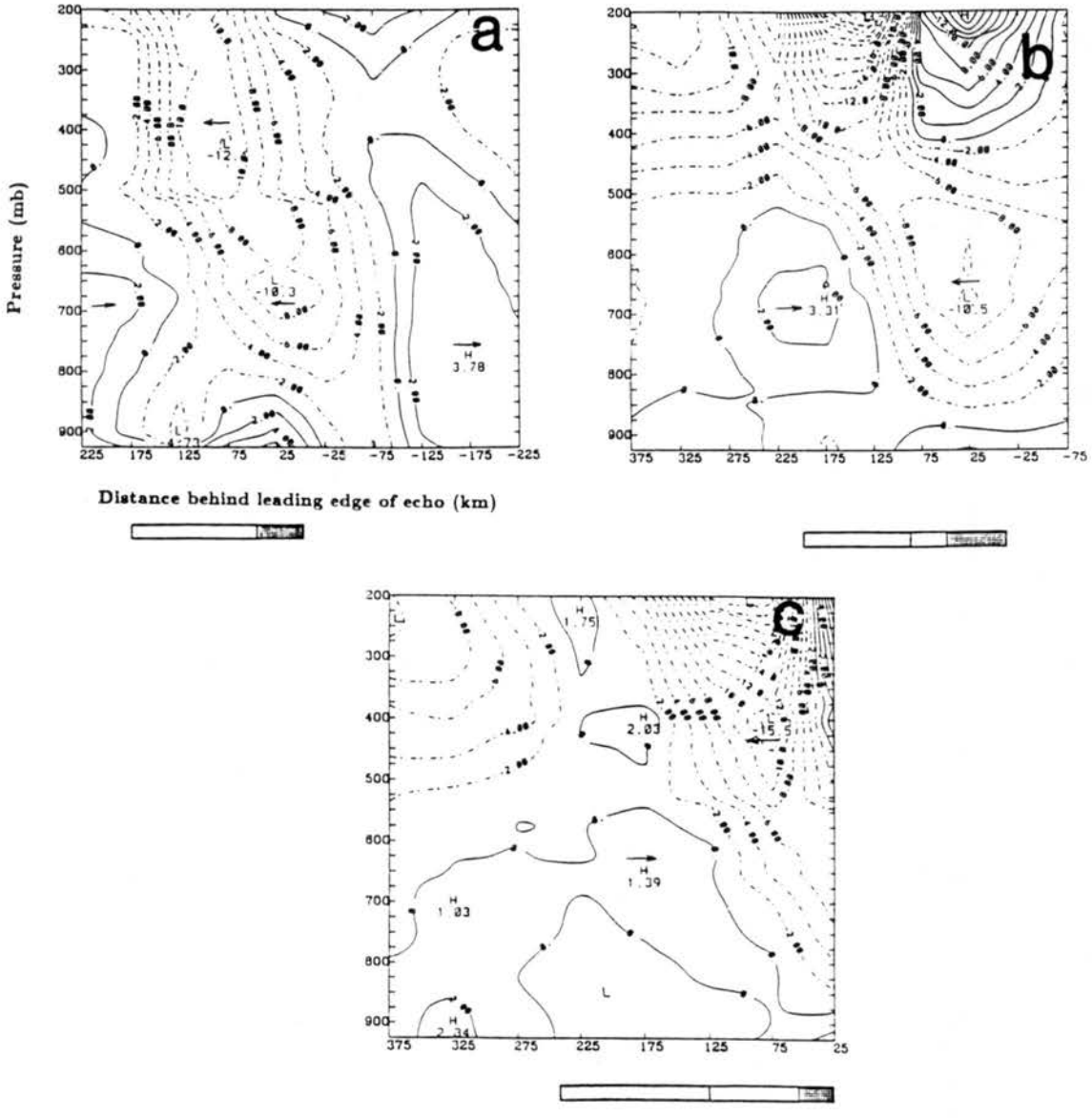

Figure 6.4: Vertical cross-sections of component of pressure gradient acceleration normal to the squall line (in $m\ s^{-1}h^{-1}$) computed from the rawinsonde height data at a.) 0300 UTC, b.) 0600 UTC, and c.) 0730 UTC. Positive values indicate acceleration from rear to front (left to right).

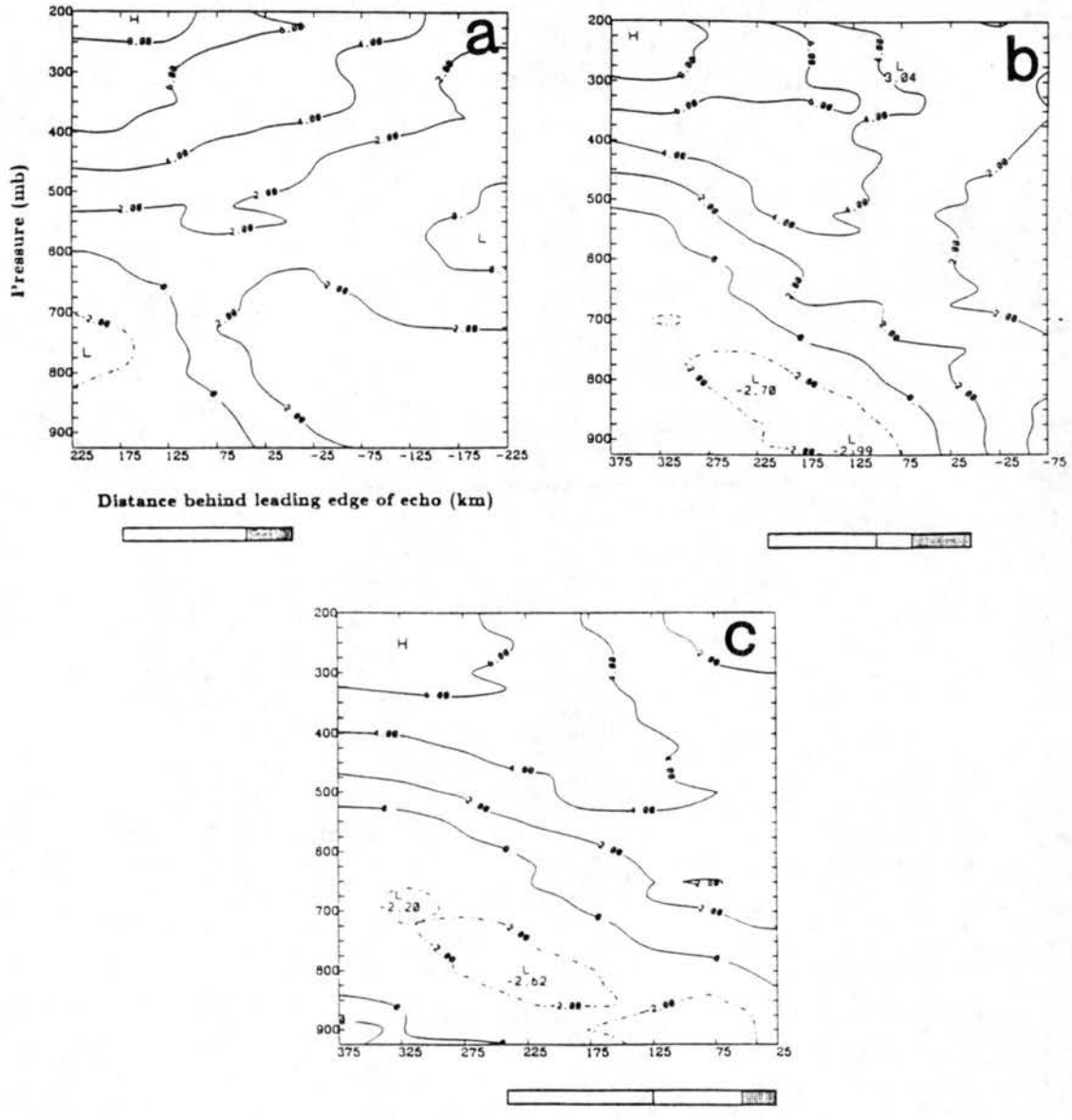

Figure 6.5: Same as Fig. 6.4, except for the component of coriolis force normal to the squall line.

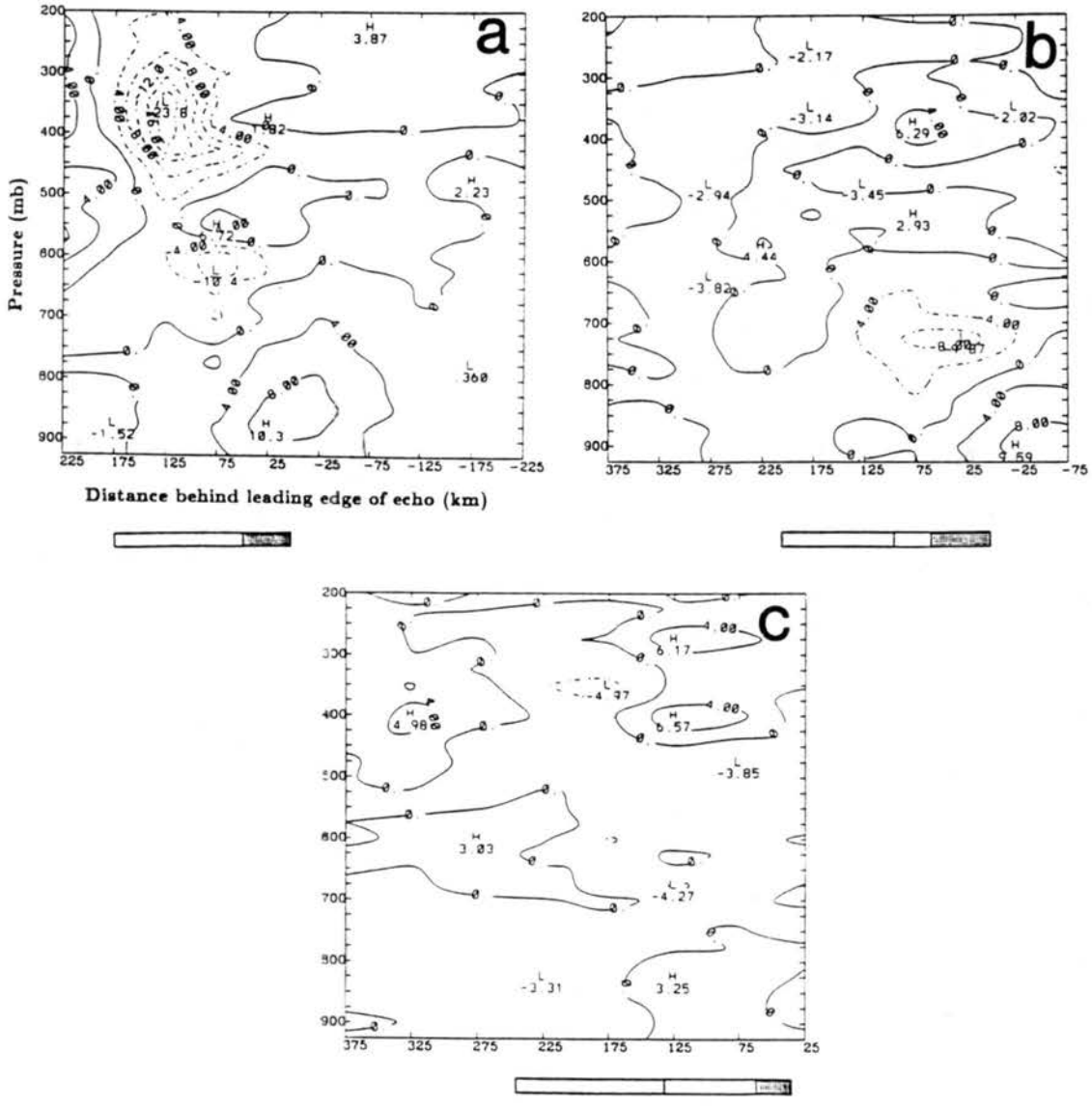

Figure 6.6: Same as Fig. 6.4, except for the observed acceleration of the velocity component normal to the squall line.

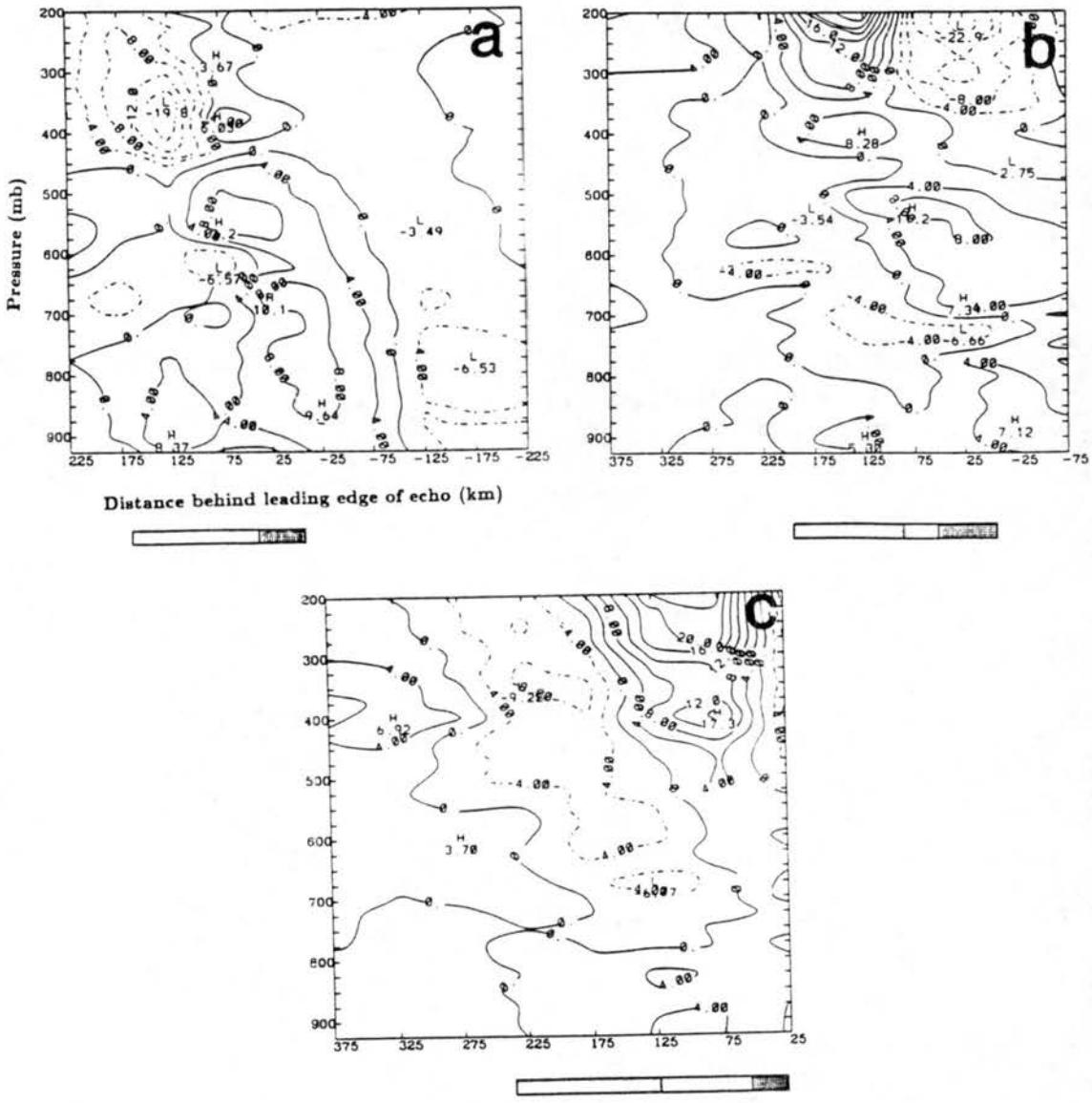

Figure 6.7: Same as Fig. 6.4, except for the residual term, $\overline{X}$, representing turbulent stresses.

system was decaying rapidly. Gao *et al.* (1989) have found in their model simulation of this system that the pressure gradient, or generation term, was the most important term contributing to both the rear-to-front acceleration that sustained the rear-inflow jet, and also the ascending front-to-rear jet ahead of it.

Near the surface, some evidence of accelerations within the mesohigh can be seen within the system, especially at 0300 UTC which was close to the time of maximum strength of the high. Gao *et al.* have linked both the region of strong rear-to-front acceleration near the surface at 0300 UTC and the rear-to-front acceleration at mid-levels further to the rear at the back of the system with the expansion of the rear-inflow jet during the mature stage of this system. Their model simulation found rear-to-front accelerations due to the pressure gradient of over 25 $m\ s^{-1}h^{-1}$ at the surface at 0300 UTC. The pressure gradient acceleration field at high levels at 0600 and 0730 UTC again was adversely affected by the one anomalous sounding, but qualitatively is correct. Although no rear-to-front outflow was found ahead of the system at high levels (Fig. 4.2) (agreeing with the observed lack of an extensive forward anvil), the front-to-rear flow around 250 mb decreased significantly between 0300 and 0600 UTC, which may be evidence that some rear-to-front pressure gradient acceleration (or deceleration of the front-to-rear flow) was occurring nonetheless, as shown in Fig. 6.4b.

The acceleration caused by the Coriolis force was generally in a rear-to-front direction, except at low levels within the stratiform region and to the rear of the system (Fig. 6.5). This was evidence of a northerly flow at low levels and the turning of the wind from a more northwesterly direction to southwesterly at mid-to-upper levels moving from west to east across the PRE-STORM domain (Johnson and Hamilton, 1988). The magnitudes of this acceleration were rather small but increased gradually to values as large as 6 or 8 $m\ s^{-1}h^{-1}$ at high levels. The Coriolis acceleration generally opposed the acceleration due to the pressure gradient, a result also found by Stevens (1979) for a GATE case. As found in LeMone (1983), this acceleration therefore diminished, rather than reinforced the U-vertical velocity circulation discussed in Newton (1950). Newton proposed that air at low levels, having excessive momentum, was accelerated to the right by the Coriolis

force while air at high levels, being subgeostrophic, had to be accelerated to the left of the gradient wind direction. The resulting circulation would increase rear-to-front flow at low levels, and front-to-rear flow aloft. This would have increased the U vertical shear for the June 10-11 case. However, whereas the pressure gradient acceleration on June 10-11 tended to increase the vertical shear of U at low levels in the convective line, and middle to high levels in the stratiform region, the Coriolis acceleration diminished it.

The total acceleration of the velocity component normal to the line (Fig. 6.6) was determined from gridded wind data, with the local derivative term being taken over the three hour time interval. It shows far more noise than the previous acceleration fields, because winds occasionally varied greatly in the vertical for soundings that ascended near the intense convection. Some layers of unreasonably large vertical wind shear (over 5 $m\ s^{-1}$ in 25 mb) were smoothed for this analysis, but small-scale maxima and minima are still apparent. Such variations of wind in the vertical may have been the real result of small-scale jets in the vicinity of convection, but are probably not representative of the large scale region over which the rawinsonde winds are smoothed. Ignoring these small-scale features, the general trend for the June 10-11 squall line was for decreasing accelerations, escpecially in the front-to-rear direction, over time. At high levels, rear-to-front acceleration began to replace front-to-rear acceleration. This may be interpreted as a decrease in front-to-rear flow at these levels as the system decayed . At 0300 UTC, rear-to-front acceleration was occurring below roughly 700 mb, with general front-to-rear acceleration above that level over the squall line. Another region of rear-to-front acceleration can be found near the back of the system, centered in the 400-600 mb layer. This rear-to-front acceleration can be interpreted as a strengthening of the rear-inflow jet at these levels around this time.

These accelerations are basically the result expected from the pressure gradients and Coriolis acceleration at this time, although the rear-to-front acceleration was occurring throughout a deeper layer and over a larger area at low levels than that for which the previous accelerations (Figs. 6.4 and 6.5) would account. The balance between the pressure gradient and Coriolis accelerations would appear to produce positive acceleration only

below 800 mb and only toward the front of the system. The front-to-rear acceleration aloft would agree with the pressure gradient.

At 0600 UTC, rear-to-front acceleration could still be found at low levels near the front of the system, with the front-to-rear acceleration aloft greatly diminished in strength since 0300 UTC. Also at 0600 UTC, an area at mid-levels near the back of the system was experiencing positive rear-to-front acceleration (or front-to-rear deceleration). This was associated with weakening front-to-rear flow within the lower parts of the anvil (roughly in the 400-600 mb layer), and some strengthening of the rear-inflow jet near the back of the system. Some weak front-to-rear acceleration was still occurring near the top of the anvil. By 0730 UTC, accelerations in general were weakening everywhere, and the strongest accelerations were in the rear-to-front direction. The rear-to-front acceleration found near the back edge of the echo at 0300 UTC continued to have its maximum intensity in this position near the rear of the system (with peak values near 400 and 600 mb) through 0730 UTC. This is consistent with a strengthening rear-inflow jet. Matejka (1989) studied the pressure and buoyancy forces with this squall system to isolate the evolutionary component of the forces. He found that although the pressure gradient force at high levels causing the front-to-rear acceleration there was not strong enough to prevent the weakening of the front-to-rear jet (the evolutionary pressure gradient was from rear-to-front), the gradients in mid-levels causing the rear-to-front acceleration were strong enough to maintain the rear-inflow jet. The observed accelerations from the rawinsonde data support his conclusions.

One area of front-to-rear acceleration was still occurring over the stratiform region at high levels in the anvil. The acceleration in this direction at this location was a persistent feature. Its weakening from $24m\ s^{-1}h^{-1}$ at 0300 UTC to less than $5\ m\ s^{-1}h^{-1}$ at 0600 and 0730 UTC agrees with the radar and satellite data showing an increasingly strong rate of decay at these times, and this supports the accuracy of wind measurements in this area.

The difference between the observed acceleration and the calculated rates from the pressure gradient and Coriolis forces is in indication not only of errors in the data, but

more importantly of small-scale forces that are not resolvable with the rawinsonde station spacing. Ignoring differences due to wind errors, and omission of water loading effects, this difference between the fields shown in Figs. 6.4 - 6.6 can be considered a measure of the internal turbulent stresses, $\overline{X}$, in the region (Fig. 6.7). At high levels (above 400 mb or so) at 0600 and 0730 UTC, unreasonably large values of $\overline{X}$ were due, in part, to the distorted height field resulting from the rawinsonde ascending in an updraft core. Some gravity waves may also have caused turbulence in the outflow layer. Turbulent forces should only be large in areas where vigorous convection is occurring (Sanders and Emanuel, 1977), and this is one check of the validity of solving for the turbulent stresses as a residual in the momentum budget. Fig. 6.7 shows that at 0300 UTC, when the system was most intense, turbulent stresses did indeed have much weaker magnitudes and far less variation over short distances outside the system than within it. As the system weakened (0600 and 0730 UTC), the difference between the stresses within it and outside were less, but the magnitudes outside of the squall line were still somewhat less than those within it. At 0300 UTC, when the observed accelerations were strong, the turbulent stress field (Fig. 6.7) resembled the vertical cross-section of acceleration (Fig. 6.6) because the pressure gradient force (Fig. 6.4) and the Coriolis force (Fig. 6.5) tended to oppose each other in most areas. At the later times when the observed accelerations were weak, the turbulent stress field was similar to that of the pressure gradient, except that the stresses were directed in opposite directions to the pressure gradient. Within the stratiform region, $\overline{X}$ was primarily positive at lower levels, and negative aloft (most evident at 0300 UTC; Fig. 6.7a). It also was negative, or in the front-to-rear direction, in the vicinity of the rear-inflow jet.

The internal turbulent stresses are primarily due to the correlation of u' and ω', which tends to be much larger than the correlation of u' and v' (Sanders and Emanuel, 1977; LeMone, 1983), and therefore

$$\overline{X} \approx -\frac{\partial \overline{(u'\omega')}}{\partial p}.$$

This explains the positive values of $\overline{X}$ at most low-level locations (Fig. 6.7) where ascent or descent is occurring across the axis of highest U. The term $\overline{(u'\omega')}$ changes sign within a vertical column when an updraft or downdraft crosses the axis of a jet. This situation occured in the convective line updraft below 750 mb, where the axis of relatively high (less negative, or slightly positive) U within the rear-inflow jet was crossed (See Fig. 4.2). Near the most intense part of the rear- inflow jet, the turbulent forces were resulting in front-to-rear acceleration, exceeding 5 $m\ s^{-1}h^{-1}$. A similar maximum in front-to-rear acceleration from turbulent forces was found in the study by Gao *et al.* (1989). This acceleration may be a result of turbulent mixing within the intense shear layer just above the axis of the jet. Evidence of such mixing has been reported as Kelvin-Helmholtz waves in the single-Doppler radar analyses of Houze *et al.* (1989). The effect of the jets on the turbulent stress field was most pronounced at 0600 UTC, when the vertical velocity patterns were still strong. The rear-inflow jet and front-to-rear jet each were associated with bands of strong turbulent stresses. Although the two jets were still strong at 0730 UTC, the vertical motion was becoming weak and the turbulent stress field did not have the pronounced bands. The magnitudes of the stresses were often as large or larger than those of the Coriolis acceleration or pressure gradient acceleration. This is a conclusion reached in nearly all previous momentum budget studies (Sanders and Emanuel, 1977; LeMone, 1983; Smull and Houze, 1987).

Rawinsonde wind data often contains errors, making accurate momentum budget calculations difficult. As stated above, both the acceleration and turbulent stress fields during the decaying stages of this system support the accuracy of the wind measurements used in this budget study. For instance, the accelerations and internal stresses tended to be small and the fields smooth outside of the convective system. Likewise, both fields showed decreasing amplitude as the system decayed, and general temporal continuity between the locations of extrema.

Earlier momentum budget studies have dealt primarily with the balance of forces within the convective line regions of mesoscale convective systems. Fig. 6.8 shows vertical profiles of the different accelerations taking place within the June 10-11 squall system's

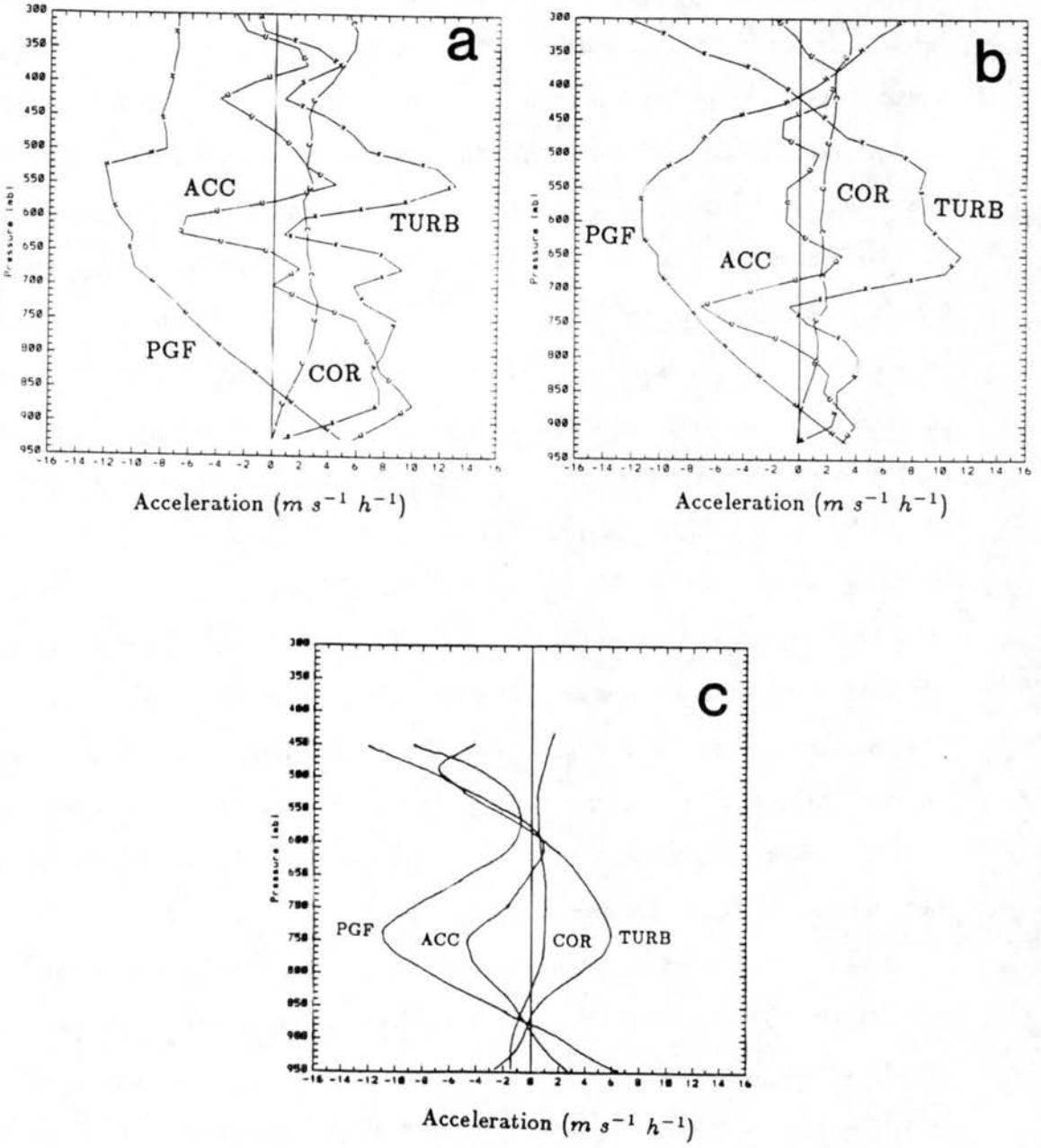

Figure 6.8: Vertical profiles of accelerations averaged over the convective line regions of this case at a.) 0300 UTC, and b.) 0600 UTC, and c.) for the Oklahoma squall line studied by Sanders and Emanuel (1977). Pressure gradient acceleration shown by curve H, coriolis acceleration, curve C, total acceleration, curve U and turbulent stresses, curve X. All units are $m\ s^{-1}h^{-1}$.

convective line region at 0300 and 0600 UTC, and compares them with the results of Sanders and Emanuel (1977), who were among the first to try to estimate the four forces shown in the figure. In the heat and moisture budgets, the inability of the rawinsondes to resolve the convective-scale processes limited the accuracy of the results found within the convective line region (magnitudes of the heating and drying rates were diminished). In the momentum budget, heights are also susceptible to problems caused by the inability of rawinsondes to resolve small-scale variations within the convective line region. In addition, liquid water loading and non-hydrostatic effects can play an important role in producing pressure perturbations there. Problems in accurately estimating the heights have limited the number of momentum budget studies done in the past. Although, errors do exist in the convective line portion of this momentum budget because of the problems mentioned above, the same problems are common to earlier studies, so that a relative comparison between the studies can still be made for the convective line region of the system.

Sanders and Emanuel used actual balloon measurements to calculate the internal turbulent stresses within their squall line, and solved for the pressure gradient as a residual (Fig. 6.8c). In general, they found that these pressure gradients were similar to those calculated from the reported rawinsonde heights, except at high levels (above 600 mb). They estimated liquid water loading from the difference between the height fields calculated using the two different methods. For this budget study, the pressure gradients were calculated from the rawinsonde height data (neglecting water loading effects), and the turbulent stresses were solved for as a residual (Figs. 6.8a and b.). At both 0300 (Fig. 6.8a) and 0600 UTC (Fig. 6.8b), the pressure gradient and Coriolis accelerations appear as rather smooth curves. The pressure gradient force at 0300 UTC was directed toward the rear, except below 850 mb. At 0600 UTC, the curve was similar, with the exception of some rear-to-front acceleration above 450 mb. This high-level rear-to-front acceleration was a result of the updraft-core ascent of the one sounding, and therefore may not actually represent the average acceleration from the pressure gradient at this level. Sanders and Emanuel found a similar vertical profile for the pressure gradient force in their case (Fig. 6.8c). The peak magnitudes were remarkably similar between the cases, 12 $m\ s^{-1}h^{-1}$,

and were found in mid-levels, with the PRE-STORM case having peak levels about 150 mb higher than that found by Sanders and Emanuel. The Coriolis force at 0300 and 0600 UTC on June 11 was entirely from rear-to-front, with a gradual increase with height. Sanders and Emanuel found weak front-to-rear acceleration with this force below 825 mb, but in general, rear-to-front acceleration, nearly constant with height.

The balance between the pressure gradient and Coriolis forces at 0300 UTC would result in acceleration toward the front of the system below 825 mb, and rearward acceleration everywhere above that level. The actual acceleration was strictly toward the front up to 650 mb, and then was quite variable above that level because of several layers of strong vertical shear. Because of the observed acceleration profile, it appears that the actual accelerations at this time were strongly influenced by the internal turbulent stresses. Between 650 and 825 mb, these turbulent stresses helped to cause the acceleration to be opposite the pressure gradient. The deceleration of the front-to-rear flow at lower levels agrees with the observed rapid decay of the squall line system.

The balance between the pressure gradient and Coriolis forces at 0600 UTC would also result in front-to-rear acceleration everywhere except at low levels below 875 mb, and high levels above 450 mb. The observed acceleration, much weaker than that at 0300 UTC, was toward the front below 775 mb, and rather variable and weak above that level. Again, it appears that internal stresses, caused mainly by mixing with the rear-inflow jet, were important in decelerating the front-to-rear flow in this part of the MCS. Except for a layer around 725 mb which may have been strongly influenced by the intrusion of the rear-inflow jet into the convective line region, the turbulent stresses produced an acceleration from rear-to-front everywhere below 425 mb.

In spite of the different methods used to calculate the turbulent stress and pressure gradient terms, similarity can be seen between the June 10-11 case and that of Sanders and Emanuel. The dominating acceleration toward the rear was that of the pressure gradient, while the primary opposing acceleration was that due to internal turbulent stresses. Although the Coriolis force also opposed the pressure gradient, it was typically much weaker than the internal turbulent stresses (also found in LeMone, 1983). The biggest difference

between the two squall lines is found in the observed accelerations. Sanders and Emanuel found mid-level front-to-rear acceleration dominating the vertical profile. On June 11, front-to-rear acceleration tended to be weaker, with strong acceleration in this direction restricted to only a narrow layer in mid-levels. Rear-to-front acceleration appeared to dominate the convective line region more than in the Sanders and Emanuel case. This may be a reflection of the decaying state of the June 10-11 squall line. The squall line studied by Sanders and Emanuel was at an earlier stage in its life cycle, when acceleration toward the rear at mid-levels would be likely.

Vertical profiles of the four forces averaged over the stratiform region at 0300, 0600 and 0730 UTC are shown in Fig. 6.9. In general, the acceleration from the pressure gradient was toward the rear at all levels within the stratiform rain region. A minimum in this acceleration, with near zero values, can be found centered in the 700-750 mb layer (especially at 0600 and 0730 UTC). This was the approximate level where rear-to-front acceleration could be found in the vicinity of the rear-inflow jet (Fig. 6.4). Because the vertical profiles were averaged over the entire stratiform region, positive rear-to-front acceleration in some areas was negated by weak front-to-rear acceleration nearby. The Coriolis force typically produced acceleration toward the rear in the lowest few kilometers (the layer deepened with time), and toward the front aloft. The balance between these two forces should have produced front-to-rear acceleration at nearly all levels, although it would have been weak everywhere with the exception of the lowest and highest levels. One exception was at 0600 and 0730 UTC (Figs. 6.9b and c), when the balance of these two forces was in the rear-to-front direction in a small layer near 700 mb.

The observed acceleration at 0300 UTC (Fig. 6.9a) was weak and toward the front below 725 mb, and generally toward the rear above that with a few exceptions. The strong rearward acceleration at high levels helped to transport hydrometeors rearward, and resulted in the substantial broadening of the stratiform region around this time. The observed accelerations show that the internal turbulent stresses were important in the stratiform region as they were in the convective line. However, they were generally much weaker than in the convective line, since any convective activity in this region was fairly

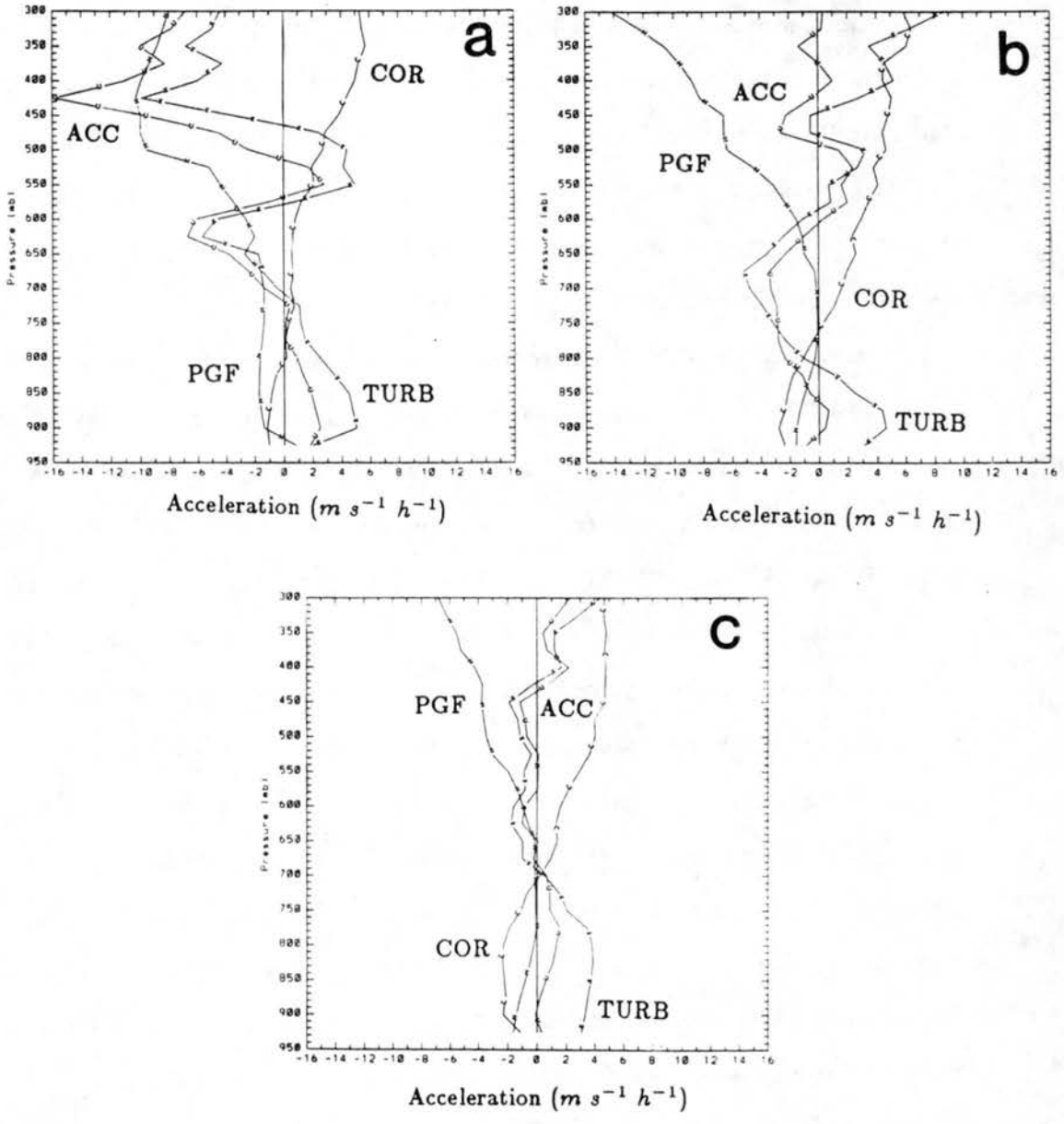

Figure 6.9: Vertical profiles of accelerations averaged over the stratiform region of the June 10-11 squall line at a.) 0300 UTC, b.) 0600 UTC, and c.) 0730 UTC. Pressure gradient acceleration shown by curve H, coriolis acceleration, curve C, total acceleration, curve U and turbulent stresses, curve X. Units are $m\ s^{-1}h^{-1}$.

weak, with stratiform cloud predominating. By 0600 UTC (Fig. 6.9b), the high-level rearward acceleration had almost disappeared, and accelerations in general were very weak, with the possible exception of the 650-800 mb layer. In that layer, averaged over the stratiform region, accelerations averaged 3 $m\ s^{-1}h^{-1}$ from front-to-rear, indicating a weakening of the portion of the rear-inflow jet within the stratiform region. In Fig. 6.6, it was shown that some rear-to-front accelerations were occurring at the back edge of the squall system. This area of positive acceleration was toward the rear of the area over which the average was taken for the stratiform region in Fig. 6.9. Again, the turbulent stresses had a significant impact on the actual acceleration, but the magnitudes were smaller than in the convective line region at this time. By 0730 UTC (Fig. 6.9c), acceleration everywhere below 350 mb was small, usually 1 $m\ s^{-1}h^{-1}$ or less, and was still toward the front of the line at low levels. At low levels, the balance between the Coriolis and pressure gradient forces was in the front-to-rear direction, so that the observed weak rea-to-front acceleration was probably due to turbulent forces. The balance between the Coriolis and pressure gradient forces elsewhere was nearly zero at this time, and the weak accelerations observed also were probably due primarily to weak turbulent stresses from the mixing of the different jets.

Figure 6.10 compares vertical profiles of the turbulent stress, or vertical divergence of the vertical momentum flux, within the convective line portion of this system at 0600 UTC, and squall lines studied by LeMone (1983), and Smull and Houze (1987). All three cases show positive acceleration (in the front-to-rear direction) at low levels, with opposite accelerations aloft. The midlatitude cases (curves B and C) have much larger magnitudes of internal stress than the tropical case (curve A). However, the profile of the tropical case (LeMone, 1983) is the one that most closely resembles the June 10-11 case at 0600 UTC. Positive acceleration due to the turbulent stresses was occurring everywhere below the 6-7 km layer, except for a small layer at 2.5 km. (That minimum in the positive acceleration for June 10-11 is related to the aliasing of the rear-inflow jet into the squall line at this level). The profile appears to qualitatively agree with the numerical study of this case by Gao *et al.* (1989). Peak positive values were found around 4 km. Because this was also

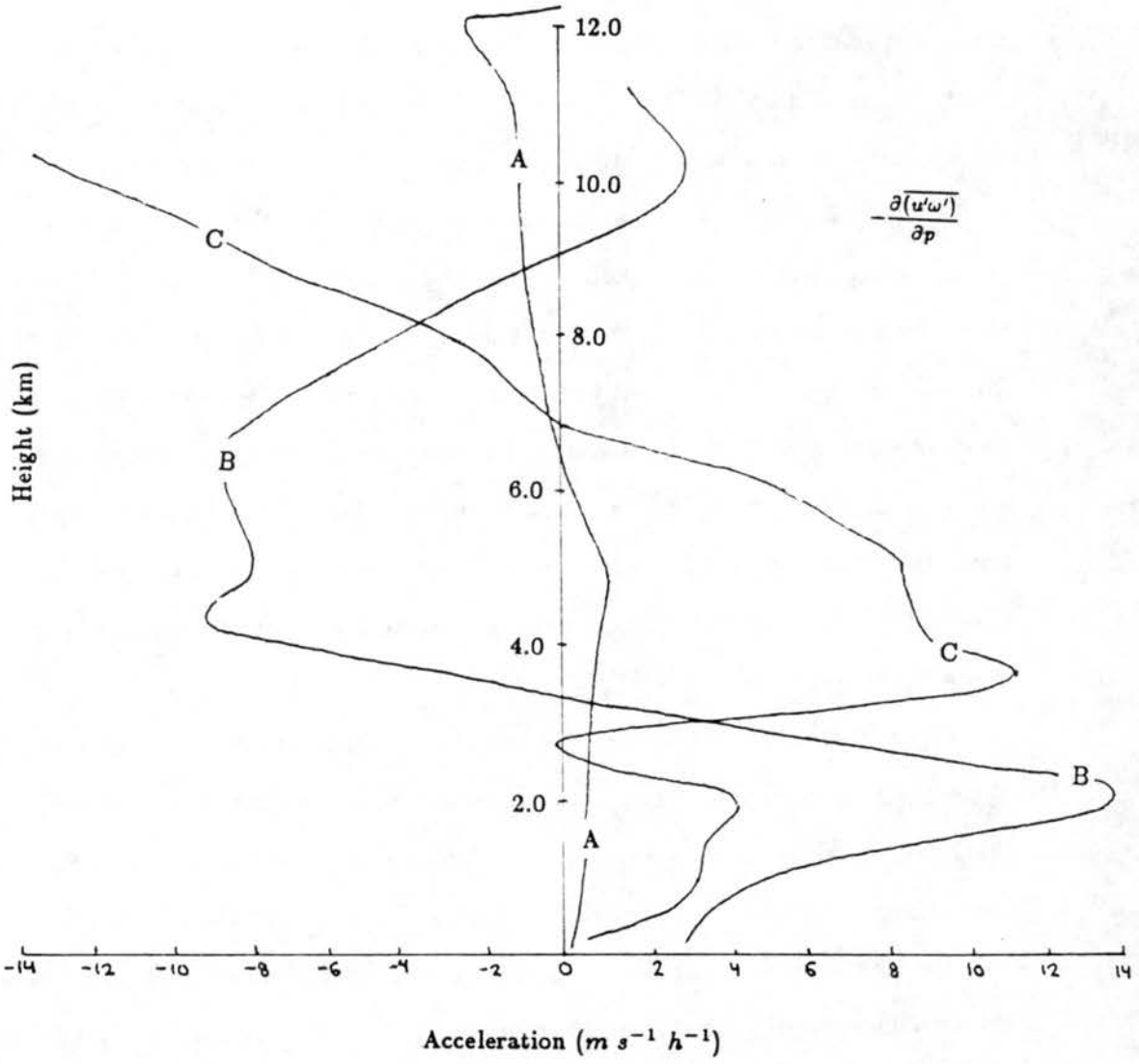

Figure 6.10: Comparison of vertical divergence of the vertical momentum flux (turbulent stresses) for several convective events. Curve A from LeMone (1983), B from Smull and Houze (1987), and C for the June 10-11 case at 0600 UTC. Units are $m\ s^{-1}h^{-1}$.

the level at which the front-to-rear flow was strongest at this time, it appears the vertical divergence of the vertical momentum flux was working to decrease the vertical shear at this late stage of the system. At this same time, however, the pressure gradient in the convective line was increasing the shear through most of the troposphere. At 0300 UTC, when the system was at its mature stage, both of these accelerations were increasing the vertical shear in different layers within the convective line.

The profile from Smull and Houze (1987) for another midlatitude squall line (curve B) is somewhat different in that the positive acceleration is found only below 3 km, and peak negative values are found in mid-levels where LeMone (1983) and this case found peak positive values. Smull and Houze also found a return to positive acceleration at high levels. Because they used Dual-Doppler radar data for their analysis, they were probably able to get a more precise picture of the events taking place strictly within the convective line, and their analysis was probably more immune to aliasing of stratiform region features into the convective line area. Some of the positive acceleration found in mid-levels for the June 10-11 case within the convective line may be due to aliasing of the effects of the strong rear-inflow jet which did extend to within 50 km or so of the leading edge of the echo. On the other hand, the June 10-11 case was in the decaying stages, and the rear-inflow jet had advanced farther forward than in the case studied by Smull and Houze which was in its mature stage. The differing profiles may be real, a sign of changes that take place within the convective line region leading to its dissipation.

Chapter 7

SUMMARY

This study used data from the dense rawinsonde network of the PRE-STORM project to perform heat, moisture, and momentum budgets on the June 10-11 PRE- STORM squall line during its late mature and decaying stages. Budget studies done on midlatitude convective systems have been uncommon in the past, and their similarity to tropical convective systems is still being learned. Many of the findings in this paper supported theories based on the discoveries from tropical budgets.

The June 10-11 squall line was shown to posses a pronounced flow structure made up of strong front-to-rear jets at high and low levels, and a rear-inflow jet at mid-levels. The rear-inflow jet remained strong as the convective system decayed, but the front-to-rear jets began to weaken. The rear-inflow jet was strongest in the vicinity of the echo notch, and was aligned toward the echo bow, as found in another case by Smull and Houze (1985). Strong convergence occurred over the stratiform region of the system where the opposing jets were in close proximity. Divergence was found to be strong within the falling rain of the stratiform region, and also at high levels above the system where it weakened markedly over time. Vertical velocities also decreased quickly as the system weakened, and the vertical axes of strongest ascent and descent tilted more with time, indicative of the broadening of the entire system. The mesoscale descent within the stratiform region began to weaken as the rainfall rates decreased, in spite of the fact that mid-level convergence remained relatively constant. This showed the importance of evaporative cooling in maintaining the downdraft. The splitting wake low at the surface found by Johnson and Hamilton (1988) was linked to two centers of maximum downward motion at the rear edge of the system. The enhanced downward motion would result in increased adiabatic warming, resulting in the pressure minimums.

The heat budget for this system showed warming in the front portion of the system, near the convective line, due to the release of latent heat from condensation, and cooling over the stratiform region at low levels, due to the evaporation of falling rain, and to a lesser extent, the melting of ice. The heating profile of the convective line resembled those of other midlatitude studies (Ninomiya, 1971; Lewis, 1975). Maximum values of the apparent heat source, Q_1 , were found at high levels, around 400 mb. The peak cooling rates were located at mid-levels, around 550 mb, at the back edge of the radar echo.

The moisture budget for this case indicated intense drying due to condensation within the convective line region, and moistening due to evaporation at low and middle levels in the stratiform rain area. The peak drying was found at lower levels than the peak heating, agreeing with other budget studies. Some hint of the double peak Q_2 structure found in other moisture budgets could be seen, in spite of the fact that aliasing of data due to the relatively coarse spacing of the rawinsonde sites was a problem. The double-peak structure has been explained as the result of two distinct processes, drying within cumulus clouds at low levels, and drying within the mesoscale anvil over the stratiform rain region (Johnson, 1984).

Precipitation rates estimated from the vertical integration of both the moisture and heat budgets showed the importance of considering storage effects when doing budget studies of decaying midlatitude convection. The typical underestimates due to the rawinsonde resolution occurred within the convective line regions. The budget-integrated predictions increasingly underestimated the stratiform region rain rates at 0600 and 0730 UTC when the system was decaying more rapidly. The discrepancy exceeded 2 $mm\ h^{-1}$ by 0730 UTC; however, the transport of hydrometeors into the region from the convective line portion of the system was shown to have the ability to add up to 2-4 $mm\ h^{-1}$ to the rain rates. The complete system-averaged rates also were underestimated as the system weakened, implying the importance of storage effects. Rainfall produced at earlier times when the convective system was more vigorous had been stored within the clouds and was falling out at these later times as the updrafts rapidly weakened.

Although the predicted rainfall rates were found to differ from the observed rates, in general the values were surprisingly close, supporting the credibility of the budgets.

The location of Q_1 and Q_2 extrema, and the predicted area covered by precipitation in the budget integrations agreed with the observed convective system location. Also, the temporal trend of the decaying system was illustrated well in the heat and moisture budgets. These factors support the ability to determine with a high degree of accuracy, the heat and moisture budgets of midlatitude convection from rawinsonde data.

Height fields for this case showed a strong mesolow at mid-levels within the stratiform region, in agreement with the results of Brown (1979). Heights were calculated hydrostatically without taking liquid water loading into account. It was felt that the effects of liquid water loading would not be significant within the stratiform region. Heights within the mesolow were several tens of meters deeper than in nearby regions, allowing the direct calculation of the pressure gradient force in the momentum budget study of the squall line. Accelerations of the component of the wind normal to the squall line became weak, and increasingly in the rear-to-front direction at high levels, as the system decayed. The observed acceleration was often in a direction opposite to that of the pressure gradient acceleration. Although the coriolis force was found to oppose the pressure gradient (as in Sanders and Emanuel, 1977), internal turbulent stresses tended to oppose the pressure gradient with much larger magnitudes, and had more influence on the observed acceleration. The force balance within the June 10-11 squall line was similar to the case studied by Sanders and Emanuel, except for the observed acceleration. Because the acceleration in their case was front-to-rear over a deep layer, it is believed that the switch to more rear-to-front acceleration may be a typical sign of decay in squall lines. At the earliest budget time in this study, 0300 UTC, when convection was still intense, accelerations were increasing the vertical shear over a deep layer within the convective line, a result found by LeMone (1983) for a tropical squall line. At later times, increasing shear was broken into small layers.

As with the heat and moisture budgets, a good deal of temporal continuity was found in the momentum budget as the system decayed. The decrease in the acceleration and turbulent stresses within the system as it decayed imply a high degree of reliability for the momentum budget.

Although the PRE-STORM project resulted in a much more dense rawinsonde network than normally available from NWS sites, the station spacing was still too coarse to resolve accurately most convective line region processes. Compositing of the soundings for this case decreased the station spacing to roughly 80 km, but the accurate determination of quantities like ω- vertical velocity, specific humidity, and temperature which are necessary to calculate heating and drying rates in the budgets for the convective line region require spacing on the order of 10 or 20 km to approach their true values. In addition, many of the rawinsondes terminated early (most within the 450 - 650 mb layer) inside the convective system, diminishing the accuracy of analyses at higher levels. These problems should be considered in the planning for future mesoscale field experiments such as STORM-Central.

Future budget study work should be done on this case, or other PRE-STORM cases, to document more fully the life cycle of a squall system, from birth to decay. More work needs to be done on investigating the development and strengthening of the rear-inflow jet found in this case and many similar ones. How much of its strength is related to the intensity of the mid-level mesolow caused by hydrostatic processes? Since heat and moisture budget studies from the PRE-STORM dataset have not been done before, the rawinsonde data should be used from other cases to determine if the Q_1 and Q_2 profiles found in this study are typical of most organized midlatitude squall lines. In addition, do the budget-integrated rainfall rates within the stratiform regions of dissipating systems always show a negative departure from the observed rates? Perhaps, more detailed work could be done using Doppler radar for this case to determine precisely how much of the discrepancy is due to the transport of hydrometeors rearward in the anvil.

REFERENCES

Arakawa, A., and J.-M. Chen, 1986: Closure assumptions in the cumulus parameterization problem. WMO/IUGG Symposium on Short- and Medium-Range Numerical Weather Prediction, Tokyo, 107-131.

Augustine, J. A., and E. J. Zipser, 1987: The use of wind profilers in a mesoscale experiment. *Bull. Amer. Meteor. Soc.*, **68**, 4-17.

Balsley, B. B., W. L. Ecklund, D. A. Carter, A. C. Riddle, and K. S. Gage, 1988: Average vertical motions in the tropical atmosphere observed by a radar wind profiler on Pohnpei (7° N latitude, 157° E longitude). *J. Atmos. Sci.*, **45**, 396-405.

Barnes, S. L., 1964: A technique for maximizing details in numerical weather map analysis. *J. Appl. Meteor.*, **3**, 396-409.

Barnes, S. L., 1973: Mesoscale objective map analysis using weighted time- series observations. NOAA Tech. Memo. ERL NSSL-62, Norman, OK, 60 pp.

Bluestein, H. B., and M. H. Jain, 1985: Formation of mesoscale lines of precipitation: Severe squall lines in Oklahoma during the spring. *J. Atmos. Sci.*, **42**, 1711-1731.

Bluestein, H. B., E. W. McCaul, Jr., and G. R. Woodall, 1988: Case study of a tornadic storm along the dryline in the Texas panhandle: The Canadian storm of 7 May 1986. *Preprints, 15th Conf. on Severe Local Storms*, Baltimore, Amer. Meteor. Soc., 217-220.

Brown, J. M., 1979: Mesoscale unsaturated downdrafts driven by rainfall evaporation: A numerical study. *J. Atmos. Sci.*, **36**, 313-338.

Chen, Y.-L., and E. J. Zipser, 1982: The role of horizontal advection of hydrometeors in the water budget of a large squall line system. *Preprints, 12th Conf. on Severe Local Storms*, San Antonio, Amer. Meteor Soc., 355-358.

Cheng, C.-P., and R. A. Houze, Jr., 1979: The distribution of convective and mesoscale precipitation in GATE radar echo patterns. *Mon. Wea. Rev.*, **107**, 1370-1381.

Cotton, W. R., M.-S. Lin, R. L. McAnelly, and C. J. Tremback, 1989: A composite model of mesoscale convective complexes. *Mon. Wea. Rev.*, **117**, 765-783.

Cunning, J. B., 1987: The Oklahoma-Kansas Preliminary Regional Experiment for STORM-Central. *Bull. Amer. Meteor. Soc.*, **67**, 1478-1486.

Davies-Jones, R. P., 1974: Discussion of measurements inside high-speed thunderstorm updrafts. *J. Appl. Meteor.*, **13**, 710-717.

Esbensen, S. K., J.-T. Wang, and E. I. Tollerud, 1988: A composite life cycle of nonsquall mesoscale convective systems over the tropical ocean. Part II: Heat and moisture budgets. *J. Atmos. Sci.*, **45**, 537-548.

Fankhauser, J. C., 1974: The derivation of consistent fields of wind and geopotential height from mesoscale rawinsonde data. *J. Appl. Meteor.*, **13**, 637-646.

Fritsch, J. M., 1975: Cumulus dynamics: Local compensating subsidence and its implication for cumulus parameterization. *Pure Appl. Geophys.*, **113**, 851- 867.

Fritsch, J. M., C. F. Chappell and L. R. Hoxit, 1976: The use of large-scale budgets for convective parameterization. *Mon. Wea. Rev.*, **104**, 1408-1418.

Fujita, T. T., 1955: Results of detailed synoptic studies of squall lines. *Tellus*, **7**, 405-436.

Gamache, J. F., and R. A. Houze, Jr., 1982: Mesoscale air motions associated with a tropical squall line. *Mon. Wea. Rev.*, **110**, 118-135.

Gamache, J. F., and R. A. Houze, Jr., 1983: Water budget of a mesoscale convective system in the tropics. *J. Atmos. Sci.*, **40**, 1835-1850.

Gao, K., D.-L. Zhang, M. W. Moncrieff, and H.-R. Cho, 1989: Mesoscale momentum budget in a midlatitude squall line: A numerical case study. *Mon. Wea. Rev.*, **117**, (in press).

Houze, R. A., Jr., 1977: Structure and dynamics of a tropical squall-line system observed during GATE. *Mon. Wea. Rev.*, **105**, 1540-1567.

Houze, R. A., Jr., 1982: Cloud clusters and large-scale vertical motions in the tropics. *J. Meteor. Soc. Japan,* **60**, 396-410.

Houze, R. A., Jr., 1989: Observed structure of mesoscale convective systems and implications for large-scale heating. *Quart. J. Roy. Meteor. Soc.*, **115**, 425-461.

Houze, R. A., Jr., and A. K. Betts, 1981: Convection in GATE. *Reviews of Geophysics and Space Physics*, **19**, 541-576.

Houze, R. A., Jr., and P. V. Hobbs, 1982: Organization and structure of precipitating cloud systems. *Advances in Geophysics*, vol. 24, Academic Press, 225-315.

Houze, R. A., Jr., S. A. Rutledge, M. I. Biggerstaff, and B. F. Smull, 1989: Interpretation of Doppler weather radar displays of midlatitude mesoscale convective systems. *Bull. Amer. Meteor. Soc.*, **70**, 608-619.

Hoxit, L. R., C. F. Chappell, and J. M. Fritsch, 1976: Formation of mesolows or pressure troughs in advance of cumulonimbus clouds. *Mon. Wea. Rev.*, **104**, 1419-1428.

Johnson, R. H., 1976: The role of convective-scale precipitation downdrafts in cumulus and synoptic scale interactions. *J. Atmos. Sci.*, **33**, 1890-1910.

Johnson, R. H., 1980: Diagnosis of convective and mesoscale motions during Phase III of GATE. *J. Atmos. Sci.*, **37**, 733-753.

Johnson, R. H., 1982: Vertical motion in near-equatorial winter monsoon convection. *J. Meteor. Soc. Japan,* **60**, 682-690.

Johnson, R. H., and M. E. Nicholls, 1983: A composite analysis of the boundary layer accompanying a tropical squall line. *Mon. Wea. Rev.*, **111**, 308-319.

Johnson, R. H., 1984: Partitioning tropical heat and moisture budgets into cumulus and mesoscale components: Implications for cumulus parameterization. *Mon. Wea. Rev.*, **112**, 1590-1601.

Johnson, R. H., and G. S. Young, 1983: Heat and moisture budgets of tropical mesoscale anvil clouds. *J. Atmos. Sci.*, **40**, 2138-2147.

Johnson, R. H., and W. A. Gallus, 1988: The wake structure of an intense midlatitude squall line in OK PRE-STORM. *Preprints, 15th Conf. on Severe Local Storms*, Baltimore, Amer. Meteor. Soc., 229-232.

Johnson, R. H., and P. J. Hamilton, 1988: The relationship of surface pressure features to the precipitation and air flow structure of an intense midlatitude squall line. *Mon. Wea. Rev.*, **116**, 1444-1472.

Kuo, Y.-H., and R. A. Anthes, 1984: Mesoscale budgets of heat and moisture in a convective system over the Central United States. *Mon. Wea. Rev.*, **112**, 1482-1497.

Leary, C. A., and R. A. Houze, Jr., 1979: The structure and evolution of convection in a tropical cloud cluster. *J. Atmos. Sci.*, **36**, 437-457.

Leary, C. A., and R. A. Houze, Jr., 1980: The contribution of mesoscale motions to the mass and heat fluxes of an intense tropical convective system. *J. Atmos. Sci.*, **37**, 784-796.

LeMone, M. A., 1983: Momentum transport by a line of cumulonimbus. *J. Atmos. Sci.*, **40**, 1815-1834.

Lewis, J. M., 1975: Test of Ogura-Cho model on a prefrontal squall line case. *Mon. Wea. Rev.*, **103**, 764-778.

Luo, H., and M. Yanai, 1984: The large-scale circulation and heat sources over the Tibetan plateau and surrounding areas during the early summer of 1979. Part II: Heat and moisture budgets. *Mon. Wea. Rev.*, **112**, 966-989.

McNab, A. L., and A. K. Betts, 1978: A mesoscale budget study of cumulus convection. *Mon. Wea. Rev.*, **106**, 1317-1331.

Maddox R. A., D. J. Perkey, and J. M. Fritsch, 1981: Evolution of upper tropospheric features during the development of a mesoscale convective complex. *J. Atmos. Sci.*, **38**, 1664-1674.

Matejka, T., 1989: Pressure and buoyancy forces and tendencies in a squall line and their relation to its evolution. *Preprints, 24th Conf. on Radar Meteorology*, Amer. Meteor. Soc., Tallahassee, 478-481.

Meitín, J. G., and J. B. Cunning, 1985: The Oklahoma-Kansas preliminary regional experiment for STORM-Central (OK PRE-STORM), Volume I. Daily operations summary. NOAA Tech. Memo. ERL ESG-20, Dept. of Commerce, Weather Research Program, Boulder, Colorado, 313 pp.

Menard, R. D., and J. M. Fritsch, 1989: A mesoscale convective complex- generated inertially stable warm core vortex. *Mon. Wea. Rev.*, **117**, 1237-1261.

Menard, R. D., D. L. Sims, and J. M. Fritsch, 1988: Case example of the effect of a wake low on subsequent convective events. *Preprints, 15th Conf. on Severe Local Storms*, Amer. Meteor. Soc., Baltimore, 225-228.

Newton, C. W., 1950: Structure and mechanisms of the pre-frontal squall line. *J. Meteor.*, **7**, 210-222.

Ninomiya, K., 1971: Dynamical analysis of outflow from tornado-producing thunderstorms as revealed by ATS III pictures. *J. Appl. Meteor.*, **10**, 145-167.

Nitta, T., 1972: Energy budget of wave disturbances over the Marshall Islands during the years of 1956 and 1958. *J. Meteor. Soc. Japan,* **50**, 71-84.

Nitta, T., 1977: Response of cumulus updrafts and downdrafts to GATE A/B-scale motion systems. *J. Atmos. Sci.*, **34**, 1163-1186.

O'Brien, J. J., 1970: Alternative solutions to the classical vertical velocity problem. *J. Appl. Meteor.*, **9**, 197-203.

Ogura, Y., and Y.-L. Chen, 1977: A life history of an intense mesoscale convective storm in Oklahoma. *J. Atmos. Sci.*, **34**, 1458-1476.

Ogura, Y., and M. T. Liou, 1980: The structure of a midlatitude squall line. *J. Atmos. Sci.*, **37**, 553-567.

Ooyama, K. V., 1982: Conceptual evolution of the theory and modeling of the tropical cyclone.*J. Meteor. Soc. Japan,* **60**, 369-379.

Riehl, H., and J. S. Malkus, 1958: On the heat balance in the equatorial trough zone. *Geophysica*, **6**, 503-538.

Rotunno, R., J. B. Klemp, and M. L. Weisman, 1988: A theory for strong, long-lived squall lines. *J. Atmos. Sci.*, **45**, 463-485.

Rutledge, S. A., and R. A. Houze, Jr., 1987: A diagnostic modeling study of the trailing stratiform region of a midlatitude squall line. *J. Atmos. Sci.*, **44**, 2640- 2656.

Rutledge, S. A., R. A. Houze, Jr., M. I. Biggerstaff and T. Matejka, 1988: The Oklahoma-Kansas mesoscale convective system of 10-11 June 1985: Precipitation structure and single-Doppler radar analysis. *Mon. Wea. Rev.*, **116**, 1409-1430.

Rutledge, S. A., and D. R. MacGorman, 1988: Cloud-to-ground lightning activity in the 10-11 June 1985 mesoscale convective system observed during Oklahoma-Kansas PRE-STORM project. *Mon. Wea. Rev.*, **116**, 1393-1408.

Sanders, F., and R. J. Paine, 1975: The structure and thermodynamics of an intense mesoscale convective storm in Oklahoma. *J. Atmos. Sci.*, **32**, 1563-1579.

Sanders, F., and K. Emanuel, 1977: The momentum budget and temporal evolution of a mesoscale convective system. *J. Atmos. Sci.*, **34**, 322-330.

Smull, B. F., and R. A. Houze, Jr., 1985: A midlatitude squall line with a trailing region of stratiform rain: radar and satellite observations. *Mon. Wea. Rev.*, **113**, 117-133.

Smull, B. F., and R. A. Houze, Jr., 1987: Dual-Doppler radar analysis of a midlatitude squall line with a trailing region of stratiform rain. *J. Atmos. Sci.*, **44**, 2128-2148.

Smull, B. F., and R. A. Houze, Jr., 1987: Rear inflow in squall lines with trailing stratiform precipitation. *Mon. Wea. Rev.*, **115**, 2869-2889.

Smull, B. F., and J. A. Augustine, 1989: Structure and environment of a non-squall mesoscale convective comples observed during PRE-STORM. *24th Conf. on Radaj Meteorology*, Tallahassee, Florida, 502-505.

Srivastava, R. C., T. J. Matejka and T. J. Lorello, 1986: Doppler radar study of the trailing anvil region associated with a squall line. *J. Atmos. Sci.*, **43**, 356-377.

Stevens, D. E., 1979: Vorticity, momentum and divergence budgets of synoptic- scale wave disturbances in the tropical Eastern Atlantic. *Mon. Wea. Rev.*, **107**, 535-550.

Stumpf, G. J., 1988: Surface pressure features associated with a mesoscale convective system in O. K. PRE-STORM. M.S. Thesis, Colorado State University Dept. of Atmos. Sci., 148 pp.

Stumpf, G. J., and W. A. Gallus, Jr., 1989: An examination of new convective development with a PRE-STORM squall line case. *24th Conf. on Radar Meteorology*, Tallahassee, Florida, 506-509.

Thompson, R. M., Jr., S. W. Payne, E. E. Recker, and R. J. Reed, 1979: Structure and properties of synoptic-scale disturbances in the intertropical convergence zone of the eastern Atlantic. *J. Atmos. Sci.*, **36**, 53-72.

Vasiloff, S. V., and H. B. Bluestein, 1988: Analysis of the Oklahoma segment of the 10-11 June 1985 squall line: Maturity to decay. *15th Conf. on Severe Local Storms*, Baltimore, Maryland, 288-291.

Webster, P. J., and G. L. Stephens, 1980: Tropical upper-tropospheric extended clouds: Inferences from Winter MONEX. *J. Atmos. Sci.*, **37**, 1521-1541.

Wetzel, P. J., W. R. Cotton, and R. L. McAnelly, 1983: A long-lived mesoscale convective complex. *Mon. Wea. Rev.*, **111**, 1919-1937.

Yanai, M., S. Esbensen and J. Chu, 1973: Determination of bulk properties of tropical cloud clusters from large-scale heat and moisture budgets. *J. Atmos. Sci.*, **36**, 53-72.

Zhang, D.-L., and K. Gao, 1989: Numerical simulation of an intense squall line during 10-11 June 1985 PRE-STORM. Part II: Rear inflow, surface pressure perturbations and stratiform precipitation. *Mon. Wea. Rev.*, **117**, 2067-2094.

Zhang, D.-L., K. Gao and D. B. Parsons, 1989: Numerical simulation of an intense squall line during 10-11 June 1985 PRE-STORM. Part I: Model verification. *Mon. Wea. Rev.*, **117**, 960-994.

Zipser, E. J., 1977: Mesoscale and convective-scale downdrafts as distinct components of squall line structure. *Mon. Wea. Rev.*, **105**, 1568-1589.

Zwack, P., and C. Anderson, 1970: 25 July 1969: Showers and continuous precipitation. *Preprints, 14th Radar Meteor. Conf.*, Tucson, Amer. Meteor. Soc., 335-338.

Appendix A

ADDITION OF NEARLY-SATURATED BOGUS SOUNDINGS INTO CONVECTIVE LINE

As explained in Chapter 3, aliasing of pre-squall environment data into the convective line and vice-versa was common in the budget studies due to the 80 km spacing of the rawinsonde data used in objective analyses. The problem at 0300 and 0730 UTC was not as pronounced as it was at 0600 UTC when dry layers just in front of the squall line were smoothed into the convective line region. Because the wind data in this region near the eastern edge of the grid network indicated large upward vertical motion, the dry layers smoothed into the strong updrafts produced unusual values of the apparent moisture sink, Q_2 , in the moisture budget. Although it is possible that the dry layers were a real feature in front of the system, a result of subsidence from earlier convection, the low humidity values smoothed into the convective line were not real, and diminished the quality of the moisture budget at 0600 UTC.

In order to diminish the problem without taking too much liberty with the existing data, three bogus soundings were positioned at the front edge of the radar echo. They are marked by circles in Fig. 3.2b. These soundings were not assumed to be moist adiabatic, since none of the actual soundings near or within the convective line were moist adiabatic, and to make that assumption would result in anomalously large values of Q_2 . The sounding that best seemed to represent the state of the atmosphere within the convective line was Chanute at 0535 UTC, located in the extreme southeastern corner of Kansas in Fig. 3.2b. That sounding had a lapse rate slightly steeper than moist adiabatic, with relative humidities between 90% and 100% throughout the troposphere. The values of the specific humidity at that station were used as the values at the bogus soundings, with a

slight adjustment upward for the more southerly bogus sites where the temperatures were slightly higher.

Fig. A.1a shows the effect of smoothing of pre-squall dry air into the convective line at 700 mb. Relative humidity at some points along the leading edge of convection falls to near 40%. Fig. A.1b shows the relative humidity at 700 mb with the addition of the bogus soundings. In general, little change occurs; however, the humidity along the leading edge of the convection typically has risen to over 70%, and drops no lower than 50%. These values are still too low realistically, since humidity within a region having such high radar reflectivities would be close to 100%. However, the gradient of the specific humidity is simply too sharp to be accurately represented in this type of objective analysis. The only way to obtain high humidity values throughout the convective line region would be to disregard all of the low values just ahead of the line. Although the humidity along the leading edge of the echo rises by only 20% or so, the difference in the Q_2 field was substantial, and the field was much more realistic after the inclusion of these bogus soundings. The errors in that field can be seen as intense moistening at the eastern edge of the 0600 UTC cross-section (Fig. 5.9b). Without the bogus soundings, the magnitude of the moistening was higher, and the band extended further west into the convective system.

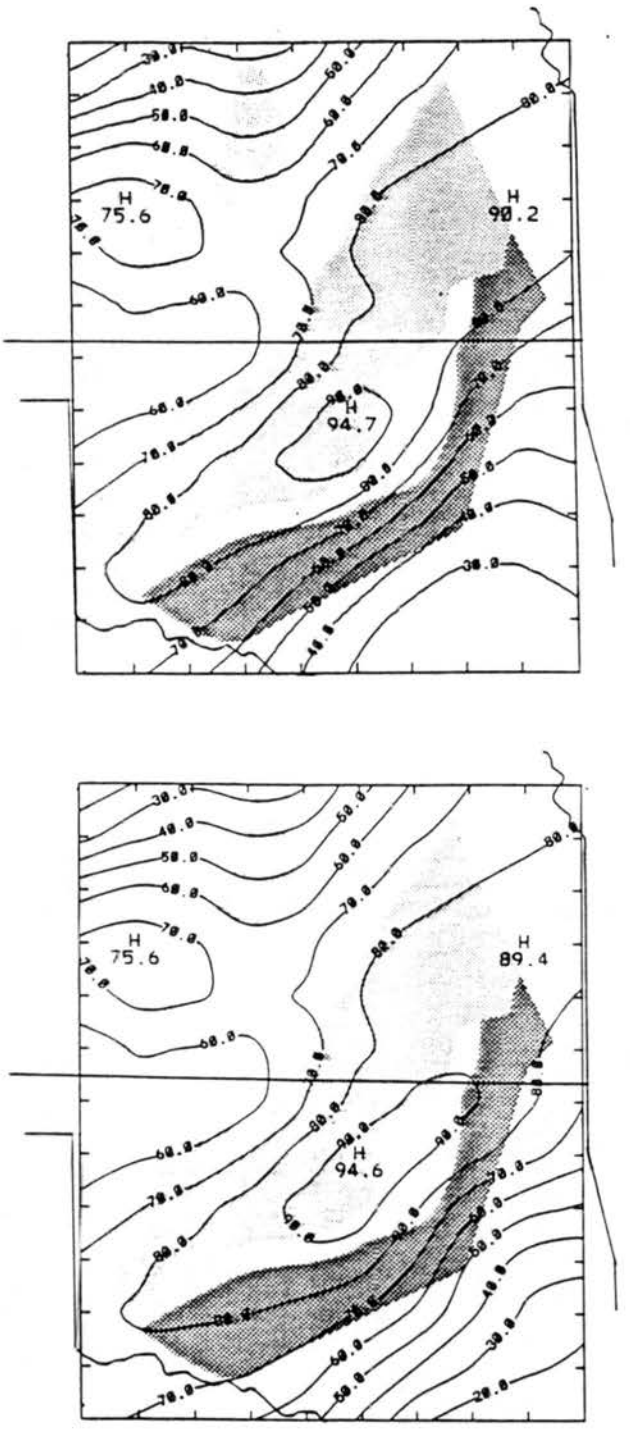

Figure A.1: Relative humidity at 0600 UTC at 700 mb for a.) analysis without bogus convective line soundings, b.) analysis with the addition of three nearly-saturated bogus soundings along leading edge of radar echo.